What's Cooler Than Being Cool?

Ice-Sheet Models Using a Fluidity-Based FOSLS Approach to Nonlinear-Stokes Flow.

by

Jeffery M. Allen

B.A., Carroll College, 2012

M.S., University of Boulder Colorado, 2014

A thesis submitted to the

Faculty of the Graduate School of the

University of Colorado in partial fulfillment

of the requirements for the degree of

Doctor of Philosophy

Department of Applied Mathematics

2017

This thesis entitled:
What's Cooler Than Being Cool? – Ice-Sheet Models Using a Fluidity-Based FOSLS Approach to Nonlinear-Stokes Flow.
written by Jeffery M. Allen
has been approved for the Department of Applied Mathematics

_____

Prof. Thomas Manteuffel

_____

Prof. Harihar Rajaram

Date _____

The final copy of this thesis has been examined by the signatories, and we find that both the content and the form meet acceptable presentation standards of scholarly work in the above mentioned discipline.

Allen, Jeffery M. (Ph.D., Applied Mathematics)

What's Cooler Than Being Cool? – Ice-Sheet Models Using a Fluidity-Based FOSLS Approach to Nonlinear-Stokes Flow.

Thesis co-directed by Prof. Thomas Manteuffel and Prof. Harihar Rajaram

This research involves a few First-Order System Least Squares (FOSLS) formulations of a nonlinear-Stokes flow model for ice sheets. In Glen's flow law, a commonly used constitutive equation for ice rheology, the viscosity becomes infinite as the velocity gradients approach zero. This typically occurs near the ice surface or where there is basal sliding. The computational difficulties associated with the infinite viscosity are often overcome by an arbitrary modification of Glen's law that bounds the maximum viscosity. The FOSLS formulations developed in this thesis are designed to overcome this difficulty.

The first FOSLS formulation is just the first-order representation of the standard nonlinear, full-Stokes and is known as the viscosity formulation and suffers from the problem above. To overcome the problem of infinite viscosity, two new formulation exploit the fact that the deviatoric stress, the product of viscosity and strain-rate, approaches zero as the viscosity goes to infinity. Using the deviatoric stress as the basis for a first-order system results in the the basic fluidity system. Augmenting the basic fluidity system with a curl-type equation results in the augmented fluidity system, which is more amenable to the iterative solver, Algebraic MultiGrid (AMG). A Nested Iteration (NI) Newton-FOSLS-AMG approach is used to solve the nonlinear-Stokes problems.

Several test problems from the ISMIP set of benchmarks is examined to test the effectiveness of the various formulations. These test show that the viscosity based method is more expensive and less accurate. The basic fluidity system shows optimal finite-element convergence. However, there is not yet an efficient iterative solver for this type of system and this is the topic of future research. Alternatively, AMG performs better on the augmented fluidity system when using specific scaling. Unfortunately, this scaling results in reduced finite-element convergence.

Dedication

I dedicate this thesis to my mom who helped keep me sane, my dad who helped push me forward, and my sister who inspired my love of math in the first place.

Acknowledgements

The two most obvious people I need to thank are Tom Manteuffel and Harihar Rajaram. Hari initially accepted me for this research, and Tom helped me every step of the way. Also, Steve McCormick deserves thanks for introducing me to the concepts of multigrid and Toby Jones for putting in a good word for me with Tom and Steve.

In terms of software, I have John Ruge to thank for offering his extensive knowledge of FOSPAC and AMG. I must give a huge thanks to the developers of FEniCS because, without their code, this research would be years behind. On that topic, Chris Liebs, and Steffen Münzenmaier get some gratitude for developing LEAP and helping me when the coding got tough.

Additionaly, there were people who helped me outside of research: Matt Edlin, Aly Fox, Dan Weidner, Hillary Fairbanks, Meredith Plumley, Taylor Epskamp, Kerry Garcia, Terri Wangler, Ben O'Neill, Ed Yasutake, Wayne Mitchell, Rebecca Hames, Delyan Kalchev, Pat Sprenger, James Folberth, Joe Benzaken, Anna Broido, Michelle Maiden and anyone I may have absentmindedly forgot. These people made the more unbearable parts of research manageable just by being good friends. I need to give a special shout out to Aly because, without her positive attitude and determination, I have no doubts that my laziness would have gotten the better of me.

Finally, I'd like to thank the members of the Walnut Table for meeting most Thursdays to discuss the outside world: Jerrad Hampton, Ben Dunham, and Aaron Pinsker.

Contents

Chapter

Tables

Table

Figures

Figure

Chapter 1

Introduction

Since the dawn of time, mankind has known one thing: ice is cold. Now, with the looming threat of global warming, that cold ice is beginning to melt. Sea level rise is one of the important projected consequences of climate warming [37]. During the past decade, the rate of sea level rise doubled, nearly half of which is due to increased mass loss from glaciers and ice sheets [43], while the remainder is due to thermal expansion of the ocean. Mass loss rates from the Greenland ice sheet more than doubled between 1996 and 2005, from 91 $\pm$ 31 to 224 $\pm$ 41 km^3/a [41], while the rate of mass loss from Antarctica and smaller glaciers combined have each increased by a factor of 1.5. It should be noted that "a" stands for annus which is equal to 31556925.445 seconds and similar to saying "per year". Predicting future contributions of the Greenland ice sheet to century-scale sea-level rise is one of the major challenges faced by the scientific community today. Greenland's mass loss appears to be equally split between surface mass balance (i.e. melt and runoff) and ice dynamics [45]. Ice dynamics refer to how the ice flows internally. Factors such as moulins, basal hydrology, stress heating, and the ice's general temperature can increase the ice flow rate leading to more discharge into the ocean. The need to improve predictions of the ice dynamics contribution from Greenland and Antarctica has prompted the development of advanced ice-sheet models. Historically, ice-sheet models have employed approximations to the momentum equation such as the Shallow-Ice approximation or the Blatter-Pattyn approximation [22]. More recently, however, several models that employ the full-Stokes equations have been developed [47, 30, 42].

One of the computational difficulties encountered in ice sheet modeling stems from the non-

Newtonian rheology of ice. In particular, Glen's flow law, the most commonly used constitutive equation for ice flow, involves an apparent viscosity that becomes infinite as the effective strain rate goes to zero, which occurs in regions where there is little deformation. This difficulty is sometimes circumvented by adding a small constant to the effective strain rate in the constitutive law, thus avoiding the "blow-up" of the viscosity [38]. Another method is to approximate the viscosity in these regions with a large value [29]. Both of these methods affect the accuracy of the numerical solution.

The reality is that this infinite viscosity results from a removable singularity. In Glen's law, the viscosity behaves as the effective strain rate taken to the $-2/3$ power when $n = 3$ (See Section 2.3 (2.3.11)). The deviatoric stress involves the product of the viscosity times the strain rate. In regions where the velocity becomes constant, the strain rate goes to zero, and the deviatoric stress behaves like the the effective strain rate taken to the $1/3$ power. That is, the deviatoric stress goes to zero. In such regions, numerical approximation explicitly using the viscosity requires the product of a nearly infinite viscosity multiplied by a nearly zero strain rate. This is the root cause of numerical difficulties.

In this thesis, three First-Order System Least-Squares (FOSLS) formulations are developed for the nonlinear, full-Stokes model. The first uses a velocity-gradient/velocity/pressure system of unknowns and is denoted the **viscosity form**. It involves the viscosity explicitly and suffers some of the same difficulties as mentioned above. The next two formulations involve the fluidity, which is the inverse of viscosity. The system of unknowns for the second formulation are deviatoric-stress/pressure/velocity and is not fully H^1 elliptic, but rather closer to an $H(\text{div})$-type system. It will be referred to as the **basic fluidity form**. The final formulation takes the basic fluidity form and adds a few consistent equation to get closer to an H^1 elliptic system. It will be referred to as the **augmented fluidity form**. The last two formulations are collectively known as the **fluidity forms** and there is no need to modify the constitutive law for these formulations since viscosity does not appear in either. Additionally, FOSLS formulations give rise to linear systems that are symmetric positive definite (SPD).

The nonlinear system is addressed numerically using a Nested Iteration (NI) approach [11] with Newton iterations on each level. Nested Iteration involves solving the system on successively finer grids and using the coarser grid solution as the initial guess. The number of Newton iterations required decreases with grid refinement since the interpolated coarse grid solution is an increasingly better initial guess. This results in most of the work done on the coarsest grids, where computation is inexpensive [17]. For the augmented fluidity system, if continuity and coercivity can be established, then the resulting linear systems are amenable using algebraic multigrid (AMG), yielding a very efficient and accurate solution strategy. Taking advantage of the sharp, local error estimate provided by FOSLS, an adaptive refinement method developed in [2, 7, 35], known as ACE, can be used to maximize Accuracy per Computational cost (Efficiency). The ACE algorithm works by estimating the increase of cost when an element is refined and compares that with another estimate of how the error on that element will be reduced. These estimates come from the AMG performance and FOSLS functional on the current level.

The consistent equations discussed above are similar to the curl constraint introduced in [13, 14], and adding them results in a FOSLS functional for which linearization in a neighborhood of the exact solution is, again loosely speaking, H^1-coercive. This these equations are added in the viscosity form and the augmented fluidity form. (The linearizations are Agmon-Douglis-Nirenberg (ADN) H^1-elliptic [4, 9].) Continuity is easily established, see Section 6.2. Coercivity for the boundary conditions examined here remains an open question, see Section 6.3 for details.) Both of these forms yield linearized systems that are amenable to AMG with proper scaling. The viscosity form yields systems for which AMG performance deteriorates somewhat in the presence of near-infinite viscosity, whereas the fluidity form yields systems that are more easily solved even as fluidity approaches zero for simple domains.

As the domains become more complex, the scalings that allows for AMG to perform better cause the finite element convergence to diminish. The basic fluidity formulation presents optimal finite element converge in several cases. However, a fast iterative solver for this type of system has yet to be implemented. The full-Stokes equations can be constructed so that linearization of

the FOSLS functional in a neighborhood of the exact solution is, loosely speaking, $H(Div) \times H^1$ coercive [34]. Linear system solvers specifically designed for $H(div)$-type systems may provide scalable solvers for these systems [26, 27, 44]. This is a topic for future investigation.

A simple, two-dimensional test problem that exhibits infinite viscosity along the entire surface is used to compare convergence of the finite element approximation and solver performance for the viscosity-based and fluidity-based formulations. Both the viscosity and H^1-type fluidity formulations yield accurate solutions and are amenable to the NI-Newton-FOSLS-AMG strategy. However, the augmented fluidity form is both more accurate and yields linearized systems that are more easily solved by AMG.

Next, several experiments from the Ice Sheet Model Intercomparison Project (ISMIP) are examined using the new fluidity formulations [39]. It is shown that the augmented fluidity formulation essentially reproduces the results in [30], except in regions where the viscosity becomes nearly infinite (fluidity approaches zero), where the augmented fluidity form is more faithful to Glen's law. The Galerkin, mixed-method form presented in [30] is used as a comparison for the ISMIP test problems. In this formulation, the viscosity is explicitly expressed in the bilinear forms. While the exact relationship is not explicitly stated in [30], in general, formulations explicitly using viscosity modify the constitutive equations. However, in this thesis, no modification is used.

The Galerkin formulation yields a saddle-point problem. A standard approach to linear systems of this form is to use a block Preconditioned Conjugate Gradient (PCG) iteration involving an AMG solver for the velocity block [20]. This approach, used in [30], is complicated by near-infinite viscosity. While [30] does not present solver performance, tests performed on similar systems show that near-infinite viscosity causes AMG convergence factors to deteriorate. Even without this extra difficulty, convergence of PCG requires many iterations where each iteration requires an application of AMG. On the other hand, the FOSLS formulations achieve an accurate solution with only a few application of AMG for each Newton step. In this thesis, the Galerkin formulation is simply solved with a direct LU solver to avoid worrying about CG convergence.

The remainder of the thesis is organized as follows. Chapters 2 and 3 are background in-

formation that discuss various ice-sheet models and some of the numerical methods involved in this research. An interesting side project is discussed in Chapter 4 involving determining the basal topography of a glacier using surface velocities. Chapter 5 describes the several full-Stokes formulations used in this thesis. Specifically Section 5.2 develops the FOSLS viscosity formulation while Section 5.4 develops the two FOSLS fluidity formulations. Chapter 6 examines linearization of both the fluidity and viscosity forms, establishes H^1-continuity, and discusses coercivity of the FOSLS formulations. Chapters 7 through 11 provides numerical results for various test problems. Chapter 7 presents a simple problem for which the exact solution is known, in order to establish finite-element convergence and AMG performance of the viscosity and augmented fluidity formulations. This test problem shows that the viscosity formulation is inferior and is no long used in the following test problems. Chapters 8-9 describe the performance of both fluidity models on benchmarks B and D from the Ice Sheet Model Intercomparison Project (ISMIP). Together, these two test problems provide enough data to conclude that the augmented fluidity system, while providing better AMG performance, is not reliable. For the remaining two benchmarks, E and an adapted version of F in Chapters 10-11, only the basic fluidity system is used. All of the benchmark solutions fluidity formulations are compared with the Taylor-Hood fomrulation presented in Section 5.1. The fluidity model shows good agreement with the database of solutions for these experiments as well as recovering larger viscosities. Finally, the results of this thesis are discussed in Chapter 12.

Chapter 2

Ice Sheet Models

Ice sheets are usually modeled as slowly-moving, viscous, incompressible fluids. As such, a full-Stokes formulation is an obvious choice. However, since solving the full-Stokes equations can be costly, several approximations to Stokes equations have been developed. This section will by developing the full-Stokes system and then develop two models that approximate this system. The first approximation is a "zeroth order" model known as the shallow ice approximation. Logically, the second approximation will be the first-order Blatter-Pattyn model.

2.1 Derivation of the Balance Equations

One of the goals of this section is to derive the full-Stokes equations, which will be used later to model glaciers and ice sheets, but first, a general balance equation will be derived. To start, let $\mathcal{Q}(m_v, t)$ be the physical quantity of interest inside the material volume, m_v. The change of this quantity with respect to time, t, is due to only two factors, which are outward flux across the boundary and production within the volume. These factors, as well as the original physical quantity, can be represented as integrals of corresponding densities such that:

$$\mathcal{Q}(m_v, t) = \int_{m_v} q(\underline{x}, t)\, dv, \qquad \text{(Quanity of interest)}$$

$$\mathcal{W}(\partial m_v, t) = \oint_{\partial m_v} \underline{w}(\underline{x}, t) \cdot \underline{n}\, da, \qquad \text{(Flux across the boundary)}$$

$$\mathcal{P}(m_v, t) = \int_{m_v} p(\underline{x}, t)\, dv, \qquad \text{(Production within the volume)}$$

Then,

$$\frac{\partial}{\partial t}\mathcal{Q}(m_v,t) = -\mathcal{W}(\partial m_v,t) + \mathcal{P}(m_v,t),$$

or,

$$\frac{d}{dt}\int_{m_v} q(\underline{x},t)\,dv = -\oint_{\partial m_v} \underline{w}(\underline{x},t)\cdot\underline{n}\,da + \int_{m_v} p(\underline{x},t)\,dv.$$

Now, assuming each of the densities is sufficiently smooth, the time partial derivative can be brought inside the integral using the Reynolds' transport theorem [22], yielding:

$$\int_{m_v}\frac{\partial q}{\partial t}\,dv + \oint_{\partial m_v} q\underline{u}\cdot\underline{n}\,da = -\oint_{\partial m_v}\underline{w}\cdot\underline{n}\,da + \int_{m_v} p\,dv,$$

where $\underline{u} = [u_1, u_2, u_3]^T$ is the fluid velocity vector. Now, use the Divergence to convert the above surface integrals into volume integrals resulting in:

$$\int_{m_v}\frac{\partial q}{\partial t}\,dv + \int_{m_v}\nabla\cdot(q\underline{u})\,dv = -\int_{m_v}\nabla\cdot\underline{w}\,dv + \int_{m_v} p\,dv.$$

Finally, move everything to the same side and combine the integrals to get:

$$\int_{m_v}\left(\frac{\partial q}{\partial t} + \nabla\cdot(q\underline{u}) + \nabla\cdot\underline{w} - p\right)dv = 0.$$

Since, this relation must hold true for any arbitrary material volume, m_v, the integrand must be equal to zero as well, resulting in:

$$\frac{\partial q}{\partial t} = -\nabla\cdot(q\underline{u} + \underline{w}) + p \tag{2.1.1}$$

Now, it is time to apply this general balance equation to conservation of momentum. If ρ is the mass density, the total momentum of a material volume is $\underline{P} = \int_{m_v}\rho\underline{u}\,dv$. Newton's Second Law states that the change $\frac{d\underline{P}}{dt}$ must equal the sum of all forces acting on the material volume. These forces are the external forces, $\underline{f}$, such as gravity and the internal stresses acting on the boundary of the material volume, $\underline{\underline{\sigma}}$. Applying Newton's Second Law to the material volume yields:

$$\frac{d}{dt}\int_{m_v}\rho(\underline{x},t)\underline{u}(\underline{x},t)\,dv = \oint_{\partial m_v}\underline{\underline{\sigma}}(\underline{x},t)\cdot\underline{n}\,da + \int_{m_v}\underline{f}(\underline{x},t)\,dv.$$

This is similar to the general balance equation (2.1.1) with $q = \rho\underline{u}$, $\underline{w} = -\underline{\underline{\sigma}}$, and $p = \underline{f}$. Therefore, Newton's Second Law can be written:

$$\frac{\partial(\rho\underline{u})}{\partial t} + \nabla \cdot (\rho\underline{u} \cdot \underline{u}) = \nabla \cdot \underline{\underline{\sigma}} + \underline{f}. \tag{2.1.2}$$

This thesis only deals with incompressible fluids where ρ is consider constant. Applying this assumption and taking the product rule of the second term yields:

$$\rho\frac{\partial(\underline{u})}{\partial t} + \rho(u \cdot \nabla) \cdot \underline{u} = \nabla \cdot \underline{\underline{\sigma}} + \underline{f}. \tag{2.1.3}$$

Conservation of mass follows in a similar fashion. The total mass in a material volume is represented by the integral $\int_{m_v} \rho \, dv$. Since mass cannot be created or destroyed within a material volume:

$$\frac{d}{dt}\int_{m_v} \rho \, dv = 0.$$

Equating this to the general balance equation (2.1.1) with $q = \rho$, $\underline{w} = \underline{0}$, and $p = 0$, the conservation of mass is just:

$$\frac{\partial\rho}{\partial t} + \nabla \cdot (\rho\underline{u}) = 0. \tag{2.1.4}$$

Using the assumption of a incompressible fluid, the mass balance or continuity equation reduces down to:

$$\nabla \cdot \underline{u} = 0. \tag{2.1.5}$$

Equations (2.1.3)-(2.1.5) describe the motion of a fluid, and, with a valid definition of $\underline{\underline{\sigma}}$, these equations represent the incompressible Navier-Stokes equations. Additionally, there is an energy balance equation, but this is neglected for now. To get to the equations of Stokes flow, the acceleration terms are neglected.

2.2 Glen's Flow Law

Glen's flow law is central to this research and is essential to building the full-Stokes equations. A quick derivation of it will be described in this section. To start off, a general strain-stress

relationship for nonlinear viscous flow is

$$\dot{\underline{\underline{\varepsilon}}} = \frac{1}{2\mu(T,p,s_e)}\underline{\underline{s}}, \tag{2.2.1}$$

where $\dot{\underline{\underline{\varepsilon}}} = \frac{1}{2}\left(\nabla\underline{u} + (\nabla\underline{u})^T\right)$ is the strain rate, $\underline{\underline{s}}$ the traceless stress deviator, μ is shear viscosity which depends on temperature, T, pressure, p, and the effective stress, s_e. For more information on the derivation of this general relationship see [22]. The effective stress comes from the square root of the second invariant of the stress deviator:

$$s_e = \sqrt{\frac{1}{2}\mathrm{tr}(\underline{\underline{s}}^2)} = \frac{1}{\sqrt{2}}||\underline{\underline{s}}||_F, \tag{2.2.2}$$

where $||\cdot||_F$ is the Frobenius norm. The inverse of viscosity, also known as fluidity, can be represented as

$$\frac{1}{\mu(T,p,s_e)} = 2A(T,p)f(s_e),$$

where $A(T,p)$ is the flow rate factor, and $f(s_e)$ is known as the creep function. For the purposes of this dissertation, $A(T,p)$ will be consider the constant with respect to temperature and pressure. The creep function is usually express as a power law $f(s_e) = s_e^{n-1}$. Combining these with Equation (2.2.1) yields one version of what is commonly known as Glen's flow law,

$$\dot{\underline{\underline{\varepsilon}}} = As_e^{n-1}\underline{\underline{s}}, \tag{2.2.3}$$

which has the corresponding viscosity,

$$\mu(s_e) = \frac{1}{2As_e^{n-1}}. \tag{2.2.4}$$

Another useful version of Glen's flow law is with stress as a function of strain. To find this relationship first define the effective strain rate,

$$\dot{\varepsilon}_e = \sqrt{\frac{1}{2}\mathrm{tr}(\dot{\underline{\underline{\varepsilon}}}^2)} = \frac{1}{\sqrt{2}}||\dot{\underline{\underline{\varepsilon}}}||_F, \tag{2.2.5}$$

which is similar to how effective stress (2.2.2) was defined. Plugging in Equation (2.2.3) into (2.2.5) yields

$$\dot{\varepsilon}_e = \sqrt{\frac{1}{2}\mathrm{tr}((As_e^{n-1}\underline{\underline{s}})^2)} = As_e^{n-1}\sqrt{\frac{1}{2}\mathrm{tr}(\underline{\underline{s}}^2)} = As_e^{n-1}s_e = As_e^n \quad \Leftrightarrow \quad s_e = A^{-1/n}\dot{\varepsilon}_e^{1/n}.$$

Solving Equation (2.2.3) for the stress devator and plugging in the newly found expression for effective stress in terms of effective strain rate will result in another version of Glen's flow law.

$$\begin{aligned}\underline{\underline{s}} &= A^{-1} s_e^{-(n-1)} \underline{\underline{\dot{\varepsilon}}} \\ &= A^{-1} A^{(n-1)/n} \dot{\varepsilon}_e^{-(n-1)/n} \underline{\underline{\dot{\varepsilon}}} \\ \underline{\underline{s}} &= A^{-1/n} \dot{\varepsilon}_e^{(1-n)/n} \underline{\underline{\dot{\varepsilon}}}. \end{aligned} \tag{2.2.6}$$

In this version, the viscosity is

$$\mu(\dot{\varepsilon}_e) = \frac{1}{2} A^{-1/n} \dot{\varepsilon}_e^{(1-n)/n}. \tag{2.2.7}$$

For ice sheets, it is generally accepted that $n = 3$ [22].

2.3 Full Stokes

In this section, the nonlinear Stokes model for ice-sheet flow is developed; for more details see [22]. The model for glacier/ice-sheet flow is a modification of the Stokes equations. The first assumption made is that ice is an incompressible fluid with constant density, which leads to the continuity equation from 2.1.5, reproduced here:

$$\nabla \cdot \underline{u} = 0. \tag{2.3.1}$$

For quasi-steady-state Stokes flow (negligible acceleration), the momentum equation from 2.1.3 becomes:

$$\nabla \cdot \underline{\underline{\sigma}} - \underline{f} = 0. \tag{2.3.2}$$

In physical problems the forcing function, $\underline{f}$, is the gravitational body force $\rho \underline{g}$, where ρ is density, $\underline{g}$ is gravitational acceleration, and $\underline{\underline{\sigma}}$ is the stress tensor. With an appropriate constitutive relationship between the pressure, stress tensor, and the strain rate (related to $\underline{u}$), equations (2.3.1) and (2.3.2) are suitable for modeling glaciers and ice sheets.

The stress tensor can be broken up into two parts: the deviatoric stress ($\underline{\underline{s}}$) and mean normal stress (pressure, p),

$$\underline{\underline{\sigma}} = \underline{\underline{s}} - p\underline{\underline{I}}. \tag{2.3.3}$$

The deviatoric stress can be expressed as a function of viscosity, μ, and strain-rate tensor, $\underline{\underline{\dot{\varepsilon}}}$:

$$\underline{\underline{s}} = 2\mu\underline{\underline{\dot{\varepsilon}}}, \tag{2.3.4}$$

$$\underline{\underline{\dot{\varepsilon}}} = \frac{1}{2}\left(\nabla\underline{u} + (\nabla\underline{u})^T\right), \tag{2.3.5}$$

with the notation

$$\nabla\underline{u} = \left[\nabla u_1, \nabla u_2, \nabla u_3\right]. \tag{2.3.6}$$

Glen's flow law for the viscosity from Equation (2.2.7) is:

$$\mu = \frac{1}{2}A^{-\frac{1}{n}}\dot{\varepsilon}_e^{\frac{1}{n}-1}, \tag{2.3.7}$$

with,

$$\dot{\varepsilon}_e = \sqrt{\frac{1}{2}\sum_{i,j}|\dot{\varepsilon}_{ij}|^2} = \frac{1}{\sqrt{2}}\left|\left|\underline{\underline{\dot{\varepsilon}}}\right|\right|_F, \tag{2.3.8}$$

where n is the power-law exponent, $\dot{\varepsilon}_e$ is the effective strain rate as defined in [15, 40, 30], $||\cdot||_F$ is the Frobenius norm, and A is the flow law parameter.

Combining all the above PDEs and constitutive relationships, the system of equations for modeling ice flow can be stated as:

$$\nabla\cdot\underline{u} = 0, \qquad \text{(Continuity)} \tag{2.3.9}$$

$$\nabla\cdot\left(\hat{\mu}\left(\nabla\underline{u} + (\nabla\underline{u})^T\right)\right) - \nabla\hat{p} = \underline{f}, \qquad \text{(Momentum)} \tag{2.3.10}$$

$$\hat{\mu} = ||\underline{\underline{\dot{\varepsilon}}}||_F^{-\frac{2}{3}}, \qquad \text{(Viscosity)} \tag{2.3.11}$$

with $\hat{p} = \frac{p}{c_A}$, $\hat{\rho} = \frac{\rho}{c_A}$, $c_A = \frac{1}{2}\left(\frac{A}{2}\right)^{-\frac{1}{3}}$. The difficulty with this formulation occurs in the viscosity term. In regions of a glacier/ice-sheet where ice deformation rates are small, the strain-rate tensor, $\underline{\underline{\dot{\varepsilon}}}$, approaches zero. This occurs when the ice is moving as a solid block, as is often encountered near the surface and in regions with significant basal sliding. When the strain-rate tensor goes to zero, the viscosity defined by (2.3.11) becomes infinite.

One frequently employed modification to resolve this problem is to add a small constant to the viscosity to prevent unconstrained growth. Viscosity is redefined as:

$$\mu_c = \frac{1}{2}A^{-\frac{1}{3}}\left(\frac{1}{\sqrt{2}}||\underline{\underline{\dot{\varepsilon}}}||_F^2 + c\right)^{-\frac{1}{3}}, \tag{2.3.12}$$

where c is a small constant [38].

However, the unconstrained growth of the viscosity may be viewed as a removable singularity. The viscosity cannot be infinite unless the strain-rate tensor is zero. Assume the strain rate scales as α, then the viscosity behaves like $\alpha^{-\frac{2}{3}}$. The momentum equation involves the product of the strain-rate tensor and the viscosity (i.e. the deviatoric stress, $\underline{\underline{s}}$), which behaves like $\alpha^{\frac{1}{3}}$, and thus, goes to zero as the strain rate becomes zero. This will be the motivation for combining the viscosity and strain-rate tensor into one new variable and is the basis for this research.

2.4 Shallow Ice

The Shallow Ice Approximation (SIA) is one of the simplest way to model ice sheets. It relies on the idea that ice sheets have a large aspect ratio (i.e. the thickness is negligible compared with the length and width). In other words, if L represents the horizontal length scales, x and y, and H represents the vertical length scale, z, then $H/L \ll 1$. This the basis of the approximation in the SIA model, which involves ignoring several terms in the stress tensor. See [21] for more details.

From Equations (2.3.2) and (2.3.3), the momentum equation can be written as $\nabla \cdot \underline{\underline{s}} - \nabla p = \underline{f}$, which expanded into component form yields:

$$\frac{\partial s_{11}}{\partial x} + \frac{\partial s_{12}}{\partial y} + \frac{\partial s_{13}}{\partial z} - \frac{\partial p}{\partial x} = 0, \tag{2.4.1}$$

$$\frac{\partial s_{12}}{\partial y} + \frac{\partial s_{22}}{\partial x} + \frac{\partial s_{23}}{\partial z} - \frac{\partial p}{\partial y} = 0, \tag{2.4.2}$$

$$\frac{\partial s_{13}}{\partial z} + \frac{\partial s_{23}}{\partial x} + \frac{\partial s_{33}}{\partial y} - \frac{\partial p}{\partial z} = \rho g. \tag{2.4.3}$$

The terms in red are the ones that are neglected by the approximations in the SIA model. Removing these terms yields:

$$\frac{\partial s_{13}}{\partial z} - \frac{\partial p}{\partial x} = 0, \tag{2.4.4}$$

$$\frac{\partial s_{23}}{\partial z} - \frac{\partial p}{\partial y} = 0, \tag{2.4.5}$$

$$-\frac{\partial p}{\partial z} = \rho g. \tag{2.4.6}$$

To solve this system start with (2.4.6). Vertically integrating this equation results in the equation for hydrostatic pressure,

$$p = \rho g(z_s - z). \tag{2.4.7}$$

where z_s is the function that describes the surface of the ice sheet. Hydrostatic pressure is essentially generated by the weight of the ice above a certain point in the ice sheet.

Now with a solution for p, Equations (2.4.4) and (2.4.5) can be simplified as follows:

$$\frac{\partial s_{13}}{\partial z} - \frac{\partial p}{\partial x} = 0 \Rightarrow \frac{\partial s_{13}}{\partial z} = \frac{\partial}{\partial x}(\rho g(z_s - z)) = \rho g \frac{\partial z_s}{\partial x}. \tag{2.4.8}$$

$$\frac{\partial s_{23}}{\partial z} - \frac{\partial p}{\partial y} = 0 \Rightarrow \frac{\partial s_{23}}{\partial z} = \frac{\partial}{\partial y}(\rho g(z_s - z)) = \rho g \frac{\partial z_s}{\partial y}. \tag{2.4.9}$$

Before integrating (2.4.8) and (2.4.9), boundary conditions must be discussed. On the surface of the ice sheet, a zero stress condition is enforced. This conditions amounts to $\underline{\underline{\sigma}} \cdot n = 0$, in other words the normal component of the stress tensor is zero. Another assumption of the SIA model is that the the surface normal is approximated by $[0, 0, 1]^T$. With that assumption, $\underline{\underline{\sigma}} \cdot n = 0$ reduces to $s_{13} = 0$ and $s_{23} = 0$ on the surface. Now, integrate equations (2.4.8) and (2.4.9) to get:

$$s_{13} = -\rho g(z_s - z)\frac{\partial z_s}{\partial x}, \tag{2.4.10}$$

$$s_{23} = -\rho g(z_s - z)\frac{\partial z_s}{\partial y}. \tag{2.4.11}$$

To solve these equations for velocity, recall Equation (2.3.4) as well as Equations (2.2.2) and (2.2.4) from Glen's Law, which are reproduced below:

$$\underline{\underline{s}} = 2\mu\underline{\underline{\dot{\varepsilon}}}, \qquad \mu = \frac{1}{2As_e^{n-1}}, \qquad s_e = \frac{1}{\sqrt{2}}||\underline{\underline{s}}||_F.$$

Under the assumption of the SIA model, $||\underline{\underline{s}}||_F = \sqrt{2{s_{13}}^2 + 2{s_{23}}^2}$. Therefore, with Equations (2.4.10) and (2.4.11),

$$s_e = \sqrt{{s_{13}}^2 + {s_{23}}^2} = \rho g(z_s - z)\left(\frac{\partial z_s}{\partial x}^2 + \frac{\partial z_s}{\partial y}^2\right)^{1/2} = \rho g(z_s - z)||\nabla z_s||.$$

Solving (2.3.4) for strain rate and using Equations (2.2.2) and (2.2.4) yields:

$$\dot{\varepsilon} = As_e^{n-1}\underline{\underline{s}} = A\left(\rho g(z_s - z)||\nabla z_s||\right)^{n-1}\underline{\underline{s}}, \tag{2.4.12}$$

Next, extract the components that correspond to s_{13} and s_{23},

$$\begin{aligned}\frac{1}{2}\left(\frac{\partial u_1}{\partial z}+\frac{\partial u_3}{\partial x}\right) &= A\left(\rho g(z_s-z)||\nabla z_s||\right)^{n-1} s_{13} = A(\rho g(z_s-z))^n||\nabla z_s||^{n-1}\frac{\partial z_s}{\partial x}\\ \frac{1}{2}\left(\frac{\partial u_2}{\partial z}+\frac{\partial u_3}{\partial y}\right) &= A\left(\rho g(z_s-z)||\nabla z_s||\right)^{n-1} s_{23} = A(\rho g(z_s-z))^n||\nabla z_s||^{n-1}\frac{\partial z_s}{\partial y}\end{aligned} \tag{2.4.13}$$

Again, under the assumption of the SIA model, the horizontal derivative of the vertical velocity is negligible so these equation reduce to

$$\begin{aligned}\frac{\partial u_1}{\partial z} &= 2A(\rho g(z_s-z))^n||\nabla z_s||^{n-1}\frac{\partial z_s}{\partial x}\\ \frac{\partial u_2}{\partial z} &= 2A(\rho g(z_s-z))^n||\nabla z_s||^{n-1}\frac{\partial z_s}{\partial y}\end{aligned}$$

or equivalently

$$\nabla \underline{u} = 2A(\rho g(z_s-z))^n||\nabla z_s||^{n-1}\nabla z_s \tag{2.4.14}$$

Now integrate from the bed to some arbitrary z value to get:

$$\begin{aligned}\underline{u} &= 2A(\rho g)^n||\nabla z_s||^{n-1}\nabla z_s\int_{z_b}^{z}(z_s-\widetilde{z})^n\,d\widetilde{z},\\ &= \frac{2A(\rho g)^n}{n+1}||\nabla z_s||^{n-1}\nabla z_s\left(H^{n+1}-(z_s-z)^{n+1}\right),\end{aligned} \tag{2.4.15}$$

where $H(x,y) = z_s(x,y) - z_b(x,y)$ is the ice thickness. Equations (2.4.7) and (2.4.15) represent the steady-state velocity and pressure profile of an isothermal ice sheet under the shallow ice approximation assumptions. Notice that when $n = 3$ is used, the velocities are proportional to the depth to the fourth power meaning the velocities are approximated by quartic function under the SIA model.

2.5 Blatter-Pattyn

Another commonly used approximation is the Blatter-Pattyn model, which is a first-order model. Again, the starting point for this model is the momentum equations (2.4.1)-(2.4.3) repro-

duced here.

$$\frac{\partial s_{11}}{\partial x} + \frac{\partial s_{12}}{\partial y} + \frac{\partial s_{13}}{\partial z} - \frac{\partial p}{\partial x} = 0, \tag{2.5.1}$$

$$\frac{\partial s_{12}}{\partial x} + \frac{\partial s_{22}}{\partial y} + \frac{\partial s_{23}}{\partial z} - \frac{\partial p}{\partial y} = 0, \tag{2.5.2}$$

$$\frac{\partial s_{33}}{\partial z} + \frac{\partial s_{13}}{\partial x} + \frac{\partial s_{23}}{\partial y} - \frac{\partial p}{\partial z} = \rho g. \tag{2.5.3}$$

Just like with the SIA model, the key simplification for this model is that the length scale is significantly larger than the height. However, fewer stress terms are neglected in the Blatter-Pattyn model leading to the assumption that only,

$$\frac{\partial s_{13}}{\partial x} = \frac{\partial s_{23}}{\partial y} = 0,$$

which are the red term in the system above. This assumption leads to the vertical component of the momentum balance to become:

$$\frac{\partial s_{33}}{\partial z} - \frac{\partial p}{\partial z} = \rho g. \tag{2.5.4}$$

Just like with the SIA model, the surface normal is approximated by $n = [0, 0, 1]^T$, which leads to the last surface boundary condition from $\underline{\underline{\sigma}} \cdot n$ to be $s_{33} - p = 0$. Vertically Integrating (2.5.4) yields:

$$p = \rho g(z_s - z) + s_{33}. \tag{2.5.5}$$

Plugging Equation (2.5.5) into (2.5.1)-(2.5.2) reduces the system down to

$$\frac{\partial s_{11}}{\partial x} - \frac{\partial s_{33}}{\partial x} + \frac{\partial s_{12}}{\partial y} + \frac{\partial s_{13}}{\partial z} = \rho g \frac{\partial z_s}{\partial x}, \tag{2.5.6}$$

$$\frac{\partial s_{22}}{\partial y} - \frac{\partial s_{33}}{\partial y} + \frac{\partial s_{12}}{\partial x} + \frac{\partial s_{23}}{\partial z} = \rho g \frac{\partial z_s}{\partial y}. \tag{2.5.7}$$

This system can be further reduced by using the continuity equation, (2.3.1), to replace s_{33}. Notice that

$$s_{11} + s_{22} + s_{33} = 2\mu \left(\frac{\partial u_1}{\partial x} + \frac{\partial u_2}{\partial y} + \frac{\partial u_3}{\partial z} \right) = 0. \tag{2.5.8}$$

Using this equation to simplify (2.5.6)-(2.5.7) yields

$$2\frac{\partial s_{11}}{\partial x} + \frac{\partial s_{22}}{\partial x} + \frac{\partial s_{12}}{\partial y} + \frac{\partial s_{13}}{\partial z} = \rho g \frac{\partial z_s}{\partial x}, \tag{2.5.9}$$

$$\frac{\partial s_{11}}{\partial y} + 2\frac{\partial s_{22}}{\partial y} + \frac{\partial s_{12}}{\partial x} + \frac{\partial s_{23}}{\partial z} = \rho g \frac{\partial z_s}{\partial y}. \tag{2.5.10}$$

The final step is to use Equations (2.3.4) and (2.3.5) to convert the system into one that is in terms of velocity. As an example, the steps of this simplification will be demonstrated on the x-component of the momentum balance:

$$2\frac{\partial}{\partial x}(s_{11}) + \frac{\partial}{\partial x}(s_{22}) + \frac{\partial}{\partial y}(s_{12}) + \frac{\partial}{\partial z}(s_{13}) = \rho g \frac{\partial z_s}{\partial x},$$

$$2\frac{\partial}{\partial x}\left(2\mu\frac{\partial u_1}{\partial x}\right) + \frac{\partial}{\partial x}\left(2\mu\frac{\partial u_1}{\partial y}\right) + \frac{\partial}{\partial y}\left(\mu\left(\frac{\partial u_1}{\partial y} + \frac{\partial u_2}{\partial x}\right)\right) + \frac{\partial}{\partial z}\left(\mu\left(\frac{\partial u_1}{\partial z} + \frac{\partial u_3}{\partial x}\right)\right) = \rho g \frac{\partial z_s}{\partial x}.$$

By the initial assumption, $\frac{\partial u_3}{\partial x}$ is negligible and can be ignored:

$$4\frac{\partial}{\partial x}\left(\mu\frac{\partial u_1}{\partial x}\right) + 2\frac{\partial}{\partial x}\left(\mu\frac{\partial u_1}{\partial y}\right) + \frac{\partial}{\partial y}\left(\mu\left(\frac{\partial u_1}{\partial y} + \frac{\partial u_2}{\partial x}\right)\right) + \frac{\partial}{\partial z}\left(\mu\frac{\partial u_1}{\partial z}\right) = \rho g \frac{\partial z_s}{\partial x}.$$

Apply the same simplification to the y-component to get the Blatter-Pattyn model:

$$4\frac{\partial}{\partial x}\left(\mu\frac{\partial u_1}{\partial x}\right) + \frac{\partial}{\partial y}\left(\mu\frac{\partial u_1}{\partial y}\right) + \frac{\partial}{\partial z}\left(\mu\frac{\partial u_1}{\partial z}\right) = \rho g \frac{\partial z_s}{\partial x} - \frac{\partial}{\partial y}\left(\mu\frac{\partial u_2}{\partial x}\right) - 2\frac{\partial}{\partial x}\left(\mu\frac{\partial u_2}{\partial y}\right), \tag{2.5.11}$$

$$\frac{\partial}{\partial x}\left(\mu\frac{\partial u_2}{\partial x}\right) + 4\frac{\partial}{\partial y}\left(\mu\frac{\partial u_2}{\partial y}\right) + \frac{\partial}{\partial z}\left(\mu\frac{\partial u_2}{\partial z}\right) = \rho g \frac{\partial z_s}{\partial y} - 2\frac{\partial}{\partial y}\left(\mu\frac{\partial u_1}{\partial x}\right) - \frac{\partial}{\partial x}\left(\mu\frac{\partial u_1}{\partial y}\right). \tag{2.5.12}$$

Chapter 3

Numerical Methods

The following is a short description of the various numerical methods used in this dissertation.

3.1 FOSLS

The main method of solving systems in this dissertation will involve a First-Order System Least-Squares (FOSLS) approach. Essentially, this involves using a first-order system to generate a functional for which the minimum is the desired solution. Then, the functional is restricted to a finite element space and minimized using least squares, which yields a discrete nonlinear system of equations. Originally, this method was applied to general convection-diffusion problems [12]. Since then, it has been applied to various other elliptic type problem such as Maxwell's equations, neutron transport, two-fluid plasma, and, as seen in this dissertation, various forms of Navier-Stokes equations [3, 13, 32, 33, 28].

One of the current ways to solve the full-Stokes system for ice sheets is to set up a Galerkin saddle point problem and solve on a mixed finite-element space with different elements in pressure and velocity [30]. This mixed finite-element space needs to satisfy the discrete infsup condition known as the Ladyženskaja-Babuška-Brezzi (LBB) condition. Converting the full-Stokes system into a FOSLS formulation bypasses the need to satisfy this condition, allowing the choice of standard finite element spaces. If linearization of the functional is H^1 elliptic in a neighborhood of the exact solution, the resulting linear systems of equations are often amenable to fast iterative solvers such as

algebraic multigrid (AMG). By the nature of the weak form coming from a minimization problem, the linear system is naturally symmetric positive definite (SPD). Finally, a FOSLS formulation provides a useful tool for adaptive mesh refinement (AMR), namely the FOSLS functional provides a "locally sharp, globally reliable error estimator" basically for free.[19].

The full-Stokes system, (2.3.9)-(2.3.11), is a second-order system that is posed with respect to velocity and pressure. However, it is important to note that it was derived from a naturally first-order system, (2.3.1)-(2.3.2, which can be solved for velocity and pressure by adding a set of equations that define $\underline{\underline{\sigma}}$ in terms of $\underline{u}$ and p. One reason for using the second-order system is that it reduces the number of unknowns by bypassing the need to solve for $\underline{\underline{\sigma}}$. This reveals one of the downsides to a FOSLS approach: requiring the PDE be first order tends to result in solving a larger system. In the case of the full-Stokes system, the second-order version has 3-4 unknowns depending on the number of spatial dimensions. In its first-order form, the gradient of velocity is used to define several new unknowns (4 for 2D and 9 for 3D), which describe the stresses of the system. With this increase in unknowns, storing the matrices that result from discretizing the system in memory can become an issue as the problem size increases.

Another criticism of FOSLS formulations are their reduced ability to maintain mass conservation. This is because the equations of a system are only minimized in an L^2 sense. There are special steps that can be taken to improve conservation if that is significantly more important than the other equations. These steps are detailed in [25, 24]. Finally, manipulating the first-order formulation into an H^1 equivalent system, can be difficult. Although continuity tends to be pretty easy to prove, coercivity requires particularly more attention and is discussed later in Section 6.3.

Let $\mathcal{L}(\mathbf{u}) = \mathbf{f}$ be the first-order system, where $\mathcal{L} : \mathcal{V} \to (L^2)^q$ is the nonlinear, first-order operator, $\mathcal{V}$ is an appropriate Hilbert space, and q is the number of equations. The solution to this system is found by finding $\mathbf{u}^*$ such that

$$\mathbf{u}^* = \underset{\mathbf{u}\in\mathcal{V}}{\operatorname{argmin}} ||\mathcal{L}(\mathbf{u}) - \mathbf{f}||_{L^2}. \tag{3.1.1}$$

The existance and uniquness of $\mathbf{u}^*$ is discussed later. One solution strategy to dealing with the

nonlinearity of $\mathcal{L}$ is Newton's method, which requires linearization about an approximation to the exact solution. For the formulations in this dissertation, the linearizion occurs at the PDE level, and the resulting linear problems are approximated using a FOSLS approach. This method is known as Newton-FOSLS.

To generate a Newton-FOSLS iteration, start by assuming $\mathbf{u}_k$ is the kth iterate of the solution, and expand the nonlinear operator around $\mathbf{u}_k + \delta\mathbf{u}$ using a Taylor series, where $\delta\mathbf{u}$ is an update to the solution,

$$\mathcal{L}(\mathbf{u}_k + \delta\mathbf{u}) = \mathcal{L}(\mathbf{u}_k) + \mathcal{L}'(\mathbf{u}_k)[\delta\mathbf{u}] + \frac{1}{2}\mathcal{L}''(\hat{\mathbf{u}}_k)[\delta\mathbf{u}, \delta\mathbf{u}], \tag{3.1.2}$$

where $\mathcal{L}'(\mathbf{u}_k)[\delta\mathbf{u}]$ is the first Fréchet derivative at $\mathbf{u}_k$ in the direction of $\delta\mathbf{u}$, $\mathcal{L}''[\delta\mathbf{u}, \delta\mathbf{u}]$ is the second Fréchet derivative at some point $\hat{\mathbf{u}}_k = \mathbf{u}_k + \alpha\delta\mathbf{u}$ for some $\alpha \in [0, 1]$. The Newton iteration is generated by dropping the second-order term and finding the update, $\delta\mathbf{u}_k$, such that:

$$\delta\mathbf{u}_k = \underset{\delta\mathbf{u}\in\mathcal{V}}{\operatorname{argmin}} ||\mathbb{L}_k\delta\mathbf{u} - R_k||_{L^2}, \tag{3.1.3}$$

where $\mathbb{L}_k = \mathcal{L}'(\mathbf{u}_k)$, $R_k = \mathbf{f} - \mathcal{L}(\mathbf{u}_k)$. The modification known as damped Newton is achieved by setting:

$$\mathbf{u}_{k+1} = \mathbf{u}_k + \alpha\delta\mathbf{u}_k,$$

where α is a line search parameter between [0,1] that will help ensure that the functional is always decreasing. An illustration of this process is found in Figure 3.1.

Solving the linearized system on each Newton step amounts to minimizing a quadratic functional, which has the equivalent weak variational form to find $\delta\mathbf{u}_k \in \mathcal{V}$ such that

$$\langle \mathbb{L}_k\delta\mathbf{u}_k, \mathbb{L}_k\mathbf{v}\rangle = \langle R_k, \mathbb{L}_k\mathbf{v}\rangle\,, \tag{3.1.4}$$

for all $\forall\mathbf{v} \in \mathcal{V}$ and $\langle\cdot,\cdot\rangle$ is the L^2 inner product. Using this weak variational form, define the bilinear form:

$$B_k(\mathbf{u}, \mathbf{v}) = \langle \mathbb{L}_k\delta\mathbf{u}, \mathbb{L}_k\mathbf{v}\rangle\,. \tag{3.1.5}$$

It is useful to show that B_k is $\mathcal{V}$-elliptic, which means it is coercive and continuous in the $\mathcal{V}$-norm

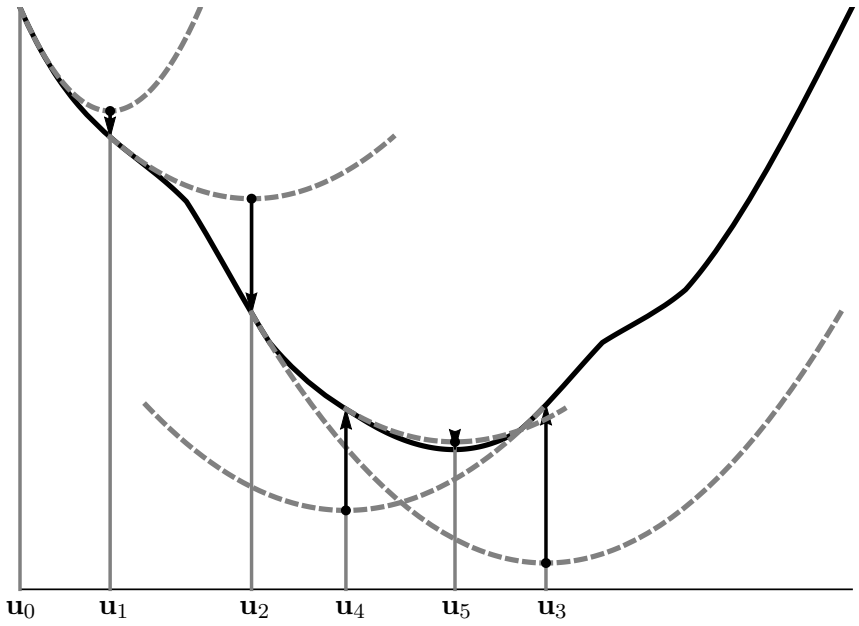

Figure 3.1: The solid black line is a representation of the least-squares functional. Each dotted gray line represents the quadratic functional resulting from a linearizion.

or, in other words, there exists constants $c_0, c_1 > 0$ Dependant only on $\mathbf{u}_k$ such that:

$$B_k(\mathbf{u}, \mathbf{v}) \leq c_1 \|\mathbf{u}\|_{\mathcal{V}} \|\mathbf{v}\|_{\mathcal{V}}, \qquad \text{(continuity)} \tag{3.1.6}$$

$$B_k(\mathbf{u}, \mathbf{u}) \geq c_0 \|\mathbf{u}\|_{\mathcal{V}}^2. \qquad \text{(coercivity)} \tag{3.1.7}$$

If the bilinear form is $\mathcal{V}$-elliptic, then B_k is a inner product on $\mathcal{V}$ and, by the Riesz representation theorem, there exists a unique solution, $\delta\mathbf{u}_k \in \mathcal{V}$, that satisfies (3.1.4). For the full-Stokes, ice-sheet system, continuity is straight forward to show and is found in Section 6.2. Coercivity on the other hand is more complected. If viscosity is bounded, coercivity can be established within a neighborhood of the solution. However, if viscosity is not bounded, determining if there is a space in which full-Stokes system is coercive remains an open question. This is discussed in Section 6.3.

In order to be useful, this method needs to be discretized. This is accomplished by first restricting the minimization in (3.1.1) to a discrete subspace, $\mathcal{V}^h \subset \mathcal{V}$. This, now discrete, nonlinear system is solved by restricting (3.1.3) and (3.1.4) to $\mathcal{V}^h$. This results in the discrete weak form: find $\delta\mathbf{u}_k^h \in \mathcal{V}^h$ given a discrete approximation $\mathbf{u}_k^h$ such that $\forall v^h \in \mathcal{V}^h$

$$\left\langle \mathbb{L}_k^h \delta\mathbf{u}_k^h, \mathbb{L}_k^h \mathbf{v}^h \right\rangle = \left\langle R_k^h, \mathbb{L}_k^h \mathbf{v}^h \right\rangle, \tag{3.1.8}$$

where $\mathbb{L}_k^h = \mathcal{L}'(\mathbf{u}_k^h)$, $R_k^h = \mathbf{f} - \mathcal{L}(\mathbf{u}_k^h)$, and $\mathbf{u}_k^h$ is the kth approximation to the true discrete solution. If ϕ_i is a set of basis vectors for $\mathcal{V}^h$, then (3.1.8) can be written as the linear system $A^h\mathbf{x}^h = \mathbf{b}^h$ where $(A^h)_{i,j} = \left\langle \mathbb{L}_k^h\phi_i, \mathbb{L}_k^h\phi_j \right\rangle$, $(\mathbf{b}^h)_i = \left\langle R_k^h, \mathbb{L}_k^h\phi_i \right\rangle$, and $\mathbf{x}^h = \delta\mathbf{u}_k^h$. If the bounds (3.1.6)-(3.1.7) hold for the discrete system, then there exists a unique solution to the discrete system, and additionally, the matrix A^h is symmetric positive definite.

3.2 Nested Iteration

To help speed up the nonlinear, Newton-FOSLS iteration, a strategy known as Nested Iteration (NI) is employed. The basic idea behind NI is to minimize the nonlinear functional using a finite element space of small dimension and then use this as a starting guess for minimization on a finite element space of larger dimension. A common way of increasing the dimension of the finite

element space is by refining the mesh on which the system is approximated and then defining a new finite element space on the refined mesh. For convenience, a mesh with a corresponding finite element space is refereed to as a level or grid.

The goal is that when the coarse grid solution is interpolated to the fine grid as an initial guess, the initial guess is close enough to the true solution on the fine grid that only a couple of Newton steps is required before the mesh is refined again [16, 18]. This process is repeated until either a certain tolerance is met or a desired fine mesh is achieved. The main benefit of an NI scheme is that most of the computation is done on coarse grids, which can be significantly cheaper than computation on the finest grid.

For a more rigorous definition of the NI method, let Ω^h be a mesh with spacing h and with corresponding finite element space defined on that mesh, $\mathcal{V}^h$. Let u_i^h and u_f^h be the initial and final solutions from the Newton-FOSLS solver on the mesh Ω^h. Starting out on a coarse grid, say $(\Omega^H, \mathcal{V}^H)$, with the initial guess u_i^H, Newton-FOSLS iterates until its stopping criteria is reached and yields the approximate solution, u_f^H. At this point a finer mesh, $\Omega^{\frac{H}{2}}$, and corresponding finite element space, $\mathcal{V}^{\frac{H}{2}}$, is generated through some process such adaptive refinement. The initial guess for Newton-FOSLS on this finer grid is generated by interpolating the coarse grid solution as follows $P_H^{\frac{H}{2}} u_f^H = u_i^{\frac{H}{2}}$, where $P_H^{\frac{H}{2}}$ is the interpolation operator from the coarse grid $(\Omega^H, \mathcal{V}^H)$ to the fine grid $(\Omega^{\frac{H}{2}}, \mathcal{V}^{\frac{H}{2}})$. The mesh and solution are repeatedly refined until the NI process reaches its stopping criteria. This method is known as NI-Newton-FOSLS and is illustrated in Figure 3.2.

Deciding not to perform another Newton-FOSLS iteration and, instead, refine the grid, is one of the more important decisions in making NI as efficient as possible. Let u_*^H be the true discrete solution on $(\Omega^H, \mathcal{V}^H)$ and u_* be the true continuous solution. This means best approximation to u_* on $(\Omega^H, \mathcal{V}^H)$ is u_*^H. One way to improve this approximation is to refine the mesh. Since iteration of Newton-FOSLS on $(\Omega^H, \mathcal{V}^H)$ only move the current solution closer to u_*^H, there there will come a point when refining the mesh reduces the error to the true continuous solution more than taking another Newton iteration. This point is when the coarse grid solution, u_k^H, is within discretization error of u_*^H [46]. There are basically two factors that make optimizing NI tricky. On one side,

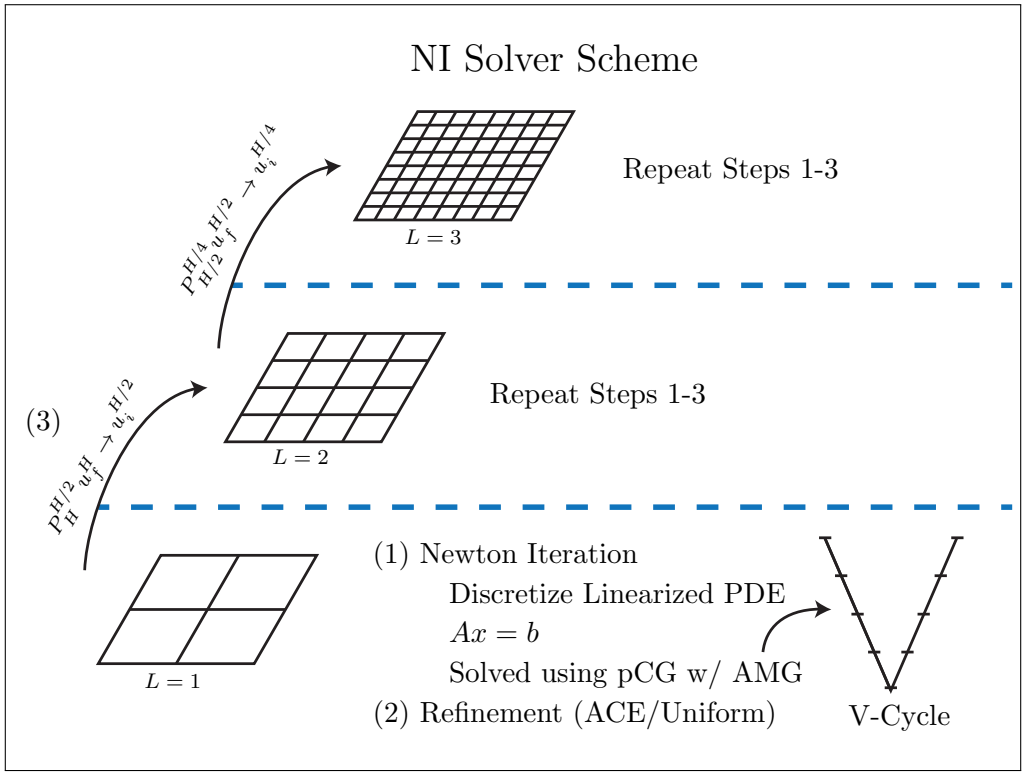

Figure 3.2: The Nested Iteration process involves solving a problem on a coarse grid, interpolating the solution to a finer grid and repeating. This depicts a linear solver involving multigrid, which is discussed in 3.3

Newton-FOSLS iterations on $(\Omega^H, \mathcal{V}^H)$ are computationally inexpensive. On the other side, these iteration can only converge to an approximation of the desired solution and refining the grid can improve this approximation. This is illustrated in Figure 3.3.

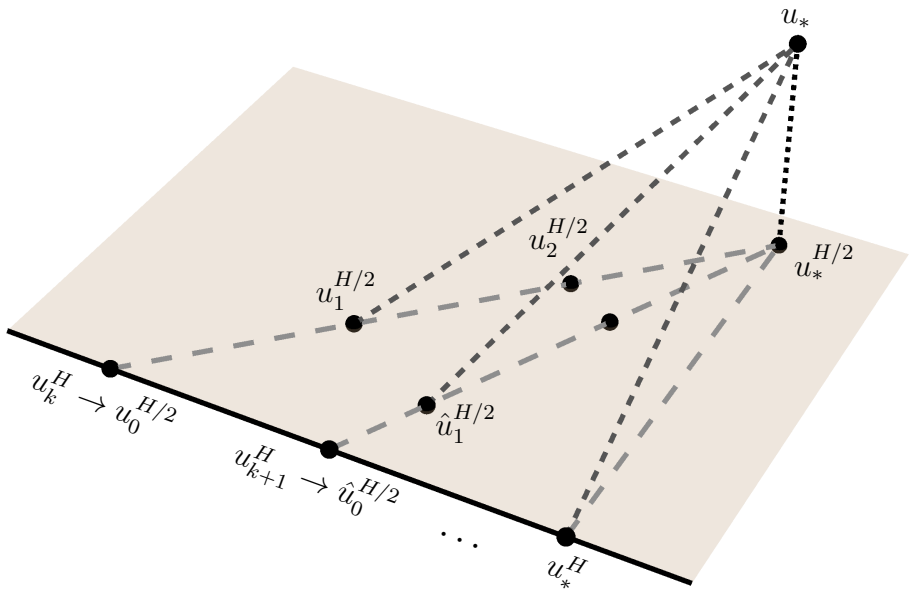

Figure 3.3: The black line represents the Hilbert space on the mesh Ω^H with the true discrete solution, u_*^H and the plane represents $\Omega^{H/2}$ with the true discrete solution, $u_*^{H/2}$. The true continuous solution is u_* and in reality should be much closer to $u^{H/2}$ since this figure is not to scale.

3.3 AMG

At the core of the Newton-FOSLS method is the linear solver that actually solves the FOSLS problem on each Newton iteration. Although many times a direct solver such as LU is used for debugging purposes, one of the goals of this dissertation is to apply an iterative solver to the full-Stokes, ice-sheet problem. Assuming the FOSLS system yields an H^1 elliptic operator, a multigrid method is an ideal choice of solver. Specifically, the main solver used in this dissertation is a Conjugate Gradient (CG) method preconditioned with Algebraic Multigrid (AMG). Before discussing AMG, the basics of multigrid in general will be discussed. For more detail on multigrid

and AMG see [11]

There are three main parts to a multigrid process: relaxation/smoothing, restriction, and interpolation. The first two parts help to reduce different components of the error. Relaxation works well at reducing the high frequency modes of the error. The performance of Relaxation starts to degrade as the smooth modes begin to dominate the high frequency modes. Restriction takes smooth modes on the fine grid and approximates them on a coarse grid where problem is solved using less work than on the fine grid. Interpolation is use to transfer a coarse grid correction to a finer grid.

The general idea is to relax on a grid until error reduction has stalled. Then, restrict the error down to a courser grid and relax on the residual equation until relaxation stall again. Repeat this process recursively until the grid is course enough to do a direct solve. Apply coarse grid corrections back up through the finer grids using interpolation. Repeat this entire process until a satisfactory solution is reached.

In more depth, multigrid starts off by posing the problem:

$$Ax = b,$$

where A is an $n_f \times n_f$ fine grid matrix and x, b are vectors of length n_f. The f in this case refers to the size of the fine grid. The residual is defined as:

$$r = b - Ax.$$

If x is the current approximate solution and x^* is the true solution, then the residual equation is:

$$Ae = r,$$

where $e = x^* - x$. Applying an approximation to the inverse of A to the residual equation, gives an approximation to the error, which can be used to update the solution. This approximate inverse will be the multigrid process and the update to the solution is:

$$x \leftarrow x + \hat{e},$$

where $\hat{e}$ is the approximation of the error, e.

The first step is to apply ν sweeps of a smoother such as Jacobi or Gauss-Seidel, S_ν. This creates the approximate error, $\hat{e}_\nu = S_\nu r$. The smoothing process eliminates the high frequency modes rapidly, leaving only smooth error. Unfortunately, this causes the smoothing process to slow down considerably, so simply smoothing is not enough. When this happens, it is time to restrict down to a coarser grid, where computation is cheaper.

Let R be an $n_c \times n_f$ operator representing restriction and P be an $n_f \times n_c$ operator representing interpolation, where c refers to the size of the coarse grid. The residual is restricted down to the course grid by $r_\nu^c = RA\hat{e}_\nu$, and the coarse grid error is computed by approximately solving,

$$A^c \hat{e}_\nu^c = r_\nu^c,$$

where A^c is the $n_c \times n_c$ coarse grid operator. This coarse error is brought back up to the fine grid by $\hat{e}^f = P\hat{e}_\nu^c$, since it is assumed that the fine grid error is easily approximated by interpolation of the coarse grid error. To mitigate any mistake introduced by the interpolation, μ smoother sweeps are preform to get the final approximation of the error,

$$\hat{e} = S_\mu A \hat{e}^f.$$

Putting all of these steps together yields a scheme for a single coarse grid correction with ν pre-smoothings and μ post-smoothings:

$$x \leftarrow x + \left[S_\nu AP(A^c)^{-1}RAS_\nu\right] r. \tag{3.3.1}$$

A useful part of this coarse-grid correction is that it can be applied recursively to the system, $A^c\hat{e}_\nu^c = r_\nu^c$. This is repeated until the coarse grid system is small enough to be easily solve by a direct solver. Recursively applying coarse grid corrections in this manner is known as a V-Cycle and is illustrated in Figure 3.4. To indicated the number of pre- and post-smoothings, the cycle is often referred to as a V(ν, μ)-Cycle. Another common cycle is the W-Cycle, where multiple V-Cycles are taken on each level. This is also illustrated in Figure 3.4.

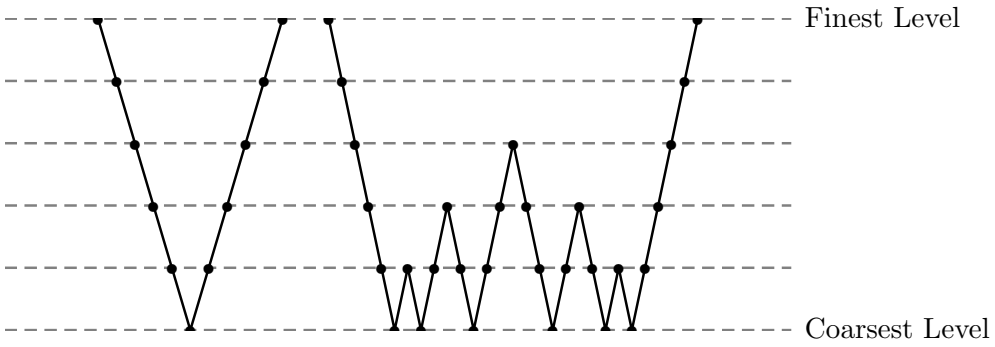

Figure 3.4: This graphic depicts showing V-Cycles and W-Cycles.

There are still three parts of the algorithm that have yet to be explained, that is the construction of A^c, R, and P. One way to construct A^c is by simply using the restriction and interpolation operators such that:

$$A^c = RAP,$$

where $R = P^T$. This way, all that remains to define a coarse grid correction is to define interpolation, P.

There are numerous ways to do this and each definition of P produces a different flavor of multigrid. The method used in this dissertation is AMG. The interpolation operator in AMG is built with the goal of accurately representing algebraically smooth error, e_s, where $S^{-1}Ae_s \approx 0$, where S^{-1} is some smoother that is approximating A^{-1}. In other words, algebraically smooth error is the error that cannot be resolved with smoothing. With this in mind, the interpolation operator takes the coarse grid error to the fine grid via:

$$e_i^f = (Pe^c)_i = \begin{cases} e_i^c & i \in C \\ \sum_{j \in C_i} w_{ij} e_j^c & i \in F \end{cases}, \tag{3.3.2}$$

where C is the collection of coarse grid points, F is the collection of fine grid points, w_{ij} is the interpolation weight between coarse point j to fine point i, and C_i is the collection of strongly connected coarse point that influence the fine point i. The choice of C, F, C_i, and w_{ij} is determined by examining the entries of A and is further explained in [11].

3.4 AMS

Another potential preconditioner for the FOSLS formulation of the full-Stokes, ice-sheet model is know as the auxiliary space Maxwell solver (AMS). AMS is a general algebraic solver that is based on HX decompositions and uses AMG to solve second-order definite/semi-definite equations of the form

$$a_{curl}(\mathbf{u}, \mathbf{v}) = (\alpha \nabla \times \mathbf{u}, \nabla \times \mathbf{v}) + (\beta \mathbf{u}, \mathbf{v}) \,,$$

with $\alpha > 0$ and $\beta \geq 0$ [27].

Another interesting and related system is $\nabla \cdot \beta \nabla \mathbf{u} - \alpha \mathbf{u} = \mathbf{f}$ This is often referred to as the "grad-div" system and has the following variational form:

$$a_{div}(\mathbf{u}, \mathbf{v}) = (\beta \nabla \cdot \mathbf{u}, \nabla \cdot \mathbf{v}) + (\alpha \mathbf{u}, \mathbf{v}) \,.$$

This operator has the near-null space of curl fields. If $\mathbf{u} = \nabla \times \mathbf{\Phi}$ and $\mathbf{v} = \nabla \times \mathbf{\Psi}$, then

$$a_{div}(\mathbf{u}, \mathbf{v}) = (\alpha \nabla \times \mathbf{\Phi}, \nabla \times \mathbf{\Psi}) \approx a_{curl}(\mathbf{\Phi}, \mathbf{\Psi}).$$

AMS was designed to solve problems of this type given an appropriate finite element discretization such as Raviart-Thomas elements [44].

It can be shown that a full-stress formulation for the full-Stokes model has a formal-normal with two grad-div systems followed by a Laplace operator along the block diagonal. One method of solving a system like this, is to construct a block preconditioner comprised of two AMS and one AMG solves. The advantage solving Stokes via this method is that an $H(\text{div})$ space can be used as opposed to the H^1 space that AMG requires. The $H(\text{div})$ space requires the less regularity out of the solution than an H^1 space, which may prove beneficial in places where viscosity becomes infinite.

Chapter 4

Inverse Problem

This chapter describes a side project that involves using surface velocity data and Stoke equations to predict the basal topography of a glacier. The Kennicott glacier is a temperate glacier located in southeast Alaska. Using elevation and velocity data acquired from high resolution satellite imagery, the basal topography of a cross section of the Kennicott is approximated. The normal method for determining ice thickness is to use ice penetrating radar. However, since the Kennicott glacier is a temperate glacier, its higher water content causes these readings to be unreliable. A different method is to use Stokes-equations as a forward model and attempt to approximate the basal topography by comparing recorded data to modeled surface velocities from various test domains.

A simplification of Equation (2.3.2) comes from making two assumptions. First, assume that u_1 is the only non-negligible velocity component. Essentially, $\underline{u} = [u_1, 0, 0]^T$, where u_1 is the down-glacier velocity. Second, stress and strain rate tensors do not vary with x. In this case the x-direction is down glacier, the y-direction is cross glacier, and the z-direction is depth. In this reference frame, gravity is $\underline{g} = [|g|\sin(\theta), 0, -|g|\cos(\theta)]^T$ where θ is the slope of the glacier.

With these assumptions, the strain rate tensor becomes

$$\dot{\underline{\underline{\varepsilon}}} = \frac{1}{2}\left(\nabla\underline{u} + (\nabla\underline{u})^T\right) = \frac{1}{2}\begin{bmatrix} 2\frac{\partial u_1}{\partial x} & \frac{\partial u_1}{\partial y} + \frac{\partial u_2}{\partial x} & \frac{\partial u_1}{\partial z} + \frac{\partial u_3}{\partial x} \\ \frac{\partial u_1}{\partial y} + \frac{\partial u_2}{\partial x} & 2\frac{\partial u_2}{\partial y} & \frac{\partial u_2}{\partial z} + \frac{\partial u_3}{\partial y} \\ \frac{\partial u_1}{\partial z} + \frac{\partial u_3}{\partial x} & \frac{\partial u_2}{\partial z} + \frac{\partial u_3}{\partial y} & 2\frac{\partial u_3}{\partial z} \end{bmatrix} = \frac{1}{2}\begin{bmatrix} 0 & \frac{\partial u_1}{\partial y} & \frac{\partial u_1}{\partial z} \\ \frac{\partial u_1}{\partial y} & 0 & 0 \\ \frac{\partial u_1}{\partial z} & 0 & 0 \end{bmatrix}. \quad (4.0.1)$$

This corresponds to neglecting the $s_{11},\ s_{22},\ s_{33},\ s_{23}$ components in the deviatoric stress, Equation (2.3.4). The continuity equation (2.3.1) is automatically satisfied under these assumptions. In the

momentum equation, velocity and pressure become completely decoupled allowing us to solve for just velocity using:

$$\frac{\partial}{\partial y}\left(\mu\frac{\partial u_1}{\partial y}\right)+\frac{\partial}{\partial z}\left(\mu\frac{\partial u_1}{\partial z}\right)=\nabla\cdot(\mu\nabla u_1)=-|g|\sin(\theta). \tag{4.0.2}$$

This is simply a nonlinear Poisson equation. The boundary conditions for this problem are no-slip where the glacier meets the bed and no-stress on the surface of the glacier. This simplified model is the basis for the forward model used to approximate the basal topography and estimate summer sliding.

The velocity field calculated from the imagery acquired by the WorldView and SPOT satellites can be found in Figure 4.1 [8]. The line indicated on this figure is where the inversion was attempted.

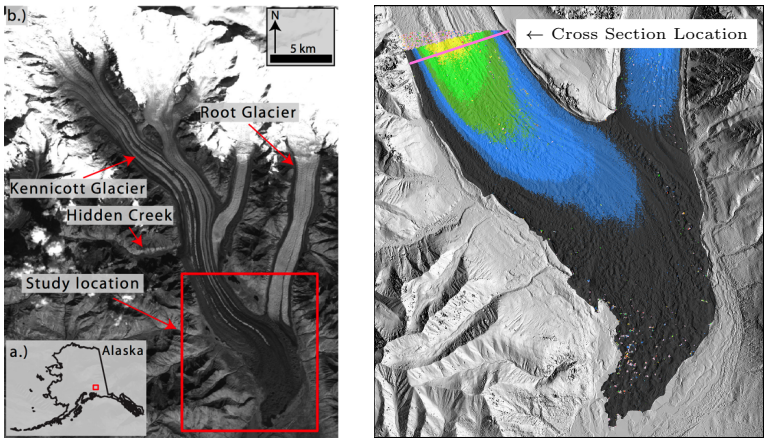

Figure 4.1: Left: a) The Kennicott glacier, b) Location of the Kennicott glacier in Alaska. Right: The spring velocity map of the Kennicott glacier with a pink line indicating the location of the cross section used in the inverse problem.

To solve for the basal geometry, a test domain is used in conjunction with the forward problem in Equation (4.0.2) to produce a surface velocity profile. The L^2 error of the calculated velocities and those observed by the satellite imagery is then calculated. Due to the relatively small nature of the domains, a simple LU Solver on Galerkin discretization using Taylor-Hood elements is used solve the forward problem [31]. The optimal domain is found by minimizing this L^2 error within the parameter space from which the domain was chosen, which is depicted in Figure 4.2.

The test domains are generated by two power law functions. Both function are uniquely

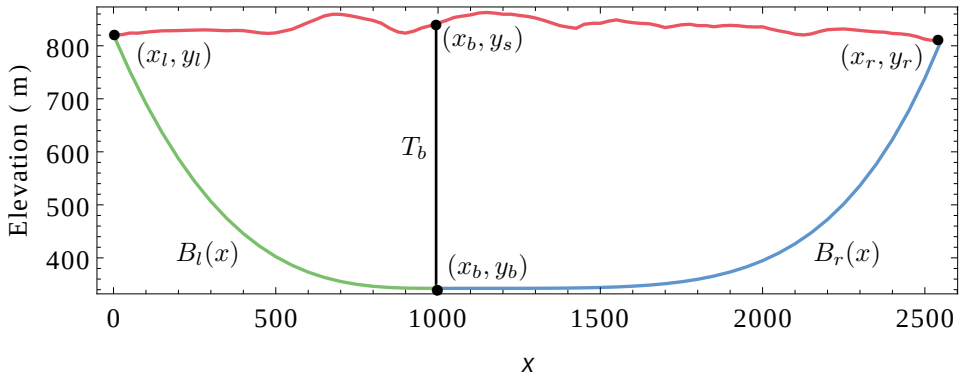

Figure 4.2: A depiction of the parameter space.

determined by eleven parameters: four points, two power parameters, and a thickness value. All but four of these parameters are fixed by the elevation data from the satellite imagery. Those four parameters are a break point, x_b, ice thickness at the break point, T_b, and the left/right powers, γ_l, γ_r. The equations that define the basal topography are:

$$B_l(x) = (y_l - y_b)\left(\frac{x_b - x}{x_b - x_l}\right)^{\gamma_l} + y_b,$$

$$B_r(x) = (y_r - y_b)\left(\frac{x_b - x}{x_b - x_r}\right)^{\gamma_r} + y_b,$$

where $y_b = y_s - T_b$.

This parameter space was chosen for its smooth nature, small dimension, and its general shape, which is similar to what would be expected from a valley glacier [36]. Since the domain is broken up into two power functions, this parameter space has the added benefit of being able to capture the non-symmetric velocity profile given by the observed data. An near-optimal domain and corresponding velocity profiles can be found in Figure 4.3. This domain was used to evaluate how various basal sliding models explain summer speed up.

The WorldView data was also used to collect velocity profiles for the summer. The summer data showed a significant increase in speed throughout the length of the cross section. This was due to ice melt as well as basal sliding. Assuming that the spring velocity data accounted for the glacial melt, subtracting the spring data from the summer data, provided an estimate of the basal sliding in the summer. The next part of this research was to attempt to use the domain generated

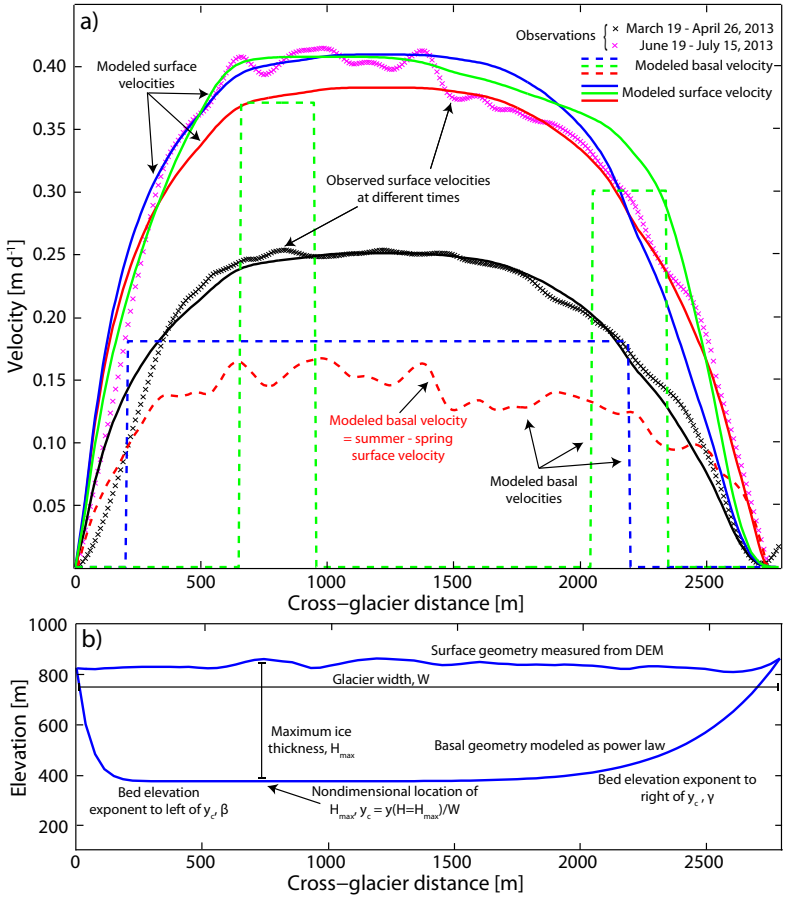

Figure 4.3: Top: Observed velocity profiles and computed velocity profiles with various sliding models for both spring and summer data. Bottom: The hand tuned near-optimal domain.

by the spring data and various models for basal sliding to match the summer velocities.

Three different basal sliding models were used. All of these models involved directly enforcing a basal velocity profile as a boundary condition on the bed. The first profile, the blue lines in Figure 4.3, was a large, uniform slippery patch with a velocity 0.18 m d^{-1}. The second profile, the green lines in Figure 4.3, had two smaller but faster slippery patches, which attempted to recover the asymmetry in the summer velocity profile. The left patch's velocity was 0.37 m d^{-1} and the right patch's velocity was 0.30 m d^{-1}. The final profile, the red lines in Figure 4.3, was created by subtracting the spring velocity from the summer velocity and then directly enforcing the result as the boundary condition on the bed. This was known as the speedup profile and is common practice for estimating basal sliding.

It should be noted that the methods with slippery patches involved enforcing a discontinuous boundary condition. This would create singularities at these discontinuities. Since solver performance was not a concern for this project, these singularities were dealt with by simply having a fine enough mesh that their effect on the solution was minimal.

Of the three basal sliding models, the two slippery patches performed the best with an RMSE of 0.0229 m d^{-1}. The model that performed the worst was the uniform patch with an RMSE of 0.0299 m d^{-1}. The speedup profile had an RMSE of 0.0244 m d^{-1}. As a point of comparison, the RMSE between the observed spring velocities and the spring velocities modeled by (4.0.2) using the best basal topography from the parameter space in Figure 4.2 was 0.0155 m d^{-1}.

It is important to notice that all three basal sliding models produced summer velocity profiles that were comparable accurate. This implies that the exact basal sliding is not necessary in these types of glacier models. Choosing to use the difference between summer and spring velocities as the basal velocity is an adequate and easily implemented method. See [6], submitted to the Journal of Glaciology, for further details.

Chapter 5

Stokes Formulations

This chapter describes the various formulations of the full-Stokes equations used in this dissertation.

5.1 Taylor-Hood Galerikin Model

This section will discuss the Taylor-Hood Galerkin model as described in [30]. The solutions from this model will be compared to the solutions from various FOSLS formulations below. First, define Ω as the domain of the ice-sheet with $\Gamma = \Gamma_s + \Gamma_b + \Gamma_p$ as the surface, bed and periodic portions of the boundary. Additionally, let $(H^1(\Omega))^d$ be a vector Hilbert space of d functions where each function and its first derivatives are square integrable.

This method starts off by taking the momentum, (2.3.2), and continuity, (2.3.9), combined with equation for the full stress, (2.3.3), to get the system:

$$\nabla \cdot \underline{\underline{s}} - \nabla \hat{p} = \underline{f}, \tag{5.1.1}$$

$$\nabla \cdot \underline{u} = 0, \tag{5.1.2}$$

Multiplying first equation by the test functions, $\underline{v} \in (H^1(\Omega))^d$, and preforming the proper integration by parts yields:

$$\int_\Omega \underline{\underline{s}} : \nabla \underline{v}\, dx - \int_\Omega p \nabla \cdot \underline{v}\, dx - \int_\Gamma n \cdot \underline{\underline{\sigma}} \cdot \underline{v}\, ds = \int_\Omega \underline{f} \cdot \underline{v}\, dx. \tag{5.1.3}$$

It can be shown that from the symmetry of $\underline{\underline{s}}$ and Equation 2.3.4 that,

$$\int_\Omega \underline{\underline{s}} : \nabla \underline{v}\, dx = \int_\Omega 2\mu_u \underline{\underline{\dot{\varepsilon}}}_u : \underline{\underline{\dot{\varepsilon}}}_v, dx,$$

where μ_u is the viscosity dependent on $\underline{u}$ and $\dot{\underline{\underline{\varepsilon}}}_u$ is the symmetric gradient of $\underline{u}$.

The boundary functional is eliminated by using the proper boundary conditions. On the surface, Γ_s, $n \cdot \underline{\underline{\sigma}} = 0$ is enforced, which results in $\int_{\Gamma_s} n \cdot \underline{\underline{\sigma}} \cdot \underline{v}\, ds = 0$. Periodic boundaries are enforce on Γ_p if it is present. In the case of a no-slip basal boundary condition, $\underline{u} = 0$ is enforced on Γ_b. These boundary conditions are built into the trial space by defining:

$$(H_0^1(\Omega))^d = \left\{ \underline{u} \in (H^1(\Omega))^d \middle| \, \underline{u}\,(\Gamma_b) = 0, \, \underline{u} \text{ is periodic on } \Gamma_p \right\} \tag{5.1.4}$$

This results in $\int_{\Gamma_p} n \cdot \underline{\underline{\sigma}} \cdot \underline{v}\, ds = 0$ and $\int_{\Gamma_b} n \cdot \underline{\underline{\sigma}} \cdot \underline{v}\, ds = 0$, and the boundary functional is completely eliminated. The case where there is a basal slip boundary condition is discussed in Section 9.1.

The weak variational form becomes: find $\underline{u} \in (H_0^1(\Omega))^d$ and $p \in L^2(\Omega)$ such that

$$\begin{aligned} \int_\Omega 2\mu_u \dot{\underline{\underline{\varepsilon}}}_u : \dot{\underline{\underline{\varepsilon}}}_v \, dx - \int_\Omega p \nabla \cdot \underline{v}\, dx &= \int_\Omega \underline{f} \cdot \underline{v}\, dx, \\ - \int_\Omega q \nabla \cdot \underline{u}\, dx &= 0 \end{aligned} \tag{5.1.5}$$

for all $\underline{v} \in (H_0^1(\Omega))^d$ and $q \in L^2(\Omega)$.

The weak form is satisfied uniquely by the solution of the equations (5.1.1) and (5.1.2). An approximation is produced by restricting the weak form to finite element spaces. In order to guarantee stability of the discrete equations, the finite element spaces must satisfy the LLB conditions discussed in 3.1. Toward that end, the velocity functions, $\underline{u}$ and $\underline{v}$, are choose from a quadratic finite element space and the pressure functions, p and q, are chosen from a linear finite element space [23]. This pair is usually $\mathcal{P}_2$-$\mathcal{P}_1$, where $\mathcal{P}_2$ is the set of piecewise quadratic Lagrange polynomials and $\mathcal{P}_1$ is the set of piecewise linear Lagrange polynomials on a discretization of Ω. This element pair is also known as the Taylor-Hood elements.

5.2 Velocity-Gradient Viscosity Formulation

In the FOSLS approach, the first step is to revert equations (2.3.9 - 2.3.10) back to a convenient first-order system. One way to initiate this process is by defining

$$\underline{\underline{U}} = \nabla \underline{u} = \begin{bmatrix} \frac{\partial u_1}{\partial x} & \frac{\partial u_2}{\partial x} & \frac{\partial u_3}{\partial x} \\ \frac{\partial u_1}{\partial y} & \frac{\partial u_2}{\partial y} & \frac{\partial u_3}{\partial y} \\ \frac{\partial u_1}{\partial z} & \frac{\partial u_2}{\partial z} & \frac{\partial u_3}{\partial z} \end{bmatrix} = \begin{bmatrix} U_{11} & U_{21} & U_{31} \\ U_{12} & U_{22} & U_{32} \\ U_{13} & U_{23} & U_{33} \end{bmatrix}.$$

Since this new set of unknowns is based on the velocity gradient and the curl of a gradient is zero, the system can be augmented with an additional equation, $\nabla \times \underline{\underline{U}} = 0$. The continuity equation written in terms of the new variable is $\text{Trace}(\underline{\underline{U}}) = 0$. Therefore, the solution of (2.3.9-(2.3.10) satisfies the following first-order system, which we will refer to as the **viscosity formulation**:

$$\nabla \cdot \underline{u} = 0, \qquad \text{(Continuity)}, \tag{5.2.1}$$

$$\underline{\underline{U}} = \nabla \underline{u}, \qquad \text{(Definition)}, \tag{5.2.2}$$

$$\nabla \cdot \hat{\mu} \left(\underline{\underline{U}} + \underline{\underline{U}}^T \right) - \nabla \hat{p} = \underline{f}, \qquad \text{(Momentum)}, \tag{5.2.3}$$

$$\nabla \times \underline{\underline{U}} = 0, \qquad \text{(Curl of a gradient)}, \tag{5.2.4}$$

$$\nabla \text{Trace}(\underline{\underline{U}}) = 0, \qquad \text{(Derived fron (5.2.1), (5.2.2))}. \tag{5.2.5}$$

A solution that satisfies equations (5.2.1) - (5.2.3) clearly must also solve equations (5.2.4) and (5.2.5). These equations are added to modify the norm in which the solution is approximated.

This system can be solved in two stages. Equations (5.2.3) - (5.2.5) are used to calculate the velocity gradient, $\underline{\underline{U}}$, and pressure, p. Then, Equations (5.2.1) - (5.2.2) retrieve the velocities, $\underline{u}$, from the velocity gradient. For 2-D problems in the xz-plane, the trace condition is readily enforced by explicitly setting $U_{33} = -U_{11}$. With $\mu = 1$ this system is H^1 equivalent with velocity boundary conditions as shown in [14]. The proof therein can be modified to establish H^1 equivalence when μ is a given function for which both $\|\mu\|_\infty$ and $\|\nabla\mu\|_\infty$ are bounded.

5.3 Velocity-Gradient Fluidity Formulation

In this section, an alternative, 2-D FOSLS formulation is developed in which the viscosity is absorbed into the velocity gradient. The effective strain rate can be written as

$$\dot{\varepsilon}_e = \frac{1}{\sqrt{2}} \left|\left|\underline{\underline{\dot{\varepsilon}}}\right|\right|_F = \left(\frac{1}{2} \left\langle \underline{\underline{E}}\,\underline{U}, \underline{\underline{E}}\,\underline{U} \right\rangle\right)^{\frac{1}{2}},$$

where

$$\underline{\underline{E}} = \frac{1}{2}\begin{bmatrix} 2 & 0 & 0 & 0 \\ 0 & 1 & 1 & 0 \\ 0 & 1 & 1 & 0 \\ 0 & 0 & 0 & 2 \end{bmatrix}, \quad \text{and} \quad \underline{U} = \begin{bmatrix} U_{11} \\ U_{21} \\ U_{12} \\ U_{22} \end{bmatrix}.$$

To make this calculation simpler, $\underline{U}$ is just $\underline{\underline{U}}$ written as a vector. Unlike the 3-D system in (5.2.1)-(5.2.5) where the subscripts 1, 2, and 3 corresponded with x, y, and z, this 2-D system just uses 1 and 2 which refers to x and z. Using these definitions, viscosity can be written as:

$$\hat{\mu} = \left\langle \underline{\underline{E}}\,\underline{U}, \underline{\underline{E}}\,\underline{U} \right\rangle^{-\frac{1}{3}}.$$

Now, Consider the new set of variables,

$$\hat{U} = \left\langle \underline{\underline{E}}\,\underline{U}, \underline{\underline{E}}\,\underline{U} \right\rangle^{-\frac{1}{3}} U,$$

where,

$$\underline{\hat{U}} = \begin{bmatrix} \hat{U}_{11} \\ \hat{U}_{12} \\ \hat{U}_{21} \\ \hat{U}_{22} \end{bmatrix}, \quad \text{or} \quad \underline{\underline{\hat{U}}} = \begin{bmatrix} \hat{U}_{11} & \hat{U}_{21} \\ \hat{U}_{12} & \hat{U}_{22} \end{bmatrix}.$$

Additionally, define

$$\phi = \left\langle \underline{\underline{E}}\,\underline{\hat{U}}, \underline{\underline{E}}\,\underline{\hat{U}} \right\rangle.$$

Notice that

$$\phi = \left\langle \underline{\underline{E}}\,\underline{\hat{U}}, \underline{\underline{E}}\,\underline{\hat{U}} \right\rangle = \left\langle \underline{\underline{E}}\,\underline{U}, \underline{\underline{E}}\,\underline{U} \right\rangle^{-\frac{2}{3}} \left\langle \underline{\underline{E}}\,\underline{U}, \underline{\underline{E}}\,\underline{U} \right\rangle = \left\langle \underline{\underline{E}}\,\underline{U}, \underline{\underline{E}}\,\underline{U} \right\rangle^{\frac{1}{3}}.$$

With these definitions, ϕ can be easily written in terms of either set of variables, which will allow the system of equations to be written entirely in the new set of variables. To transform back to the

original set of variables, multiply by ϕ, that is, $\phi\underline{\underline{\hat{U}}} = \underline{\underline{U}}$. Writing ϕ explicitly in terms of the new variables yields,

$$\phi = \frac{1}{2}\hat{U}_{11}{}^{2} + \frac{1}{4}\hat{U}_{12}^2 + \frac{1}{2}\hat{U}_{21}\hat{U}_{21} + \frac{1}{4}\hat{U}_{21}^2 + \frac{1}{2}\hat{U}_{22}^2.$$

The trace condition of U implies a trace condition on $\hat{U}$, which yields $\hat{U}_{22} = -\hat{U}_{11}$. Thus, ϕ simplifies further to:

$$\phi = \hat{U}_{11}^2 + \frac{1}{4}\hat{U}_{12}^2 + \frac{1}{2}\hat{U}_{21}\hat{U}_{21} + \frac{1}{4}\hat{U}_{21}^2.$$

Thus, the velocity-gradient fluidity formulation is expressed as:

$$\nabla \cdot \underline{u} = 0, \tag{5.3.1}$$

$$\phi\underline{\underline{\hat{U}}} = \nabla\underline{u}, \tag{5.3.2}$$

$$\nabla \cdot \left(\underline{\underline{\hat{U}}} + \underline{\underline{\hat{U}}}^T\right) - \nabla\hat{p} = \underline{f}, \tag{5.3.3}$$

$$\nabla \times \phi\underline{\underline{\hat{U}}} = 0. \tag{5.3.4}$$

However, this introduces a new problem occurring in Equation (5.3.4). The balance between the divergence Equation (5.3.3) and the curl Equation (5.3.4) is not maintained when ϕ goes to zero. It is well known that having these two equations of the same scale will produce better AMG performance. This is resolved by multiplying Equation 5.3.4 by $1/\phi$. However, to avoid yet another singularity, a small constant is added to this scaling, $\frac{1}{\phi+c}$. Since the entire equation is scaled by this factor, the actual solutions remains unchanged, as opposed to the the method of fixing the singularity found in Equation 2.3.12, which actually changes the overall solution. In regions where $\phi << c$ the div and curl equations are once again unbalanced. However, these will be the regions where the solution, $\underline{\underline{\hat{U}}}$, is essentially zero and $\underline{u}$ is constant, so the solvers should not have much difficulty.

The last modification made to Equation (5.3.4) is to use the product rule. Doing this yields:

$$\frac{\phi}{\phi + c}\nabla \times \underline{\underline{\hat{U}}} - \frac{1}{\phi + c}\left(\nabla^{\perp}\phi\right)^T \cdot \underline{\underline{\hat{U}}} = 0, \tag{5.3.5}$$

where

$$\nabla^{\perp} = \begin{bmatrix} \partial z \\ -\partial x \end{bmatrix} \quad \text{or} \quad \begin{bmatrix} \partial z & -\partial x & 0 & 0 \\ 0 & 0 & \partial z & -\partial x \end{bmatrix},$$

depending on the situation. This form is helps the linear solver converge faster since it has an nearly unscaled curl term with some lower order terms.

Another problem with this fluidity formulation is that it does not allow the solution to have pure rotations in some local region. Consider the simple velocity profile is some local region:

$$\begin{aligned} u_1 &= c_1 z + c_2, \\ u_2 &= -c_1 x + c_3, \end{aligned} \tag{5.3.6}$$

where c_1 is some nonzero constant and $c_2,\ c_3$ are just any constant. Then in that region,

$$\begin{aligned} \nabla \cdot \underline{u} &= 0, \\ \underline{\underline{U}} = \nabla \underline{u} &= \begin{bmatrix} 0 & c_1 \\ -c_1 & 0 \end{bmatrix}, \\ \underline{\underline{\dot{\varepsilon}}} &= \frac{1}{2}\left(\underline{\underline{U}} + \underline{\underline{U}}^T\right) = \underline{\underline{0}}, \\ \phi &= \left\langle \underline{\underline{E}}\,\underline{U}, \underline{\underline{E}}\,\underline{U} \right\rangle^{\frac{1}{3}} = 0. \end{aligned} \tag{5.3.7}$$

This means that equation (5.3.2) becomes,

$$\begin{bmatrix} 0 & 0 \\ 0 & 0 \end{bmatrix} = \begin{bmatrix} 0 & c_1 \\ -c_1 & 0 \end{bmatrix},$$

which is clearly not possible. This is why the stress-vorticity fluidity formulation is developed in Section 5.4.

5.4 Stress-Vorticity Fluidity Formulations

In this section another 2-D FOSLS formulation is developed in which the deviatoric stress is used as the new set up unknowns. The 2-D models are framed in (x, z) space with the x-direction being downstream and the z-direction being height.

Another way to convert equations (2.3.9) - (2.3.9) into a first-order system is to break up the tensor $\underline{\underline{s}} = 2\hat{\mu}\underline{\underline{\dot{\varepsilon}}}$ into four variables.

$$\begin{aligned}
\underline{\underline{s}} &= 2\hat{\mu}\underline{\underline{\dot{\varepsilon}}} \\
&= \hat{\mu}\left(\nabla u + (\nabla u)^T\right) \\
&= \begin{bmatrix} 2\hat{\mu}\partial_x u_1 & \hat{\mu}(\partial_z u_1 + \partial_x u_2) \\ \hat{\mu}(\partial_z u_1 + \partial_x u_2) & 2\hat{\mu}\partial_z u_2 \end{bmatrix}
\end{aligned}$$

Using equation (2.3.1), $2\partial_x u_1$ can be written as $\partial_x u_1 - \partial_z u_2$. Thus,

$$\begin{aligned}
\underline{\underline{s}} &= \begin{bmatrix} \hat{\mu}(\partial_x u_1 - \partial_z u_2) & \hat{\mu}(\partial_z u_1 + \partial_x u_2) \\ \hat{\mu}(\partial_z u_1 + \partial_x u_2) & \hat{\mu}(\partial_z u_2 - \partial_x u_1) \end{bmatrix} \\
&= \begin{bmatrix} s_{11} & s_{12} \\ s_{12} & -s_{11} \end{bmatrix}.
\end{aligned}$$

Next, define the fluidity as $\phi = \hat{\mu}^{-1}$. Then,

$$\begin{aligned}
\phi s_{11} &= \partial_x u_1 - \partial_z u_2, \\
\phi s_{12} &= \partial_z u_1 + \partial_x u_2.
\end{aligned}$$

To determine what ϕ is in terms of s_{11} and s_{12}, start with the definition of $\hat{\mu}$ from equation (2.3.11),

$$\hat{\mu}^{-1} = ||\underline{\underline{\dot{\varepsilon}}}||_F^{\frac{2}{3}} = ||\underline{\underline{\dot{\varepsilon}}}||_F^{-\frac{4}{3}} ||\underline{\underline{\dot{\varepsilon}}}||_F^2 = \hat{\mu}^2 ||\underline{\underline{\dot{\varepsilon}}}||_F^2 = ||\hat{\mu}\underline{\underline{\dot{\varepsilon}}}||_F^2 = \left|\left|\frac{s}{2}\right|\right|_F^2 = \frac{{s_{11}}^2 + {s_{12}}^2}{2} = \phi. \tag{5.4.1}$$

The system can now be rewritten in terms of s_{11} and s_{12} to get the deviatoric-stress/pressure/velocity form,

$$\phi s_{11} - (\partial_x u_1 - \partial_z u_2) = 0, \tag{5.4.2}$$

$$\phi s_{12} - (\partial_z u_1 + \partial_x u_2) = 0, \tag{5.4.3}$$

$$\partial_x u_1 + \partial_z u_2 = 0, \tag{5.4.4}$$

$$-\partial_x s_{11} - \partial_z s_{12} + \partial_x \hat{p} - f_1 = 0, \tag{5.4.5}$$

$$\partial_z s_{11} - \partial_x s_{12} + \partial_z \hat{p} - f_2 = 0, \tag{5.4.6}$$

where $\underline{f} = [f_1, f_2]$. This system is known as the **basic fluidity formulation** throughout the rest of this paper since fluidity is the quantity associated with the inverse of viscosity. Here, equations (5.4.2) - (5.4.3) are analogous to equation (5.2.2) in the viscosity formulation, equation (5.4.4) is just continuity again, and equations (5.4.5) - (5.4.6) are conservation of momentum.

Another neat trick is to break up pressure into two components. Pressure can be expressed as $\hat{p} = \hat{p}_d + \hat{p}_h$ where $\hat{p}_h$ is the hydrostatic pressure. Since, hydrostatic pressure is usually the dominate term, solving just for $\hat{p}_d$ allows for a scaling that produces unknowns (u_1, u_2, s_{11}, s_{11}, $\hat{p}_d$) that are approximately $O(1)$. This scaling can be achieved by setting $f_2 = \max(u_1)^{-1/3} f_2$, where u_1 is the physical solution in m s^{-1}. Then the new forcing function needs to be $\underline{f} = [f_1, f_2]^T - \nabla \hat{p}_h$.

One of the other goals of this thesis is to create a formulation that can be quickly and efficiently solved. In this case, that solver is AMG. To make the fluidity formulation more amenable to AMG, the system (5.4.2)-(5.4.6) is augmented with an equation that represents the curl of the velocity gradient. Unfortunately, the velocity gradient is obscured by the creation of s_{11} and s_{12}. To recover the velocity gradient, a definition that involves the vorticity is added. To follow the same form as the other definitions, (5.4.2)-(5.4.3), this vorticity-based equation is

$$\psi\omega = (-\partial_z u_1 + \partial_x u_2). \tag{5.4.7}$$

The definition of ψ is discussed later. Now, gradient of $\underline{u}$ is reconstructed using (5.4.2)-(5.4.4) and (5.4.7),

$$\nabla \underline{u} = \begin{bmatrix} \partial_x u_1 & \partial_z u_1 \\ \partial_x u_2 & \partial_z u_2 \end{bmatrix} = \frac{1}{2} \begin{bmatrix} \phi s_{11} & \phi s_{12} - \psi\omega \\ \phi s_{12} + \psi\omega & -\phi s_{11} \end{bmatrix}. \tag{5.4.8}$$

Finally, $\nabla \times \nabla u = 0$ is added to the fluidity formulation resulting in the

deviatoric-stress/vorticity/pressure/velocity form,

$$\phi s_{11} - (\partial_x u_1 - \partial_z u_2) = 0, \tag{5.4.9}$$

$$\phi s_{12} - (\partial_z u_1 + \partial_x u_2) = 0, \tag{5.4.10}$$

$$\psi\omega - (-\partial_z u_1 + \partial_x u_2) = 0, \tag{5.4.11}$$

$$\partial_x u_1 + \partial_z u_2 = 0, \tag{5.4.12}$$

$$-\partial_x s_{11} - \partial_z s_{12} + \partial_x \hat{p} - f_1 = 0, \tag{5.4.13}$$

$$\partial_z s_{11} - \partial_x s_{12} + \partial_z \hat{p} - f_2 = 0, \tag{5.4.14}$$

$$-\partial_z(\phi s_{11}) + \partial_x(\phi s_{12}) - \partial_x(\psi\omega) = 0, \tag{5.4.15}$$

$$-\partial_x(\phi s_{11}) - \partial_z(\phi s_{12}) - \partial_z(\psi\omega) = 0. \tag{5.4.16}$$

This is known as the **augmented fluidity formulation**. Notice that the two new equations are consistent with the fluidity formulation such that, if a solution satisfies (5.4.2)-(5.4.4), then it must also satisfy (5.4.15)-(5.4.16). Furthermore, that solution must also satisfy (2.3.9)-(2.3.10).

It is important to note that for better AMG performance, the curl equations, (5.4.15)-(5.4.16), and the div equations, (5.4.13)-(5.4.14), need to be balanced in terms of magnitude. In places where ϕ goes to zero, the curl equations are deemphasized and the balance with the div equations is disrupted. To maintain this balance, the curl equations may need to be scaled by a function that emphasizes the locations where ϕ is small.

The last modification is to use the product rule on the terms in the curl equations. Expanding

the 6 terms from equations (5.4.15) and (5.4.16) using the product rule yields:

$$\begin{aligned}
\partial_x(\phi s_{11}) &= \frac{1}{2}\partial_x\left({s_{11}}^3 + {s_{12}}^2 s_{11}\right) \\
&= \frac{1}{2}\left(3{s_{11}}^2\partial_x(s_{11}) + {s_{12}}^2\partial_x(s_{11}) + 2s_{12}s_{11}\partial_x(s_{12})\right), \\
\partial_x(\phi s_{12}) &= \frac{1}{2}\partial_x\left({s_{11}}^2 s_{12} + {s_{12}}^3\right) \\
&= \frac{1}{2}\left(2s_{11}s_{12}\partial_x(s_{11}) + {s_{11}}^2\partial_x(s_{12}) + 3{s_{12}}^2\partial_x(s_{12})\right), \\
\partial_x(\psi\omega) &= \frac{1}{2}\partial_x\left({s_{11}}^2\omega + {s_{12}}^2\omega + \omega^3\right) \\
&= \frac{1}{2}\left(s_{11}\omega\partial_x(s_{11}) + {s_{11}}^2\partial_x(\omega) + s_{12}\omega\partial_x(s_{12}) + {s_{12}}^2\partial_x(\omega) + 3\omega^2\partial_x(\omega)\right), \\
\partial_z(\phi s_{11}) &= \frac{1}{2}\partial_z\left({s_{11}}^3 + {s_{12}}^2 s_{11}\right) \\
&= \frac{1}{2}\left(3{s_{11}}^2\partial_z(s_{11}) + {s_{12}}^2\partial_z(s_{11}) + 2s_{12}s_{11}\partial_z(s_{12})\right), \\
\partial_z(\phi s_{12}) &= \frac{1}{2}\partial_z\left({s_{11}}^2 s_{12} + {s_{12}}^3\right) \\
&= \frac{1}{2}\left(2s_{11}s_{12}\partial_z(s_{11}) + {s_{11}}^2\partial_z(s_{12}) + 3{s_{12}}^2\partial_z(s_{12})\right), \\
\partial_z(\psi\omega) &= \frac{1}{2}\partial_z\left({s_{11}}^2\omega + {s_{12}}^2\omega + \omega^3\right) \\
&= \frac{1}{2}\left(s_{11}\omega\partial_z(s_{11}) + {s_{11}}^2\partial_z(\omega) + s_{12}\omega\partial_z(s_{12}) + {s_{12}}^2\partial_z(\omega) + 3\omega^2\partial_z(\omega)\right).
\end{aligned} \tag{5.4.17}$$

Plugging in the expanded forms from (5.4.17) into (5.4.15) and (5.4.16) and sorting based on the derivative terms yields:

$$\psi^{-1}\left(A\begin{bmatrix}\partial_x s_{11}\\ \partial_z s_{11}\end{bmatrix} + B\begin{bmatrix}\partial_x s_{12}\\ \partial_z s_{12}\end{bmatrix} + C\begin{bmatrix}\partial_x\omega\\ \partial_z\omega\end{bmatrix}\right) = 0, \tag{5.4.18}$$

where $A = \begin{bmatrix}a_{11} & a_{12}\\ a_{12} & a_{22}\end{bmatrix}$, $B = \begin{bmatrix}b_{11} & b_{12}\\ b_{12} & b_{22}\end{bmatrix}$, $C = \begin{bmatrix}c_{11} & 0\\ 0 & c_{11}\end{bmatrix}$ are matrices containing the curl coefficient

equations and are defined as:

$$\begin{aligned}
a_{11} &= \ \ 1/2\left(2s_{11}s_{12} - s_{11}\omega\right), \\
a_{12} &= -1/2\left(3{s_{11}}^2 + {s_{12}}^2\right), \\
a_{22} &= -1/2\left(2s_{11}s_{12} + s_{11}\omega\right), \\
b_{11} &= \ \ 1/2\left({s_{11}}^2 + 3{s_{12}}^2 - s_{12}\omega\right), \\
b_{12} &= -1/2\left(2s_{11}s_{12}\right), \\
b_{22} &= -1/2\left({s_{11}}^2 + 3{s_{12}}^2 + s_{12}\omega\right), \\
c_{11} &= -1/2\left({s_{11}}^2 + {s_{12}}^2 + 3\omega^2\right).
\end{aligned} \tag{5.4.19}$$

Another, possibly cleaner, way to look at this system is in tableau form,

$$\left[\begin{array}{ccc|c|cc}
\phi & 0 & 0 & 0 & -\partial_x & \partial_z \\
0 & \phi & 0 & 0 & -\partial_z & -\partial_x \\
0 & 0 & \psi & 0 & \partial_z & -\partial_x \\
0 & 0 & 0 & 0 & \partial_x & \partial_z \\
\hline
-\partial_x & -\partial_z & 0 & \partial_x & 0 & 0 \\
\partial_z & -\partial_x & 0 & \partial_z & 0 & 0 \\
\hline
\frac{a_{11}}{\varphi}\partial_x + \frac{a_{12}}{\varphi}\partial_z & \frac{b_{11}}{\varphi}\partial_x + \frac{b_{12}}{\varphi}\partial_z & \frac{c_{11}}{\varphi}\partial_x & 0 & 0 & 0 \\
\frac{a_{12}}{\varphi}\partial_x + \frac{a_{22}}{\varphi}\partial_z & \frac{b_{12}}{\varphi}\partial_x + \frac{b_{22}}{\varphi}\partial_z & \frac{c_{11}}{\varphi}\partial_z & 0 & 0 & 0
\end{array}\right]
\left[\begin{array}{c} s_{11} \\ s_{12} \\ \omega \\ \hline \hat{p} \\ \hline u_1 \\ u_2 \end{array}\right]
=
\left[\begin{array}{c} 0 \\ 0 \\ 0 \\ 0 \\ \hline f_1 \\ f_2 \\ \hline 0 \\ 0 \end{array}\right], \tag{5.4.20}$$

where φ is the scaling designed to balance the curl and div equations.

From (5.4.19) it is clear that the coefficients are quadratic functions of the dependent variables, s_{11}, s_{12}, ω. Further, it can be established that, when scaled by $\varphi = \psi$, the coefficients stay bounded. Take, for example, the function

$$\frac{a_{11}}{\psi} = \frac{2s_{11}s_{12} - s_{11}\omega}{{s_{11}}^2 + {s_{12}}^2 + \omega^2} \tag{5.4.21}$$

Taking the partial derivatives with respect to s_{11}, s_{12}, and ω of (5.4.21) yields:

$$\begin{aligned}
\frac{\partial}{\partial s_{11}}\left(\frac{a_{11}}{\psi}\right) &= \ \ \frac{(2s_{12} - \omega)(-{s_{11}}^2 + {s_{12}}^2 + \omega^2)}{({s_{11}}^2 + {s_{12}}^2 + \omega^2)^2} \\
\frac{\partial}{\partial s_{12}}\left(\frac{a_{11}}{\psi}\right) &= \ \ \frac{2s_{11}({s_{11}}^2 - {s_{12}}^2 + s_{12}\omega + \omega^2)}{({s_{11}}^2 + {s_{12}}^2 + \omega^2)^2} \\
\frac{\partial}{\partial \omega}\left(\frac{a_{11}}{\psi}\right) &= -\frac{s_{11}({s_{11}}^2 + {s_{12}}^2 + 4s_{12}\omega - \omega^2)}{({s_{11}}^2 + {s_{12}}^2 + \omega^2)^2}
\end{aligned} \tag{5.4.22}$$

Setting all of these derivatives for zero and solving for s_{11}, s_{12}, and ω results in three critical points: $(s_{11} = 0, \omega = 2s_{12})$, $(s_{11} = -\sqrt{5}s_{12}/2, \omega = -s_{12}/2)$, and $(s_{11} = \sqrt{5}s_{12}/2, \omega = -s_{12}/2)$. Plugging these into (5.4.21) results into the values of 0, $-\sqrt{5}/2$, and $\sqrt{5}/2$ respectively.

Next, consider what happens when $s_{11} \to \pm\infty$, $s_{12} \to \pm\infty$, and/or $\omega \to \pm\infty$. Notice that the degree of the relevant variable(s) is always less than or equal to the degree in the denominator. When the degree is less than, the limit will be 0. When the degrees are equal, the limit will be the coefficient or sum of coefficients associated with the relevant variable(s). In the case of (5.4.21), all three of these limits are zero. Table 5.1 summarizes the critical points, limits, and ranges of the curl coefficient functions.

Table 5.1: This table shows the ranges of the various coefficients from equations (5.4.19) when they are divided by ψ. The critical values are the values of the relevant coefficient evaluated at the critical points. The max/min limit comes from examining the coefficient equation and determine the extrema of the various limits where a variable goes to infinity

Coefficient	Critical Values			Min, Max Limit	Range
a_{11}	$0,$	$-\frac{\sqrt{5}}{2},$	$\frac{\sqrt{5}}{2}$	$-3, \quad 3$	$(-3, \quad 3)$
a_{12}	$0,$	$-1,$	-3	$-4, -1$	$(-4, \quad 0]$
a_{22}	$0,$	$\frac{\sqrt{5}}{2},$	$-\frac{\sqrt{5}}{2}$	$-3, \quad 3$	$(-3, \quad 3)$
b_{11}	$1,$	$\frac{3}{2}+\sqrt{\frac{5}{2}},$	$\frac{3}{2}-\sqrt{\frac{5}{2}}$	$-1, \quad 5$	$(-1, \quad 5)$
b_{12}	$0,$	$1,$	-1	$-2, \quad 2$	$(-2, \quad 2)$
b_{22}	$-1,$	$-\frac{3}{2}+\sqrt{\frac{5}{2}},$	$-\frac{3}{2}-\sqrt{\frac{5}{2}}$	$-5, \quad 1$	$(-5, \quad 1)$
c_{11}	$-1,$	-3		$-5, -1$	$(-5, -1]$

The augmented fluidity formulation was used in [5], with $\psi = \frac{1}{2}({s_{11}}^2 + {s_{12}}^2 + \omega^2)$ and the curl equations were scaled by ψ^{-1}. This resulted in a system that produced accurate solutions and AMG performed very well on a simple domain. However, this scaling caused reduced finite-element convergence when the domain was more complected as in ISMIP benchmark B. Experimenting with various scalings led to the discovery that the basic fluidity formulation exhibits optimal finite-element convergence for the domain in benchmark B. However, AMG did not perform well on the basic fluidity formulation since it was not H^1 elliptic. Despite the performance issues, both the basic and augmented fluidity formulations produced solutions that were accurate when compared

with ISMIP's database of solutions and the Taylor-Hood method from [30]. This work is discussed in Chapters 7-8.

This leads to a few questions that need to be answered. Which FOSLS formulation performs better? How should ψ be defined? How should the curl equations be scaled? the numerical results from Chapters 8-9 are used to examine these questions, but first, they are discussed below to present possible answers.

The first question is easy to address since there are only two possible formulations, basic and augmented. The basic system avoids the difficulties introduced by the curl equation such as additional nonlinearity and choosing a scaling. The major problem with this system, is that there is not a readily available iterative linear solver for a system of this form. Right now, it is solved using a direct solver, which is not a useful choice when solving significantly larger problems. On the other hand, The advantage to the augmented system, with proper scaling, is that it is amenable to an AMG solver, which is a fast and efficient iterative solver.

The next question involves the definition of ψ. One possible definition is $\psi = \frac{1}{2}({s_{11}}^2 + {s_{12}}^2 + \omega^2)$, which follows the format of ϕ and leads to a scaling that results in the various terms of the curl equations to remain bounded in places where $\phi \to 0$. The problem is it can lead to cube root type behavior in ω. Looking at (5.4.7),

$$\begin{aligned} \psi\omega &= (-\partial_z u_1 + \partial_x u_2), \\ \frac{1}{2}({s_{11}}^2\omega + {s_{12}}^2\omega + \omega^3) &= (-\partial_z u_1 + \partial_x u_2). \end{aligned}$$

Solving for ω yields the only real root of:

$$\omega = \frac{\sqrt[3]{R}}{3\sqrt[3]{2}} - \frac{\sqrt[3]{2}\left({s_{11}}^2 + {s_{12}}^2\right)}{R},$$

where

$$R = \sqrt{(54\partial_x u_2 - 54\partial_z u_1)^2 + 108\left({s_{11}}^2 + {s_{12}}^2\right)^3} - 54\partial_z u_1 + 54\partial_x u_2.$$

Therefore, ω will have cube root type behavior unless R is exactly a cubic, which is unlikely.

An alternative definition for ψ is simply $\psi = 1$. This avoids unnecessarily adding cube root behavior to ω. The downside to this definition is that, when the curl equation is scaled, the ω term of the curl equation will potentially be left out of balance with the other terms.

The last question is how to scale the curl equations, (5.4.15)-(5.4.16)? The work in [5] led to the discovery that strengthening the curl equations results in reduced finite-element convergence. However, AMG performed better on the strongly scaled systems. It seemed that there could be a balance between finite-element convergence and AMG performance.

Here are several scalings tested in hopes of finding this balance. As mentioned above, when using an appropriate definition for ψ, the scaling $\psi^{-1/2}$ keeps the curl equations nicely bounded. The reason for using this scaling is to keep the curl and div (momentum) equations balanced when $\phi \to 0$ leading to improved AMG performance. A possible problem with this scaling is that it may not compensate well enough for when $\phi \to 0$, since $\psi \not\to 0$ in the same places as ϕ because $\omega \not\to 0$ in these places.

The next logical scaling is $\phi^{-1/2}$. This will definitely emphasize the places where $\phi \to 0$. However, it also has the obvious problem of being unbounded in these same places. This can be resolved by instead scaling by $(\phi + c)^{-1/2}$, where c is a small constant dependent on the size of the mesh. Additionally, this might scale the curl equations too strongly. As discussed in Chapters 8-9, the augmented fluidity formulation experiences reduced finite-element convergence when strongly scaled.

To get around the reduced finite-element convergence problem, a scaling of ϕ will intentionally unweight the areas where $\phi \to 0$. Unfortunately, this can lead to poorer solution accuracy near these regions. Also, since this will lead to a drastic unbalance between the curl and div equations, AMG performance will suffer. This scaling closely resembles the basic fluidity formulation.

Finally, the curl equation can be left unweighted altogether. This will just be useful as a baseline for comparing the other scalings and will have poorer AMG performance.

It should be noted that since the approximate solutions are obtained by using a least squares method, scaling an equation in the system by φ results in the corresponding term in the functional

to be scaled by φ^2. The four scalings mentioned above act like scaling the curl portion of the functional by ψ^{-1}, ϕ^{-1}, ϕ^2, or 1.

Chapter 6

Well Posedness

This chapter will discuss the linearizations of the FOSLS formulations. Additionally, the continuity and coercivity of the augmented fluidity formulation will be discussed.

6.1 Linearization

In this section, linearization of both the fluidity and viscosity forms is developed and continuity of the linearized forms is addressed. Coercivity is discussed in the following section. Consider the general functional,

$$\mathcal{F}(\mathcal{U}, \mathbf{F}) = ||\mathcal{L}(\mathcal{U}) - \mathbf{F}||^2,$$

where

$$\mathcal{L}(\mathcal{U}) = L\mathcal{U} + \mathcal{N}(\mathcal{U}),$$

$L\mathcal{U}$ is the linear part and $\mathcal{N}(\mathcal{U})$ contains the nonlinear terms. Linearization is accomplished by expanding $\mathcal{L}(\mathcal{U})$ about a current approximation, which is denote by $\mathcal{U}_0$. This yields

$$\mathcal{L}(\mathcal{U}_0 + \delta\mathcal{U}) = \mathcal{L}(\mathcal{U}_0) + \mathcal{L}'(\mathcal{U}_0)[\delta\mathcal{U}] + \frac{1}{2}\mathcal{L}''(\hat{\mathcal{U}})[\delta\mathcal{U}, \delta\mathcal{U}]$$

where $\mathcal{L}'$ and $\mathcal{L}''$ are the first and second Frechet derivatives of $\mathcal{L}$ centered at $\mathcal{U}_0$ and $\hat{\mathcal{U}} = (1 - \alpha)\mathcal{U}_0 + \alpha\delta\mathcal{U}$ for some $\alpha \in [0, 1]$. Note that

$$\mathcal{L}'(\mathcal{U}_0)[\mathcal{V}] = L\mathcal{V} + \mathcal{N}'(\mathcal{U}_0)[\mathcal{V}].$$

6.1.1 Fluidity Formulations

The linearization of the augmented fluidity form is considered first, which will lead directly to the linearization of the basic fluidity form by simply removing a few equations. To derive $\mathcal{L}'_F(\mathcal{U}_{0F})[\delta\mathcal{U}_F]$, where $\mathcal{U}_F = (\underline{u}, \underline{s}, \omega, p)$, the nonlinear terms in (5.4.20) are examined separately. Let

$$\underline{s} = \begin{bmatrix} s_{11} \\ s_{12} \end{bmatrix} \text{ and } E = \begin{bmatrix} -\partial_x & \partial_z \\ -\partial_z & -\partial_x \end{bmatrix}.$$

Then, equations (5.4.9) - (5.4.10) can be written as

$$\phi\underline{s} + E\underline{u} = 0, \tag{6.1.1}$$

and the first nonlinear term is $\phi\underline{s}$. To linearize this term, let $R(\underline{s}) = \phi[\underline{s}]\underline{s}$ and $\phi[\underline{s}_0] = \phi_0$. Then,

$$\begin{aligned} \frac{\partial}{\partial\theta} R(\underline{s}_0 + \theta\delta\underline{s})\Big|_{\theta=0} &= \frac{\partial}{\partial\theta} \left(\phi[\underline{s}_0 + \theta\delta\underline{s}]\,(\underline{s}_0 + \theta\delta\underline{s})\right)\Big|_{\theta=0} \\ &= \phi'[\underline{s}_0 + \theta\delta\underline{s}]\,(\underline{s}_0 + \theta\delta\underline{s}) + \phi[\underline{s}_0 + \theta\delta\underline{s}]\delta\underline{s}\big|_{\theta=0} \\ &= \phi'[\underline{s}_0 + \theta\delta\underline{s}]\big|_{\theta=0}\,\underline{s}_0 + \phi_0\theta\delta\underline{s}. \end{aligned}$$

Now, calculate ϕ' (Note that $\phi = \frac{1}{2}\langle\underline{s},\ \underline{s}\rangle$):

$$\begin{aligned} \phi'[\underline{s}_0 + \theta\delta\underline{s}]\big|_{\theta=0} &= \frac{\partial}{\partial\theta}\left[\frac{1}{2}\,\langle\underline{s}_0 + \theta\delta\underline{s}, \underline{s}_0 + \theta\delta\underline{s}\rangle\right]\Big|_{\theta=0} \\ &= \langle\underline{s}_0, \delta\underline{s}\rangle = \phi'(\underline{s}_0)[\delta\underline{s}]. \end{aligned}$$

Thus,

$$\frac{\partial}{\partial\theta} R(\underline{s}_0 + \theta\delta\underline{s})\Big|_{\theta=0} = \langle\underline{s}_0,\ \delta\underline{s}\rangle\,\underline{s}_0 + \phi_0\delta\underline{s}.$$

This can be rewritten as

$$\langle\underline{s}_0,\ \delta\underline{s}\rangle\,\underline{s}_0 + \phi_0\delta\underline{s} = (\phi_0 I + \underline{s}_0\,\underline{s}_0{}^T)\delta\underline{s}.$$

Therefore, the linearized form of the nonlinearity in Equation (6.1.1) is:

$$\begin{aligned} (\phi s)' &= \phi_0\underline{s}_0 + \phi'\underline{s}_0 + \phi_0\delta\underline{s} \\ &= \phi_0\underline{s}_0 + (\phi_0 I + \underline{s}_0\,\underline{s}_0{}^T)\delta\underline{s}. \end{aligned} \tag{6.1.2}$$

Using the same method, the nonlinear term in equation (5.4.11), $\psi\omega$, becomes:

$$(\psi\omega)' = \psi_0\omega_0 + \psi'\omega_0 + \psi_0\delta\omega,$$

which can also be rewritten as:

$$(\psi\omega)' = \psi_0\omega_0 + (\psi_0 e_3^T + \omega_0\, \underline{\hat{s}}_0{}^T)\delta\underline{\hat{s}}, \tag{6.1.3}$$

with $e_3 = [0,\, 0,\, 1]^T$ and $\underline{\hat{s}} = [s_{11},\, s_{12},\, \omega]^T$. Finally, to linearize the last two equations in (5.4.20), define $M = [A|B|C]$ as a 2×6 matrix containing the curl coefficient functions and

$$\underline{\underline{\nabla}} = \begin{bmatrix} \nabla & 0 & 0 \\ 0 & \nabla & 0 \\ 0 & 0 & \nabla \end{bmatrix}$$

as a 6×3 matrix containing column gradient operators. Then, the curl equations (5.4.18) can be written simply as:

$$M\underline{\underline{\nabla}}\,\underline{\hat{s}} = 0.$$

Using the same linearization method,

$$\left(M\underline{\underline{\nabla}}\,\underline{\hat{s}}\right)' = M_0\underline{\underline{\nabla}}\,\underline{\hat{s}}_0 + M_0\underline{\underline{\nabla}}\delta\underline{\hat{s}} + M'(\underline{\hat{s}}_0)[\delta\underline{\hat{s}}]\underline{\underline{\nabla}}\,\underline{\hat{s}}_0.$$

As stated above, the elements of M are quadratics in the dependent variables. Linearization of each element of M is tedious and is left out. The curl equation is scaled by ${\varphi_0}^{-1}$, as discussed in Section 5.4, which is simply lagged using the previous Newton step's solution. To avoid yet another singularity, a small constant, c, can be added to this scaling, $\frac{1}{\varphi_0+c}$. This yields linear elements of M' divided by a function that is bounded away from zero. Thus, $\frac{1}{\varphi_0+c}M'(\underline{\hat{s}}_0)[\delta\underline{\hat{s}}]\underline{\underline{\nabla}}\,\underline{\hat{s}}_0$ is a bounded linear operator on $\delta\underline{\hat{s}}$ that yields a 2×6 matrix of functions. However, in practice, when $\varphi = \psi^{1/2}$ the small constant has not been needed and is omitted from the rest of the analysis. This is because ψ tends to be greater than 0 as shown in Section 8.2. One heuristic for why $\psi > 0$ involves the fact that the only time $\phi = 0$ is when the ice sheet is experiencing solid-body rotations/translations as seen in Equation (5.3.6). The translation are removed from the system by having a velocity based

Dirichlet boundary condition. For rotation, Equation (5.3.7) shows that $s_{11}, s_{12} = 0$. Next, from Equation (5.4.7),

$$\begin{aligned}
\psi\omega &= (-\partial_z u_1 + \partial_x u_2), \\
\psi\omega &= -2c_1, \\
\frac{1}{2}\left({s_{11}}^2\omega + {s_{12}}^2\omega + \omega^3\right) &= -2c_1, \\
\frac{1}{2}\omega^3 &= -2c_1, \\
\omega &= (-4c_1)^{\frac{1}{3}}.
\end{aligned}$$

Therefore, $\omega \neq 0$, which implies that $\psi \neq 0$.

The full linearized system is:

$$\phi' \underline{s}_0 + \phi_0 \delta\underline{s} + E\delta\underline{u} = -\phi_0 \underline{s}_0, \tag{6.1.4}$$

$$\psi'\omega_0 + \psi_0\delta\omega - \nabla \times \delta\underline{u} = -\psi_0\omega_0, \tag{6.1.5}$$

$$\nabla \cdot \delta\underline{u} = -\nabla \cdot \underline{u}_0, \tag{6.1.6}$$

$$-\nabla \cdot \delta\underline{\underline{s}} + \nabla\delta\hat{p} = \underline{f} - \left(-\nabla \cdot \underline{\underline{s}}_0 + \nabla\delta\hat{p}_0\right), \tag{6.1.7}$$

$$\frac{1}{\psi_0} M_0 \underline{\underline{\nabla}}\delta\hat{\underline{s}} + \frac{1}{\psi_0} M'(\hat{\underline{s}}_0)[\delta\hat{\underline{s}}]\underline{\underline{\nabla}}\,\hat{\underline{s}}_0 = -\frac{1}{\psi_0} M_0 \underline{\underline{\nabla}}\,\hat{\underline{s}}_0. \tag{6.1.8}$$

If Equations (6.1.5) and (6.1.8) are removed from the system above, then the result is the linearized form of the basic fluidity formulation.

Later in the continuity proof, it will be useful to have bounds on the nonlinear portion of these equations. For equation (6.1.4), consider the form found in equation (6.1.2). The only eigenvalue of the rank one operator $\underline{s}_0\,{\underline{s}_0}^T$ is $2\phi_0$ since $2\phi_0 = {\underline{s}_0}^T\underline{s}_0$ and

$$\underline{s}_0\,{\underline{s}_0}^T\underline{s}_0 = 2\phi_0\underline{s}_0.$$

This implies that $|\underline{s}_0\,{\underline{s}_0}^T| \leq 2\phi_0 I$ point wise and more importantly,

$$(|\phi_0 + \underline{s}_0\,{\underline{s}_0}^T|)|\delta\underline{s}| \leq 3\phi_0|\delta\underline{s}|. \tag{6.1.9}$$

This is a local bound and can be turned into a global bound by assuming $||\phi_0||_\infty$ is bounded. The next step is to establish bounds for equation (6.1.5) and equation (6.1.8). Expanding the terms in

these equations component wise would reveal that they is just a series of products of the terms in $\nabla\underline{\hat{s}}_0$, $\underline{\hat{s}}_0$, $\nabla\delta\underline{\hat{s}}$, and $\delta\underline{\hat{s}}$ in various combinations. With the aid of a significant quantity of algebra, it can be shown that,

$$||\psi'\omega_0 + \psi_0\delta\omega|| \leq C_1||\delta\underline{\hat{s}}||_1, \tag{6.1.10}$$

and

$$\left\| \frac{1}{\varphi_0} M_0 \underline{\underline{\nabla}}\delta\underline{\hat{s}} + \frac{1}{\varphi_0} M'(\underline{\hat{s}}_0)\underline{\underline{\nabla}}\,\underline{\hat{s}}_0 \right\| \leq C_2||\delta\underline{\hat{s}}||_1, \tag{6.1.11}$$

where $C_1,\ C_2$ are functions of $||\underline{\hat{s}}_0||_\infty$ and $||\nabla\underline{\hat{s}}_0||_\infty$. This assumes that φ^{-1} is chosen to be $\psi^{-1/2}$, $\phi^{-1/2}$, ϕ, or 1.

6.1.2 Viscosity Formulation

Linearization of the the FOSLS viscosity form is developed in a similar fashion. To produce $\mathcal{L}'_V(\mathcal{U}_{0V})[\delta\mathcal{U}_V]$, where $\mathcal{U}_V = \left(\underline{u}, \underline{\underline{U}}, p\right)$, the only nonlinear term in this formulation is in (5.2.3),

$$\hat{\mu}\left(\underline{\underline{U}} + \underline{\underline{U}}^T\right).$$

To simplify this use the definition of strain rate (2.3.5) to get

$$2\hat{\mu}\underline{\underline{\dot{\varepsilon}}}.$$

Using the same method used to find (6.1.2),

$$(2\hat{\mu}\underline{\underline{\dot{\varepsilon}}})' = 2\left(\mu_0\underline{\underline{\dot{\varepsilon}}}_0 + \mu'\underline{\underline{\dot{\varepsilon}}}_0 + \mu_0\delta\underline{\underline{\dot{\varepsilon}}}\right),$$

which can be written as,

$$(2\hat{\mu}\underline{\underline{\dot{\varepsilon}}})' = 2\left(\mu_0\underline{\underline{\dot{\varepsilon}}}_0 - \frac{2}{3}\langle\underline{\underline{\dot{\varepsilon}}}_0 : \underline{\underline{\dot{\varepsilon}}}_0\rangle^{-4/3}\langle\underline{\underline{\dot{\varepsilon}}}_0 : \delta\underline{\underline{\dot{\varepsilon}}}\rangle\underline{\underline{\dot{\varepsilon}}}_0 + \mu_0\delta\underline{\underline{\dot{\varepsilon}}}\right).$$

Treating $\underline{\underline{\dot{\varepsilon}}}$ as a column vector yields:

$$(2\hat{\mu}\underline{\dot{\varepsilon}})' = 2\mu_0\underline{\dot{\varepsilon}}_0 + 2\left(\mu_0 I - \frac{2}{3}\hat{\mu}_0^{-4}\underline{\dot{\varepsilon}}_0\underline{\dot{\varepsilon}}_0{}^T\right)\delta\underline{\dot{\varepsilon}}. \tag{6.1.12}$$

Therefore, the linearization of the velocity-gradient viscosity formulation is:

$$\delta\underline{\underline{U}} - \nabla\delta\underline{u} = -\underline{\underline{U}}_0 + \nabla\underline{u}_0, \tag{6.1.13}$$

$$\nabla\cdot\delta\underline{u} = -\nabla\cdot\underline{u}_0, \tag{6.1.14}$$

$$\nabla\cdot 2\left(\mu'\dot{\underline{\underline{\varepsilon}}}_0 + \mu_0\delta\dot{\underline{\underline{\varepsilon}}}\right) + \nabla\delta\hat{p} = \underline{f} - \left(\nabla\cdot 2\hat{\mu}_0\dot{\underline{\underline{\varepsilon}}}_0 - \nabla\hat{p}_0\right), \tag{6.1.15}$$

$$\nabla\times\delta\underline{\underline{U}} = -\nabla\times\underline{\underline{U}}_0. \tag{6.1.16}$$

As with the stress-vorticity fluidity formulation, it will useful to bound the nonlinear portion of the viscosity fluidity. The only nonlinear term is (5.2.3), the momentum equation. Using the definition of strain rate (2.3.5), the nonlinearlity can be written

$$2\nabla\cdot\hat{\mu}\dot{\underline{\underline{\varepsilon}}}. \tag{6.1.17}$$

Recall that $\hat{\mu}$ is defined in (2.3.11), where it is shown to be a function of $\dot{\underline{\underline{\varepsilon}}}$,

$$\hat{\mu}(\dot{\underline{\underline{\varepsilon}}}) = \left\langle\dot{\underline{\underline{\varepsilon}}},\dot{\underline{\underline{\varepsilon}}}\right\rangle^{-1/3}.$$

This yields

$$\nabla\hat{\mu} = -\frac{1}{3}\left\langle\dot{\underline{\underline{\varepsilon}}},\dot{\underline{\underline{\varepsilon}}}\right\rangle^{-4/3}\nabla\left\langle\dot{\underline{\underline{\varepsilon}}},\dot{\underline{\underline{\varepsilon}}}\right\rangle.$$

Using the product rule, (6.1.17) can be written

$$2\hat{\mu}\nabla\cdot\left(\dot{\underline{\underline{\varepsilon}}}\right) + 2\nabla\hat{\mu}\cdot\dot{\underline{\underline{\varepsilon}}}.$$

Putting this together yields

$$\|2\nabla\cdot\hat{\mu}\dot{\underline{\underline{\varepsilon}}}\| \le C_4\|\dot{\underline{\underline{\varepsilon}}}\|_\infty^{-2/3}\|\nabla\dot{\underline{\underline{\varepsilon}}}\| \le C_5\|\dot{\underline{\underline{\varepsilon}}}\|_\infty^{-2/3}\|\nabla\underline{\underline{U}}\|, \tag{6.1.18}$$

where C_4, C_5 are functions of $||\underline{u}_0||_\infty$ and $||\nabla\underline{u}_0||_\infty$.

6.2 Continuity

In this section a continuity bound is derived for the linearized systems above. The important issue is to bound

$$||\mathcal{L}'(\mathcal{U}_0)[\delta\mathcal{U}]|| \le \mathcal{C}||\delta\mathcal{U}||_1,$$

where $\mathcal{C}$ involves $||\mathcal{U}_0||_\infty$ and $||\nabla\mathcal{U}_0||_\infty$, $||\cdot||$ is the L^2 norm and $||\cdot||_1$ is the H^1 norm. First, use the triangle inequality to get

$$||\mathcal{L}'(\mathcal{U}_0)[\delta\mathcal{U}]|| \leq ||L\delta\mathcal{U}|| + ||\mathcal{N}'(\mathcal{U}_0)[\delta\mathcal{U}]||. \tag{6.2.1}$$

6.2.1 Fluidity Formulations

The first term in (6.2.1) is just the collection of all the linear terms so,

$$\begin{aligned}
||L_F\delta\mathcal{U}_F||^2 &= ||E\delta\underline{u}||^2 + ||\nabla\times\delta\underline{u}||^2 + ||\nabla\cdot\delta\underline{u}||^2 + \left|\left|-\nabla\cdot\delta\underline{\underline{s}} + \nabla\delta\hat{p}\right|\right|^2 \\
&\leq ||E\delta\underline{u}||^2 + ||\nabla\times\delta\underline{u}||^2 + ||\nabla\cdot\delta\underline{u}||^2 + \left|\left|\nabla\cdot\delta\underline{\underline{s}}\right|\right|^2 + ||\nabla\delta\hat{p}||^2 \\
&\leq ||E\delta\underline{u}||^2 + ||\nabla\times\delta\underline{u}||^2 + ||\nabla\cdot\delta\underline{u}||^2 + 2||\delta\underline{u}||^2 \\
&+ \left|\left|\nabla\cdot\delta\underline{\underline{s}}\right|\right|^2 + \left|\left|\nabla\times\delta\underline{\underline{s}}\right|\right|^2 + 2||\delta\underline{\underline{s}}||^2 \\
&+ ||\nabla\delta\hat{p}||^2 + ||\delta\hat{p}||^2 \\
&\leq 2||\delta\underline{u}||_1^2 + 2||\delta\underline{\underline{s}}||_1^2 + ||\delta\hat{p}||_1^2 = 2||\delta\mathcal{U}_F||_1^2.
\end{aligned}$$

Therefore,

$$||L_F\delta\mathcal{U}_F|| \leq \sqrt{2}||\delta\mathcal{U}_F||_1 \tag{6.2.2}$$

Now a bound is found for the nonlinear terms.

$$\begin{aligned}
||\mathcal{N}_F'(\mathcal{U}_{0F})\delta\mathcal{U}_F||^2 &= ||\phi'\underline{\sigma}_0' + \phi_0\delta\underline{\sigma}'||^2 + ||\psi'\omega_0 + \psi_0\delta\omega||^2 + \left\|\frac{1}{\psi_0}M_0\underline{\underline{\nabla}}\delta\hat{\underline{s}} + \frac{1}{\psi_0}M'(\hat{\underline{s}}_0)\underline{\underline{\nabla}}\,\hat{\underline{s}}_0\right\|^2 \\
&\leq ||(\phi_0 I + \underline{\sigma}_0'\,\underline{\sigma}_0'^{\,T})\delta\underline{\sigma}'||^2 + ||\psi'\omega_0 + \psi_0\delta\omega||^2 + \left\|\frac{1}{\psi_0}M_0\underline{\underline{\nabla}}\delta\hat{\underline{s}} + \frac{1}{\psi_0}M'(\hat{\underline{s}}_0)\underline{\underline{\nabla}}\,\hat{\underline{s}}_0\right\|^2
\end{aligned}$$

Using the bounds established in (6.1.9), (6.1.10), (6.1.11),

$$\begin{aligned}
&\leq 9\phi_0||\delta\underline{\sigma}'||^2 + {C_1}^2||\delta\hat{\underline{\sigma}}'||^2 + {C_2}^2||\delta\hat{\underline{\sigma}}'||_1^2 \\
&\leq C_3||\delta\hat{\underline{\sigma}}'||_1^2.
\end{aligned} \tag{6.2.3}$$

where $C_3 = 3\text{Max}(9, {C_1}^2, {C_2}^2)$. Consider the linearized functional:

$$\mathcal{F}_L(\delta\mathcal{U}_F;\, \mathcal{U}_{0F},\, \underline{f}) := ||\mathcal{L}_F'(\mathcal{U}_{0F})\delta\mathcal{U}_F - (\underline{f} - \mathcal{L}_F(\mathcal{U}_{0F}))||^2$$

Now, the continuity of $\mathcal{F}_L$ in H^1 will be proven using the discussion above.

Lemma 6.2.1. ***(Continuity of the Augmented Fluidity Linearized Functional)*** *Let $\mathcal{L}'_F(\mathcal{U}_{0F})[\delta\mathcal{U}_F]$ represent the linearization of the fluidity form about the approximation $\mathcal{U}_{0F}$. Then, there exists a constant, C, depending on $\|\mathcal{U}_{0F}\|_\infty$ and $\|\underline{\underline{\nabla}}\,\hat{\underline{s}}_0\|_\infty$, such that*

$$\|\mathcal{L}'_F(\mathcal{U}_{0F})[\delta\mathcal{U}_F]\| \leq \mathcal{C}\|\delta\mathcal{U}_F\|_1. \tag{6.2.4}$$

Proof. We have

$$||\mathcal{L}'_F(\mathcal{U}_{0F})\delta\mathcal{U}_F||^2 \leq ||L_F\delta\mathcal{U}_F||^2 + ||\mathcal{N}'_F(\mathcal{U}_{0F})\delta\mathcal{U}_F||^2$$

From bounds (6.2.2) and (6.2.3)

$$\leq 2||\delta\mathcal{U}_F||_1^2 + {C_3}^2||\delta\underline{\hat{s}}||_1^2$$

Therefore, $\mathcal{C} = \sqrt{2\text{Max}(2, {C_3}^2)}$ and $\mathcal{F}_L$ is continuous in H^1. □

Showing continuity for the basic fluidity formulation is exactly the same as for the augmented continuity with Equations (6.1.5) and (6.1.8) removed. This would result in a smaller $\mathcal{C}$.

6.2.2 Viscosity Formulation

The proof of continuity for the velocity-gradient viscosity formulation follows the same format as for the augmented fluidity formulation. Start by bounding the linear portion of $\mathcal{L}'_V(\mathcal{U}_{0V})[\delta\mathcal{U}_V]$.

$$\begin{aligned}
||L_V\delta\mathcal{U}_V||^2 &= ||\delta\underline{\underline{U}} - \nabla\delta\underline{u}||^2 + ||\nabla\cdot\delta\underline{u}||^2 + ||\nabla\delta\hat{p}||^2 + ||\nabla\times\delta\underline{\underline{U}}||^2 \\
&\leq ||\delta\underline{\underline{U}}||^2 + ||\nabla\delta\underline{u}||^2 + ||\nabla\cdot\delta\underline{u}||^2 + ||\nabla\delta\hat{p}||^2 + ||\nabla\times\delta\underline{\underline{U}}||^2 \\
&\leq ||\nabla\delta\underline{u}||^2 + ||\nabla\cdot\delta\underline{u}||^2 + 2||\delta\underline{u}||^2 \\
&+ ||\delta\underline{\underline{U}}||^2 + ||\nabla\times\delta\underline{\underline{U}}||^2 + 2||\nabla\delta\underline{\underline{U}}||^2 \\
&+ ||\nabla\delta\hat{p}||^2 + ||\delta\hat{p}||^2 \\
&\leq 2||\delta\underline{u}||_1^2 + 2||\delta\underline{\underline{U}}||_1^2 + ||\delta\hat{p}||_1^2 = 2||\delta\mathcal{U}_V||_1^2.
\end{aligned}$$

Therefore,

$$||L_V\delta\mathcal{U}_V|| \leq \sqrt{2}||\delta\mathcal{U}_V||_1 \tag{6.2.5}$$

Now a bound is found for the nonlinear term.

$$||\mathcal{N}'_V(\mathcal{U}_{0V})\delta\mathcal{U}_V||^2 = \left\|\nabla\cdot\mu\left(\underline{\underline{U}}+\underline{\underline{U}}^T\right)\right\|^2$$
$$= \left\|2\nabla\cdot\mu\underline{\underline{\dot{\varepsilon}}}\right\|^2$$

Using the bound established in (6.1.18),

$$\leq {C_5}^2\|\underline{\underline{\dot{\varepsilon}}}\|_\infty^{-4/3}\|\nabla\underline{\underline{U}}\|^2$$
$$\leq {C_5}^2\|\underline{\underline{\dot{\varepsilon}}}_0\|_\infty^{-4/3}\|\nabla\delta\underline{\underline{U}}\|^2. \tag{6.2.6}$$

Now, Consider the linearized functional:

$$\mathcal{F}_V(\delta\mathcal{U}_V;\,\mathcal{U}_{0V},\,\underline{f}) := ||\mathcal{L}'_V(\mathcal{U}_{0V})\delta\mathcal{U}_V - (\underline{f}-\mathcal{L}_V(\mathcal{U}_{0V}))||^2$$

Now, the continuity of $\mathcal{F}_V$ in H^1 will be proven using the discussion above.

Lemma 6.2.2. ***(Continuity of the Viscosity Linearized Functional)*** *Let $\mathcal{L}'_V(\mathcal{U}_{0V})[\delta\mathcal{U}_V]$ represent the linearization of the viscosity form about the approximation $\mathcal{U}_{0V}$. Then, there exists a constant, $\mathcal{C}$, dependent on $\|\mathcal{U}_{0V}\|_\infty$, $\|\mu_0\|_\infty$, and $\|\nabla\mu_0\|_\infty$, such that*

$$\|\mathcal{L}'_V(\mathcal{U}_{0V})[\delta\mathcal{U}_V]\| \leq \mathcal{C}\|\delta\mathcal{U}_V\|_1. \tag{6.2.7}$$

Proof. We have

$$||\mathcal{L}'_V(\mathcal{U}_{0V})\delta\mathcal{U}_V||^2 \leq ||L_V\delta\mathcal{U}_V||^2 + ||\mathcal{N}'_V(\mathcal{U}_{0V})\delta\mathcal{U}_V||^2$$

From bounds (6.2.5) and (6.2.6)

$$\leq 2||\delta\mathcal{U}_V||_1^2 + {C_5}^2||\delta\underline{\hat{\sigma}}'||_1^2$$

Therefore, $\mathcal{C} = \sqrt{2\text{Max}(2, C_5^2)}$ and $\mathcal{F}_V$ is continuous in H^1. □

6.3 Coercivity

In this section, the coercivity of the FOSLS functionals is discussed. In general, the coercivity of Fréchet linearizations of all forms is an open question. This is primarily due to boundary conditions. In this section, the question is set in the context of known results.

First, consider the viscosity form. The full Fréchet linearization is quite complex and has not been thoroughly analyzed to date. However, consider a Picard-type linearization in which the viscosity, μ, is evaluated at the current approximation. Then, the momentum equation, the only nonlinear term, takes on the form

$$\nabla \cdot \hat{\mu}_0(\underline{\underline{\delta U}} + (\underline{\underline{\delta U}})^T) - \nabla p. \tag{6.3.1}$$

It was shown in [34] that, with normal stress boundary conditions, if $0 < c_0 \leq \hat{\mu}_0 \leq c_1 < \infty$, then the linearized functional is coercive with $\underline{\underline{U}} + \underline{\underline{U}}^T \in H(\text{div})$ and $\underline{u} \in H^1$. With the boundary conditions considered here, or if $\hat{\mu}_0$ is not bounded above and below, the result is an open question.

Now, consider the full viscosity functional with the addition of the curl and trace equations, (5.2.1)-(5.2.5), again using the Picard-type linearization in (6.3.1) and normal stress boundary conditions. It is straight forward to establish that, when the trace constraint is enforced, the linearized viscosity functional is then coercive with $\underline{\underline{U}} \in H(\text{div}) \cap H(\text{curl})$ and $\underline{u} \in H^1$. For simple domains this yields $\underline{\underline{U}} \in H^1$. However, the result remains open for the boundary conditions used here.

Consider the basic fluidity formulation found in (5.4.2)-(5.4.6), equations. The proofs in [13] and [34] can be modified to show that, with either full velocity boundary conditions or full normal stress boundary conditions, the linearized basic fluidity functional presented in (6.1.4), (6.1.6), (6.1.7) is coercive with $\underline{s} \in H(\text{div})$ and $\underline{u}, p \in H^1$. This result holds even if $\phi = \psi = 0$. With the periodic domain and mixed velocity and normal stress boundary conditions, as studied in this paper, the same result appears to be obtainable, but has not yet been established.

If the augmented fluidity functional is formed using the full set of equations, (5.4.20), and either full velocity or full normal stress boundary conditions, in a simple domain, and $\phi, \psi > 0$, then

the linearized from presented in (6.1.2)-(6.1.8) can be shown to be coercive with $\underline{s}, \omega, p, \underline{u} \in H^1$. This can be established by two approaches. The first is to use the result in the previous paragraph and show that the last two equations of (5.4.20) enforce a curl constraint. The second is by applying the theory of Agmon, Douglis, and Nirenberg [4, 9] to the differential blocks in (5.4.20). It is straightforward to confirm that the system involving the last four equations in (5.4.20) is H^1-elliptic in the sense of ADN. (See [9], page 594.) This involves demonstrating that the determinant of a scaled form of the symbol has the correct properties. Again, with the boundary conditions presented here, or if ϕ, ψ are not bounded away from zero, coercivity is an open question.

Chapter 7

Rectangular Glacier

This chapter describes a simple test problem designed to test the performances of the viscosity and augmented fluidity formulations.

7.1 Problem Setup

To compare the viscosity and augmented fluidity formulations, a simple test is performed involving an infinitely long glacier sliding down an infinitely long hill. A periodic glacier is used to approximate the infinitely long glacier. To make computation easier, the physical domain is rotated so that the computational domain is simply a rectangle. This computational domain has rotated gravity so that $\underline{g} = [|g|\sin(\theta), -|g|\cos(\theta)]^T$ as seen in Figure 7.1. The parameters used in this test are listed in Table 7.1.

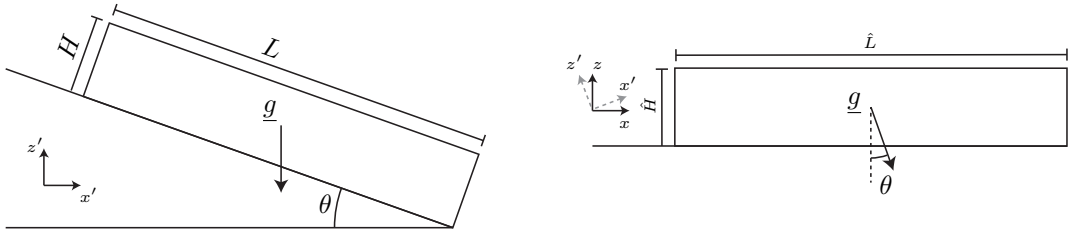

Figure 7.1: A cross section of the rectangular glacier, with the physical domain on the left and the computational domain on the right.

The boundary conditions used in this test problem mimic those found in the benchmark problems in the Ice Sheet Model Intercomparison Project for Higher-Order Ice Sheet Models (ISMIP-

Table 7.1: Parameters used in the test problem

Parameter	Value	Units
A	4×10^{-24}	$\mathrm{Pa}^{-3}\mathrm{s}^{-1}$
$\lvert g \rvert$	9.81	$\mathrm{m/s}^2$
ρ	900	$\mathrm{kg/m}^3$
$H,\ \hat{H}$	1000, 1	m, km
$L,\ \hat{L}$	10000, 10	m, km
θ	0.05	radians
n	3	

HOM) [39]. Stress-free and no-slip boundary conditions are imposed on the top and bottom, respectively. Periodic boundary conditions are imposed on the left and right sides.

The stress-free boundary conditions for the viscosity formulation are enforced by setting:

$$\underline{\underline{\sigma}} \cdot \underline{n} = 0,$$

where $\underline{\underline{\sigma}} \cdot \underline{n}$ is the stress vector acting on the plane whose normal is $\underline{n}$. In the test problem, this becomes

$$\begin{aligned}
\underline{\underline{\sigma}} \cdot \underline{n} &= \left(\hat{\mu}\left(\underline{\underline{U}} + \underline{\underline{U}}^T\right) - \hat{p}\underline{\underline{I}}\right) \cdot \underline{n} \\
&= \begin{bmatrix} 2\hat{\mu}U_{11} - \hat{p} & \hat{\mu}U_{12} + \hat{\mu}U_{21} \\ \hat{\mu}U_{21} + \hat{\mu}U_{12} & 2\hat{\mu}U_{22} - \hat{p} \end{bmatrix} \begin{bmatrix} 0 \\ 1 \end{bmatrix} \\
&= \begin{bmatrix} U_{12} + U_{21} \\ 2\hat{\mu}U_{22} - \hat{p} \end{bmatrix} = 0.
\end{aligned}$$

Using the fact that the trace condition is enforced by setting $\hat{U}_{22} = -\hat{U}_{11}$, the conditions for the top of the domain are $U_{12} + U_{21} = 0$ and $2\hat{\mu}U_{11} + \hat{p} = 0$.

The same boundary condition for the augmented fluidity formulation is:

$$\begin{aligned}
\underline{\underline{\sigma}} \cdot \underline{n} &= \left(\underline{\underline{s}} - \hat{p}\underline{\underline{I}}\right) \cdot \underline{n} \\
&= \begin{bmatrix} s_{11} - \hat{p} & s_{12} \\ s_{12} & -s_{11} - \hat{p} \end{bmatrix} \begin{bmatrix} 0 \\ 1 \end{bmatrix} \\
&= \begin{bmatrix} s_{12} \\ s_{11} + \hat{p} \end{bmatrix} = 0.
\end{aligned}$$

The no-slip condition means that the bottom of the glacier is frozen to the bed, or

$$\underline{u}(x,0) = \underline{0}.$$

This yields the additional condition that the derivative of velocity in the x direction is also zero, that is,

$$\frac{\partial \underline{u}(x,0)}{\partial x} = \underline{0}.$$

For the viscosity formulation, this translates into $U_{11} = 0$ and $U_{21} = 0$ at the bed of the glacier. The boundary conditions for the augmented fluidity formulation are more complicated since the gradient of velocity needs to be reconstructed. The resulting boundary conditions are:

$$\nabla \underline{u} \cdot t = \frac{1}{2} \begin{bmatrix} \phi s_{11} & \phi s_{12} - \psi\omega \\ \phi s_{12} + \psi\omega & -\phi s_{11} \end{bmatrix} \cdot \begin{bmatrix} 1 \\ 0 \end{bmatrix} = 0$$

$$\begin{bmatrix} \phi s_{11} \\ \phi s_{12} + \psi\omega \end{bmatrix} = 0.$$

This implies $s_{11} = 0$ and $\phi s_{12} + \psi\omega = 0$ on the bottom. The complete boundary conditions are found in Table 7.2.

Table 7.2: Boundary conditions for the Rectangular test problem

Viscosity Formulation			Fluidity Formulation		
Bottom	Top	Sides	Bottom	Top	Sides
$u_1 = 0$	$U_{12} + U_{21} = 0$	Periodic	$u_1 = 0$	$s_{12} = 0$	Periodic
$u_2 = 0$	$2\hat{\mu}U_{11} + \hat{p} = 0$		$u_2 = 0$	$s_{11} + \hat{p} = 0$	
$U_{11} = 0$			$s_{11} = 0$		
$U_{21} = 0$			$\phi s_{12} + \psi\omega = 0$		

Since the domain with its boundary conditions is constant along the x direction, the velocity profile is of the form $u = [u_1, u_2]^T = [f(z), 0]^T$. Using a gravity based forcing function, $\underline{f} =$

$[f_1, f_2]^T = \hat{\rho}\underline{g}$, as the right hand side yields an exact solution:

$$\begin{aligned} s_{12}(x,z) &= f_1(\hat{H} - z), \\ \omega(x,z) &= -c_\omega f_1(\hat{H} - z), \\ \hat{p}(x,z) &= -f_2(\hat{H} - z), \\ u_1(x,z) &= \frac{1}{8}{f_1}^3(\hat{H}^4 - (\hat{H} - z)^4), \\ u_2(x,z),\ s_{11}(x,z) &= 0, \end{aligned}$$

where $c_\omega \approx -0.682328$ is the real root of ${c_\omega}^3 + c_\omega - 1 = 0$. When using quadratic finite elements, this solution is nearly within the finite element space. This results in solving to machine precision on the coarsest grid, which obscures the numerical analysis. To get out of the finite element space while remaining similar to the physics-based, exact solution, the forcing function is modified to:

$$\underline{f} = \left[\frac{1}{2}\pi \sin\left(\frac{\pi z}{2}\right),\ -\frac{1}{2}\pi \sin\left(\frac{\pi z}{2}\right)\right]^T. \tag{7.1.1}$$

This results in the exact solution seen in Table 7.3.

Table 7.3: Exact solution to the viscosity and augmented fluidity formulations on the rectangular domain using the forcing function in equation (7.1.1)

Viscosity Formulation			Fluidity Formulation		
U_{11}	=	0	s_{11}	=	0
U_{12}	=	$\frac{1}{2}\cos^3\left(\frac{\pi z}{2}\right)$	s_{12}	=	$\cos\left(\frac{\pi z}{2}\right)$
U_{21}	=	0	ω	=	$c_\omega \cos\left(\frac{\pi z}{2}\right)$
p	=	$\cos\left(\frac{\pi z}{2}\right)$	p	=	$\cos\left(\frac{\pi z}{2}\right)$
u_1	=	$\frac{\sin\left(\frac{\pi z}{2}\right)(\cos(\pi y)+5)}{6\pi}$	u_1	=	$\frac{\sin\left(\frac{\pi z}{2}\right)(\cos(\pi y)+5)}{6\pi}$
u_2	=	0	u_2	=	0

Looking at the velocity profile for the solution in Table 7.3, notice that velocity gradients go to zero at the surface. The glacier moves like a solid chunk and the viscosity becomes infinite at the surface. Figure 7.2 displays the velocity profile and the profile of $\dot{\varepsilon}_e^{-\frac{2}{3}}$ as a function of height. Looking at $\dot{\varepsilon}_e^{-\frac{2}{3}}$ as a function of thickness confirms that the viscosity becomes infinite at the surface.

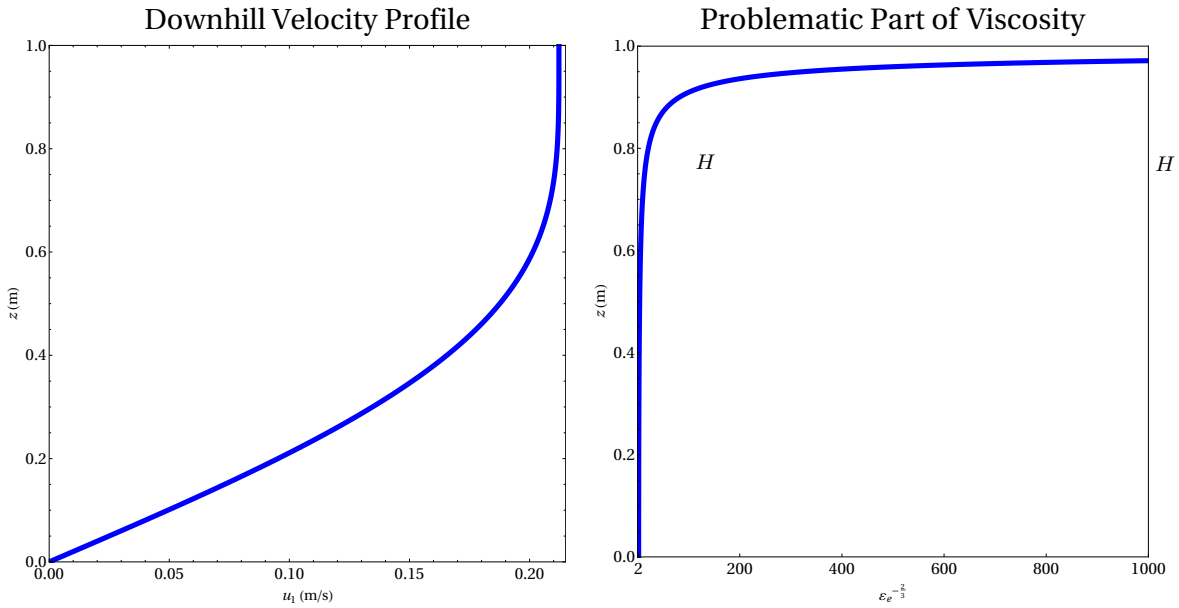

Figure 7.2: The velocity profile (left) shows the flattening near the surface of the glacier. The problematic portions of the viscosity shows the rapid growth of viscosity as $z \to \hat{H} = 1$ km.

7.2 Numerical Results

For comparison, both the viscosity and augmented fluidity formulations were run on the rectangular glacier problem under the same conditions. Both systems were solved in FEniCS using CG preconditioned with BoomerAMG from hypre [1, 31]. The scaling in the augmented formulation is $\varphi = \psi$. In order to get the viscosity formulation to converge, the constant, c, in the viscosity definition from equation (2.3.12) was chosen to be 1×10^{-4}. This value was selected by varying c from 1×10^{-1} to 1×10^{-16} by powers of 10 and looking for which c gave the best balance between performance accuracy. It should be noted that smaller values of c produce approximate solutions that are more accurate. However, the smaller constants decrease AMG performance to the point that comparison becomes difficult. Since the viscosity form uses a regularization constant in equation (2.3.12), the right-hand side is properly calculated to include this constant so that both formulations converge to the solution in Table 7.3.

Computations were performed using biquadratic finite elements on a uniform mesh with mesh spacing h. Figure 7.3 shows how the FOSLS functional is reduced with refinement. Since refinement is uniform with quadratic elements on a uniform grid, the FOSLS functional is expected to reduce with $\mathcal{O}(h^2)$ [10]. It can be clearly seen in Figure 7.3 that both formulations are working as theory predicts.

The next step is to look at how each formulation converges to the exact solution in the L^2 norm. If the FOSLS functional has full H^1 regularity and quadratic elements are used, the L^2 error is expected to decrease with $\mathcal{O}(h^3)$ [10]. Figure 7.4 shows that this is true for both formulations, but the augmented fluidity formulation yields a smaller L^2 error. In this test, the viscosity formulation had approximately 54 times the L^2 error of the augmented fluidity formulation on the same grid. Not only does the augmented fluidity formulation require less work, as explained in the following paragraph, it is also more accurate.

Next, we compare the work each formulation required to achieve convergence. Figure 7.5 shows how AMG performed on the two formulations. The AMG convergence factor is the factor

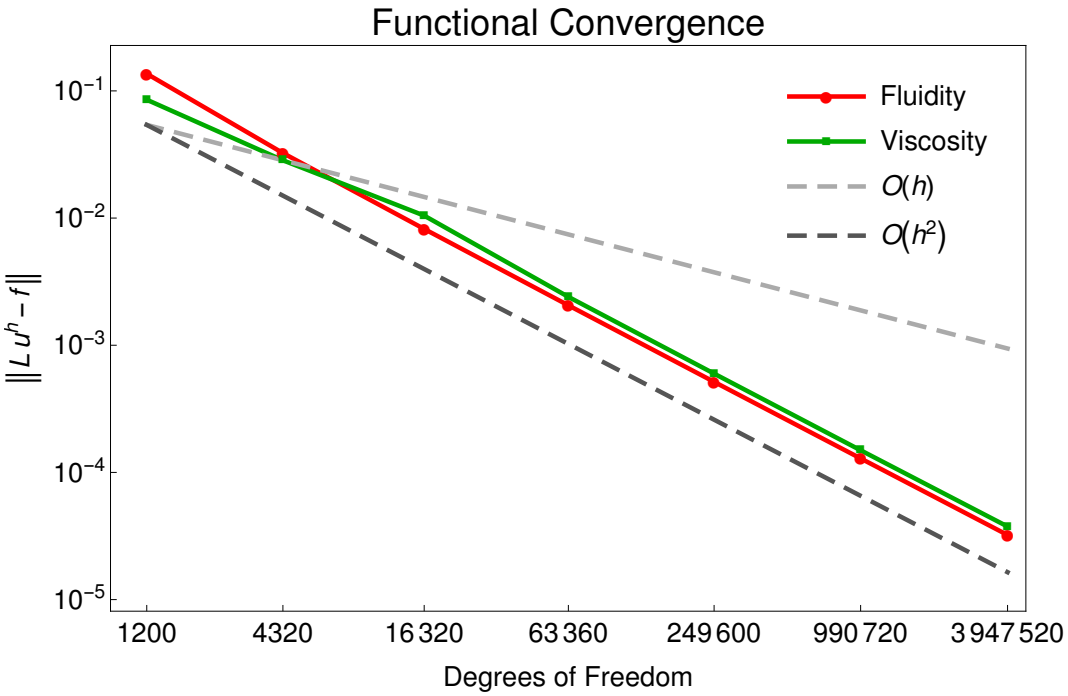

Figure 7.3: The FOSLS functional for the two formulations as a function of the number of degrees of freedom using an uniform grid with uniform refinement.

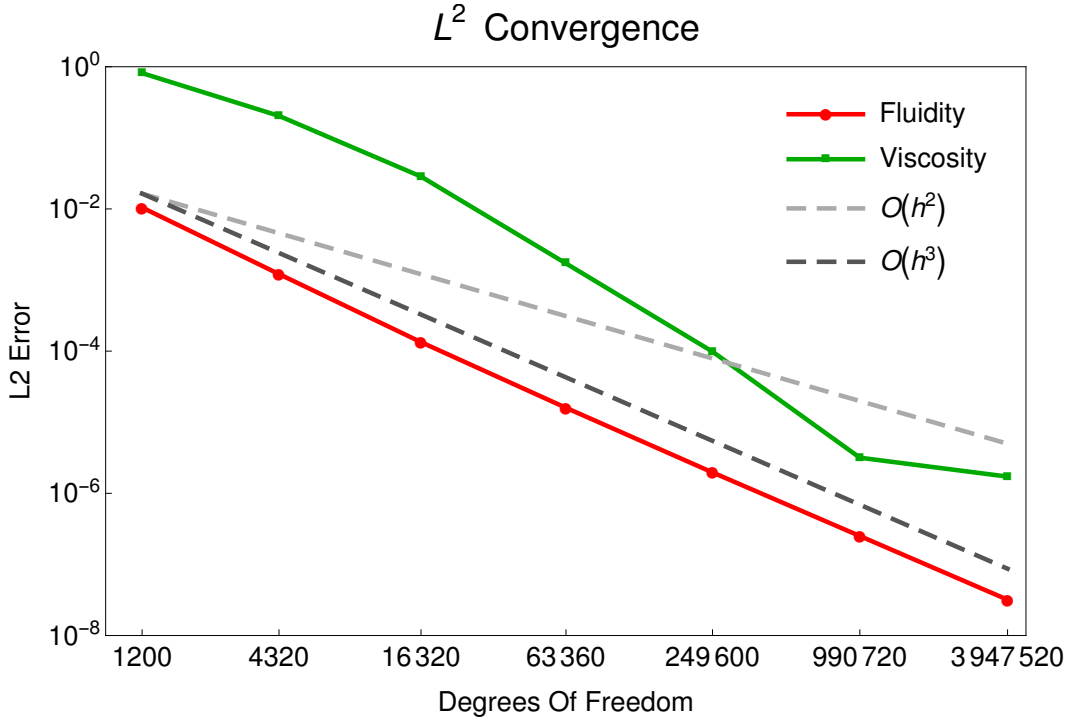

Figure 7.4: The sum of the L^2 error for each of the unknowns for the rectangular glacier problem.

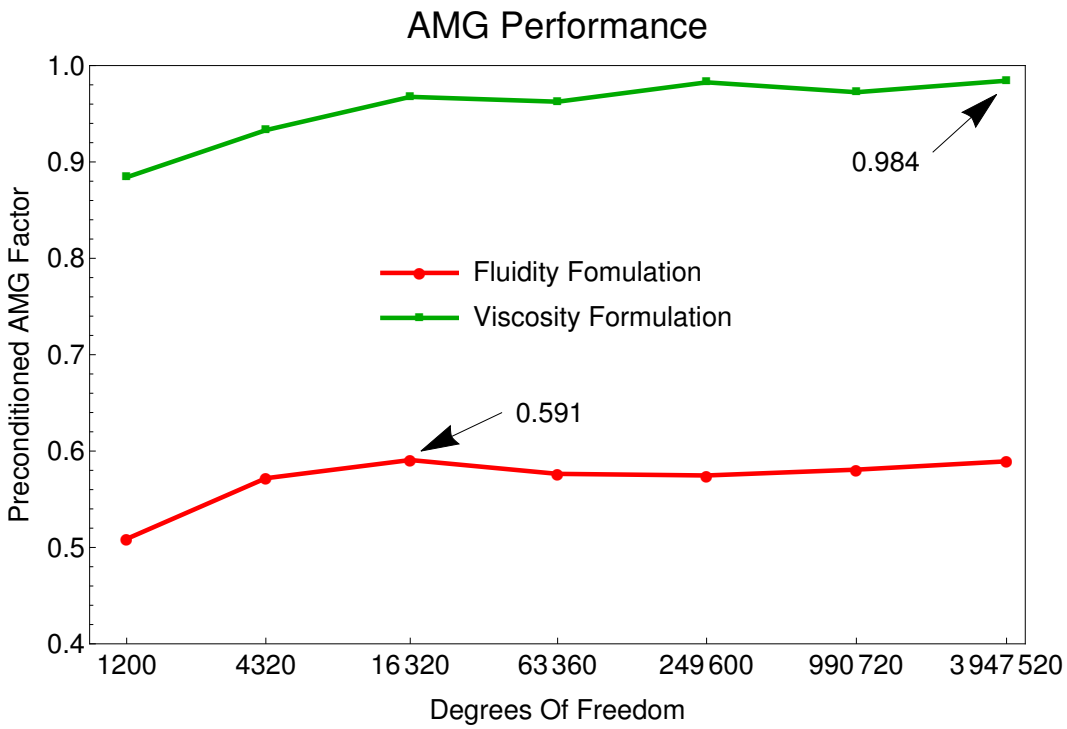

Figure 7.5: The AMG factor as a function of the number of degrees of freedom for the viscosity and augmented fluidity formulations.

by which the residual is reduced in one V(1,1)-cycle. Notice the that maximum AMG convergence factor for the viscosity formulation is $CF_v = 0.984$, while the maximum for the augmented fluidity formulation is only $CF_f = 0.591$. A quick calculation shows that about 33 V-cycles with convergence factor CF_v are required to achieve a reduction equal to one step with convergence factor CF_f. It takes the viscosity formulation 33 times the work to reduce the residual to the same level as with the augmented fluidity formulation. This is examined further by looking at the total number of work units (WU) required by each formulation to reach the solution (Tables 7.4-7.5). A work unit is the amount of work required to calculate a residual on the fine grid.

One of the nice features of Newton-FOSLS-NI methodology is that most of the work is done on the coarse grid. Starting with a uniform 20×2 grid, the grid is refined 6 times to get a final, fine grid. On the coarsest grid, the Newton iteration is initialized with a reasonable initial guess. On subsequent levels, the solution from the previous level is used as the initial guess.

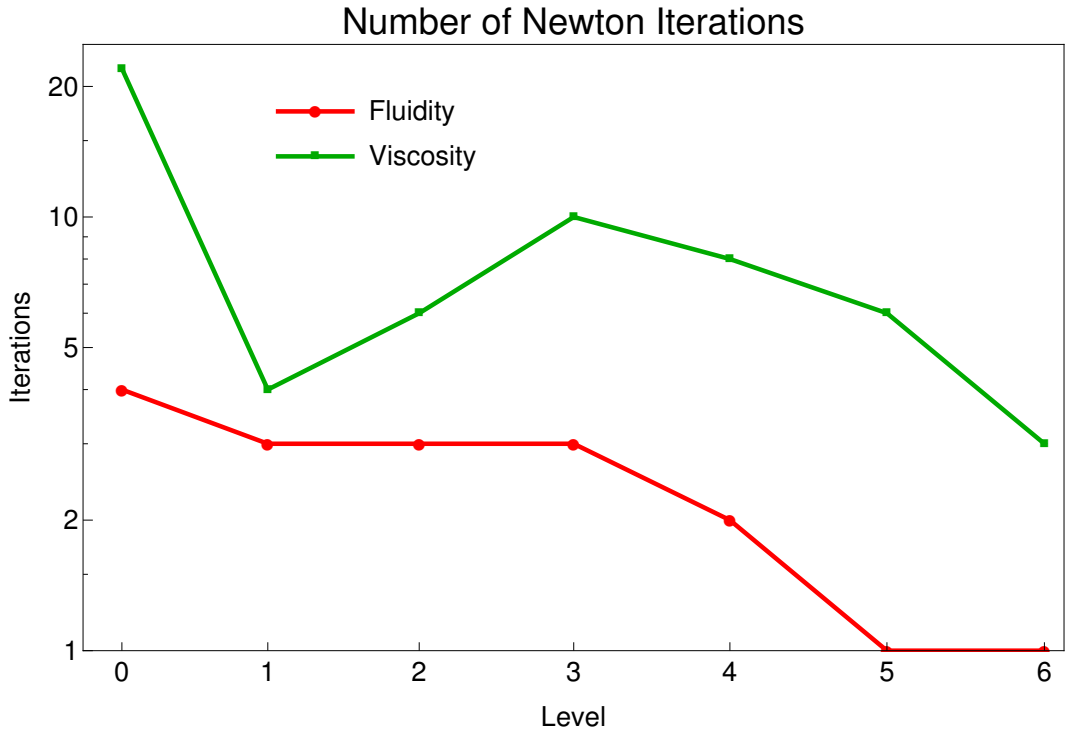

Figure 7.6: This graph show the number of Newton iterations required to solve the nonlinear problem on each level of refinement with 0 denoting the coarsest grid and 6 the finest.

Figure 7.6 shows the number of Newton iterations required to solve the nonlinear problem. Notice that most of the iterations occur on the coarse grid for the augmented fluidity formulation. For problems with sufficient regularity, it can be shown that as the mesh is refined, only one Newton step and a fixed number of AMG cycles are required to resolve the solution [17, 18].

Table 7.4: Summary of the viscosity formulation's numerical performance. E is the number of elements. N is the number of Newton steps. Comp lists the cycle complexity for each Newton step. WU is the total number of work units for that level. Functional refers to the nonlinear functional norm.

Level	E	Nonzeros	N	Comp	V-Cycles	WU	Functional
1	80	72000	22	1.57	60.82	1.49	8.52×10^{-2}
2	320	276480	4	1.78	55.25	1.07	2.85×10^{-2}
3	1280	1082880	6	1.94	96.67	11.94	1.05×10^{-2}
4	5120	4285440	10	1.97	112.90	93.57	2.40×10^{-3}
5	20480	17049600	8	2.01	129.00	346.70	5.98×10^{-4}
6	81920	68014080	6	2.03	130.30	1061.00	1.49×10^{-4}
7	327680	271687680	3	2.04	124.30	2033.00	3.76×10^{-5}
					Total	3550.00	

Table 7.5: Summary of the augmented formulation's numerical performance.

Level	E	Nonzeros	N	Comp	V-Cycles	WU	Functional
1	80	72000	4	1.34	13.50	0.05	1.36×10^{-1}
2	320	276480	3	1.62	14.67	0.19	3.25×10^{-2}
3	1280	1082880	3	1.78	16.67	0.94	8.21×10^{-3}
4	5120	4285440	3	1.86	17.67	4.15	2.06×10^{-3}
5	20480	17049600	2	1.91	18.00	11.49	5.15×10^{-4}
6	81920	68014080	1	1.95	17.00	22.11	1.29×10^{-4}
7	327680	271687680	1	1.96	19.00	99.34	3.22×10^{-5}
					Total	138.30	

To calculate the cost of both formulations, a test was run with an initial guess of the exact solution injected to a coarse grid corresponding with Level 0. This simulates solving the nonlinear problem on the coarse grid (Level 0) by some means and interpolating that solution to Level 1. The idea is that since the coarse grid is very sparse, the full spectrum of nonlinear solvers could be employed at minimal cost. The summary of these runs can be found in Tables 7.4-7.5. A single work unit is equal to the work required to perform one relaxation on the fine grid, in this case Level

6. Then, the proportional number of work units for each level is the product of nonzeros, cycle complexity, and the number of V-Cycles for that level, divided by the number of nonzeros on the fine grid. Since V(1,1) cycles were used, this number is multiplied by 8/3. V(1,1) cycles perform one relaxation before and one after the coarse grid correction. For the augmented fluidity run, the total number of work units was 138.30, which is approximately the work required to perform 139 relaxations on the fine grid. In comparison, the viscosity formulation took 3550.0 work units to solve, which is just over 25 time more expensive than the augmented fluidity formulation for a significantly less accurate in the L^2 norm.

This test problem shows that clearly, a fluidity-based FOSLS formulation performs better than a viscosity-based formulation. The next couple of test problems look into how to properly optimize a fluidity-based FOSLS formulation, and compare said formulation to a commonly used Taylor-Hood Galerkin method described in 5.1.

Chapter 8

ISMIP: Benchmark B

This chapter explores benchmark Experiment B from the Ice Sheet Model Intercomparison Project (ISMIP). The performance of the fluidity formulations is compared with the Taylor-Hood Galerkin method along with results from a database of solutions from other models solving this problem. Additionally the difference between the basic and augmented fluidity formulations is examined.

8.1 Problem Setup

The next test comes from the Ice Sheet Model Intercomparison Project (ISMIP), specifically Experiment B [39]. The shape of the ISMIP-HOM-B benchmark domain is schematically shown in Figure 8.1 with an exaggerated surface slope.

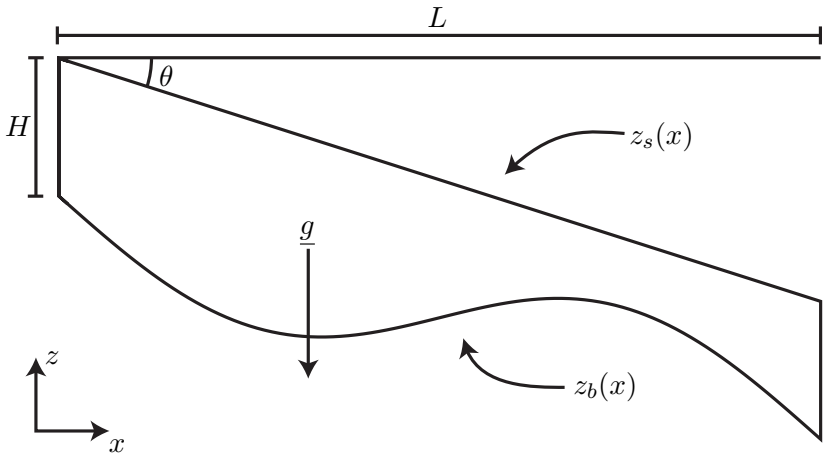

Figure 8.1: A cross section of the benchmark Experiment B.

The surface of the glacier is prescribed by

$$z_s(x) = -\tan(\theta)x,$$

and the basal topography is prescribed by

$$z_b(x) = z_s(x) - H + \beta H \sin(wx).$$

Unlike the rectangular glacier in Chapter 7, this domain is not rotated. The parameters used in Experiment B are listed in Table 8.1.

Table 8.1: Parameters used in the benchmark Experiment B

Parameter	Value	Units
A	10^{-16}	$\text{Pa}^{-3}\ \text{a}^{-1}$
$\|g\|$	9.81	m/s^2
ρ	910	kg/m^3
H	1	km
L	10	km
θ	0.5°	
w	$2\pi/L$	
β	0.5	
n	3	
Seconds per year	31,556,926	s/a

The boundary conditions used in Experiment B are similar to those found in the rectangular glacier problem. A no-slip condition is enforced at the bed. This also implies that the directional derivative in the direction of the tangent of the bed is equal to zero. A no-stress condition is enforced on the surface. Periodic boundary conditions are imposed on the left and right sides, which simulate an infinitely long glacier. The boundary conditions are summarized in Table 8.2.

Table 8.2: Boundary Conditions for benchmark B

Bottom	Top	Sides
$u_1 = 0$ $u_2 = 0$ $\nabla \underline{u} \cdot t = 0$	$\hat{\underline{\underline{\sigma}}} \cdot \underline{n} = 0$	Periodic

8.2 Numerical Solution Results

This section discusses the solution to benchmark B using the augmented fluidity formulation with $\psi = 1/2\left({s_{11}}^2 + {s_{12}}^2 + \omega^2\right)$ and $\varphi = 1$. The solution to benchmark B is approximated using the NI-Newton-FOSLS method implemented in the FEniCS Project using CG preconditioned with BoomerAMG from hypre [31, 1]. The problem is solved by initially using the basic fluidity formulation, (5.4.2)-(5.4.6), on the first two grids with an LU solver, to get a good initial guess. After that, the remaining grids are solved using the augmented fluidity formulations from Section 5.4. Uniform refinement is used for the first two grids and adaptive mesh refinement is used for the remaining grids. The solution from the augmented fluidity formulation is then compared with a compilation of various solutions from other Stokes and higher order methods models obtained from **The Cryosphere** at `http://www.the-cryosphere.net/2/95/2008/`.

Figure 8.2 shows the horizontal and vertical surface velocities as well as basal shear stress and the difference between basal pressure and hydrostatic pressure, $(\rho|g|H - p(x, z_b(x)))$. The database for this benchmark has several collected solutions from different models [39]. For comparison, these models are categorized as either a full-Stokes model or a higher-order model. Looking at Figure 8.2, it is easy to see that the fluidity formulation produces a solution that agrees with the average full-Stokes model and the Taylor-Hood method.

Another interesting aspect is how the viscosity is resolved with the augmented fluidity formulation. Since the augmented fluidity model does not impose any regularization on viscosity, it should be allowed to become as large as necessary. Another way of looking at this is that fluidity, the inverse of viscosity, can be as small as necessary. Figure 8.3 shows the log fluidity at the surface for the augmented fluidity formulation as well as the Taylor-Hood method. As expected, the augmented fluidity method produces smaller values corresponding to larger viscosities. Unfortunately, without an exact solution, it is unknown which value of fluidity is more physically correct.

Simply having smaller fluidities is not the full story. The fluidities calculated from the Taylor-Hood method have an add source of error. Since, s_{11} and s_{12} are not naturally calculated in the

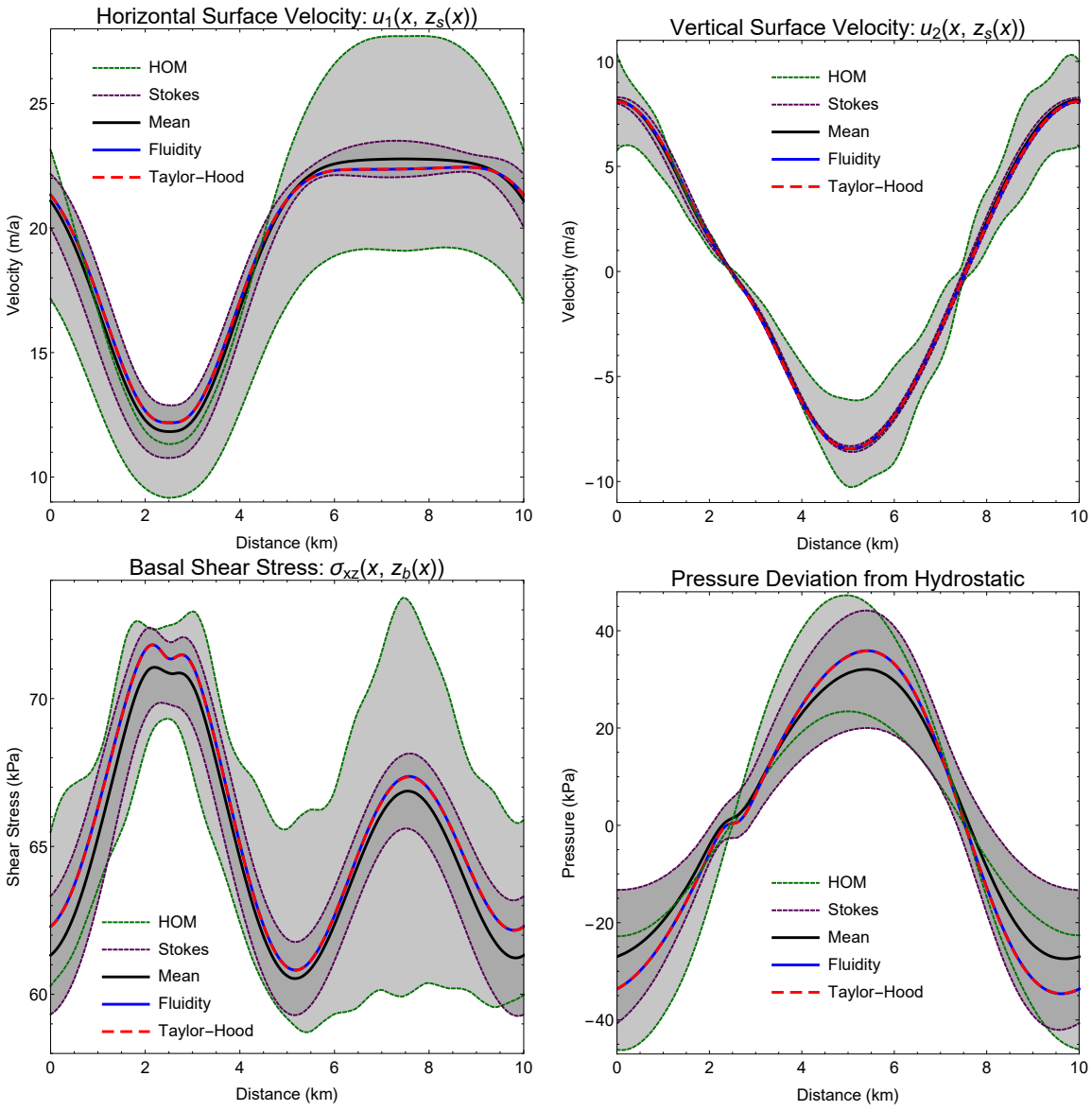

Figure 8.2: Various graphs of the augmented fluidity solution to benchmark Experiment B compared with other Stokes and higher order models. The light gray and gray bands represent one standard deviation of the higher order methods and full-Stokes models, respectively, with the average of the Stokes models represented as the gray line. The solid blue line is the solution calculated using the augmented fluidity model. The dashed red line is a solution obtained by using a viscosity based Galerkin method with Taylor-Hood elements as described in [30].

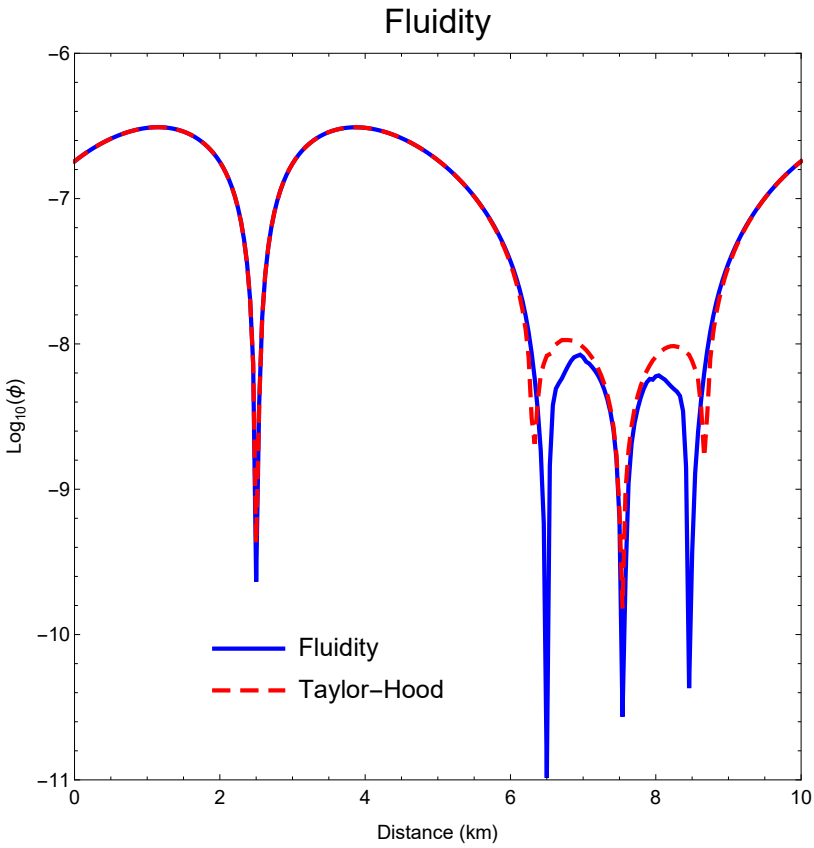

Figure 8.3: Fluidity at the surface as calculated by the augmented fluidity formulation (dashed line) and a Galerkin method using Taylor-Hood elements (solid line).

Taylor-Hood method, they must be approximated from u_1 and u_2 using numerical derivatives. This will reduced the the order of accuracy by a power of h. However, in the FOSLS formulation s_{11} and s_{12} are primary dependent variables and are approximated in a discrete subspace of H^1. The difference between the two different approximation can clearly be seen in Figure 8.4. Clearly, the Taylor-Hood method is going to have a difficult time recovering accurate fluidities with the numerical noise around the zeros of s_{11} and s_{12}.

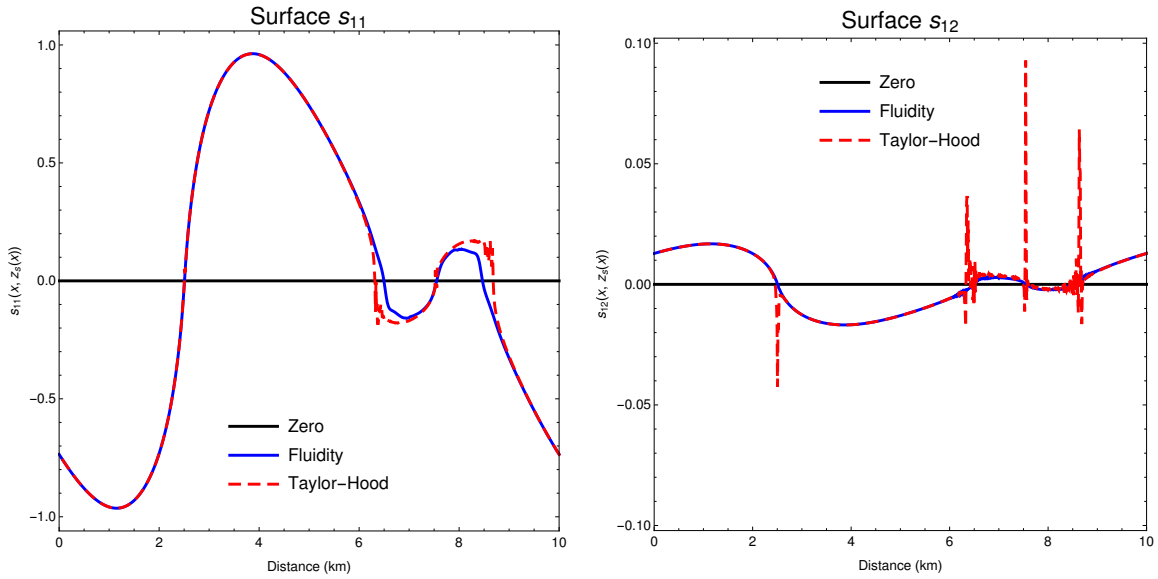

Figure 8.4: The two components of the deviatoric stress, s_{11} and s_{12}, evaluated at the surface as calculated using the augmented fluidity formulation (blue line) and a Galerkin method using Taylor-Hood elements (dashed red line).

Figure 8.5 shows contour plots for ϕ, $\log(\phi)$, ψ, $\log(\phi)$. The plots involving ϕ show that over the majority of the domain, ϕ is almost constant. The only places where the fluidity goes to zero are the two points near the surface above the peak and trough of the basal topography. This is made clearer in the $\log(\phi)$, and further shows how small the region where ϕ starts to diminish. Equation (5.3.6) show that $\phi = 0$ where there are solid-body rotation locally. Examining the velocity streamlines around the point where ϕ is small, shows a rounded behavior, which could indicate where the ice is rotating.

The plots involving ψ just show that ψ is well bounded above zero. In fact, the minimum is

greater than 0.24. The range of ψ is only an order of magnitude. This shows why scaling by $\psi^{-1/2}$ is not as effective as $\phi^{-1/2}$ for improving AMG performance.

Finally, the results of Adaptive Mesh Refinement on the benchmark B glacier for the augmented fluidity formulation are examined. Another useful aspect of solving a system using FOSLS is that the functional provides a locally sharp and globally reliable **a posteriori** error measure [7]. The adaptive refinement strategy known as ACE, described in [19, 35], was employed. The goal of ACE is to provide the best accuracy per computational cost. A side product of the ACE algorithm is that it constructs a nearly optimal grid and nearly equally distributed functional error.

After four levels of uniform refinement, the FOSLS functional is reduced to 1.02×10^{-3} with 69504 degrees of freedom, whereas with four levels of ACE refinement, the FOSLS functional is reduced to 2.90×10^{-3} with 28806 degrees of freedom. For less than half the number of degrees of freedom, ACE results in a functional that is the same magnitude when compared with uniform refinement.

The grid produced by ACE, displayed in Figure 8.6, is refined near locations were fluidity is nearly zero (viscosity is large) and around the line where $\phi/\psi = 1$ or, equivalently, where $\omega = 0$. The ACE algorithm promises to provide a greater advantage in problems for which the solution is more complex.

8.3 Comparing Fluidity Formulations

This section compares the performance of both the basic and augmented fluidity formulations. Currently, the augmented fluidity method (5.4.9)-(5.4.16) does not produce the optimal finite-element convergence rate of $O(h^2)$ for the benchmark Experiment B domain. The addition of the curl equations, (5.4.15)-(5.4.16), reduce the finite-element convergence. The convergence of the least-squares functional norm for various test is found in Figure 8.7.

These test involve scaling the curl equation by functions that either weaken/deemphasize (ϕ) or strengthen/emphasize ($\psi^{-1/2}$ or $\phi^{-1/2}$) the locations where ϕ is small. Adding the scaling produces the an additional nonlinearity, which is dealt with by a Picard-type linearizion that

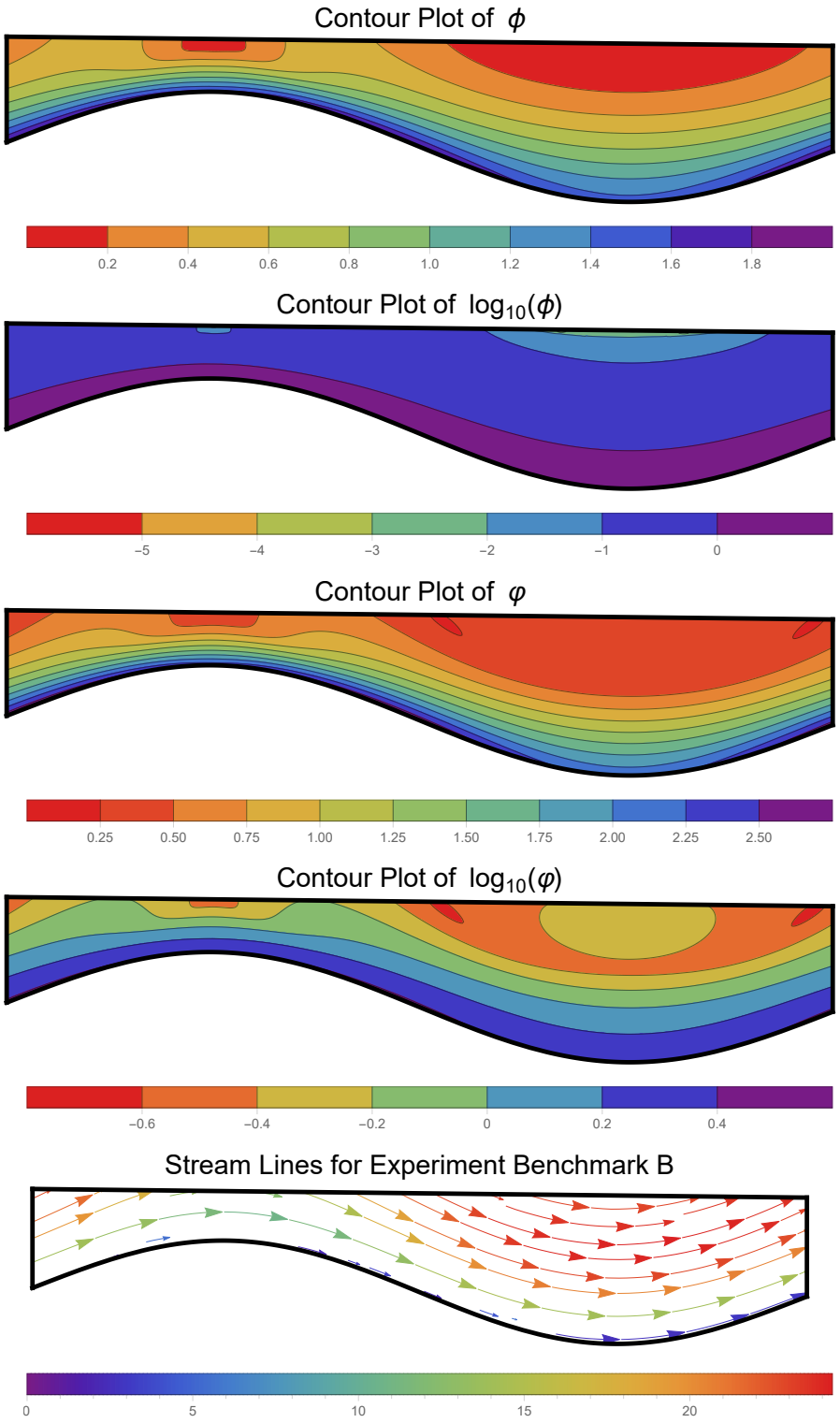

Figure 8.5: Contour plots of ϕ, $\log(\phi)$, ψ, $\log(\psi)$. The final plot show the streamlines for Experiment benchmark B.

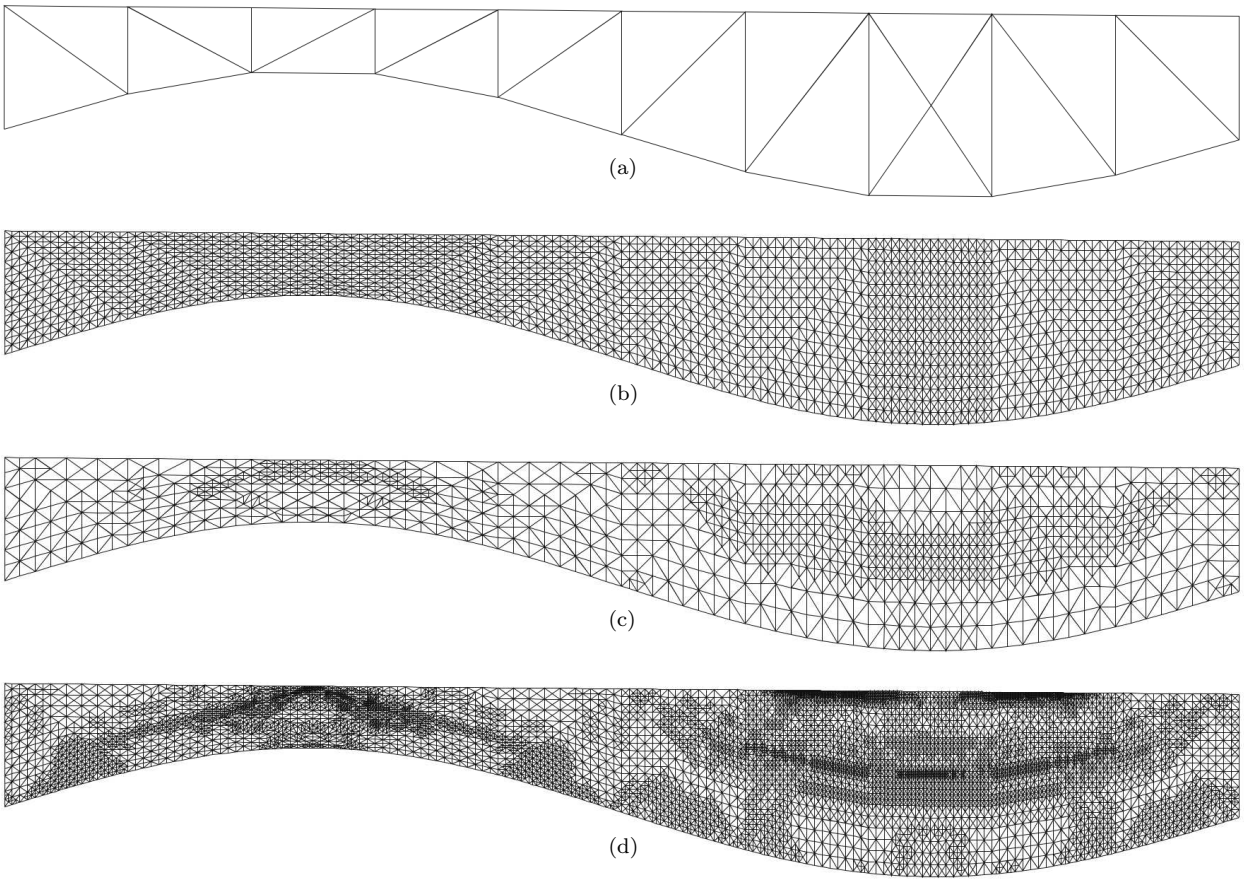

Figure 8.6: (a) The coarse grid, with 384 degrees of freedom, reduced the functional to 1.22. (b) After four uniform refinements resulting in 69504 degrees of freedom, the functional is reduced to 1.02×10^{-3}. (c) Starting on the coarse grid and refining four times with ACE results in 28806 and reduced the functional to 2.90×10^{-3}. (d) An additional three ACE refinement to 210954 degrees of freedom reduced the functional to 2.14×10^{-4}.

generates the scaling function based on the previous Newton step. The tests performed with the strong scalings started with two NI steps of the unscaled system to guarantee that the solution is in the basin of attraction. All of the test are performed on quadratic Lagrange elements for all unknowns. The "basic" case refers to solving the basic fluidity formulation, (5.4.2)-(5.4.6), and was still solved on quadratic Lagrange elements.

It should be noted that Figure 8.7 should not be used to compare the relative size of the least-squares functional, since the functional for each test depend on the scaling. This means that, since $\phi^{-1/2}$ is greater than one a majority of the domain, the functional associated with that scaling will be necessarily larger than the unscaled test. Figure 8.7 should just be used to compare the relative convergence rates.

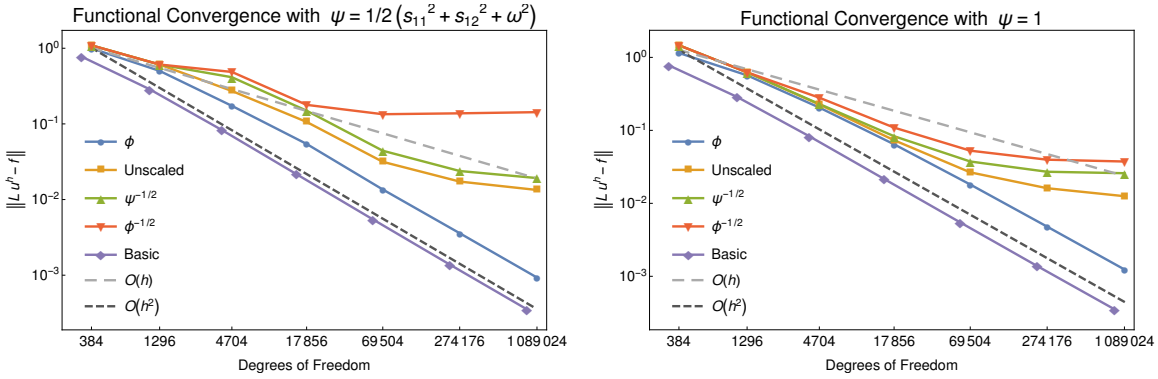

Figure 8.7: The functional norm convergence for $\psi = 1/2\left(s_{11}^2 + s_{12}^2 + \omega^2\right)$ (left) and $\psi = 1$ (right) with various scalings of the curl equations. For the case $\psi = 1$, the scaling $\psi^{-1/2}$ still uses the $1/2\left(s_{11}^2 + s_{12}^2 + \omega^2\right)$ definition only for the scaling. The "basic" case is solving the system in (5.4.2)-(5.4.6).

One possible explanation for this diminished behavior is due to the reduced regularity of the solution in a neighborhood around locations where $\phi \approx 0$. However, the basic fluidity form without the additional curl equations does converge optimally. The optimal $O(h^2)$ convergence rate can be recovered by scaling the curl equations by ϕ. This process "unweights" the problematic regions, and essentially ignores the locations of reduced regularity. Unfortunately, this modification produces degraded AMG performance, which can be seen in Figure 8.8. For these reasons, an iterative solver for basic fluidity system would be very useful for this type of problem.

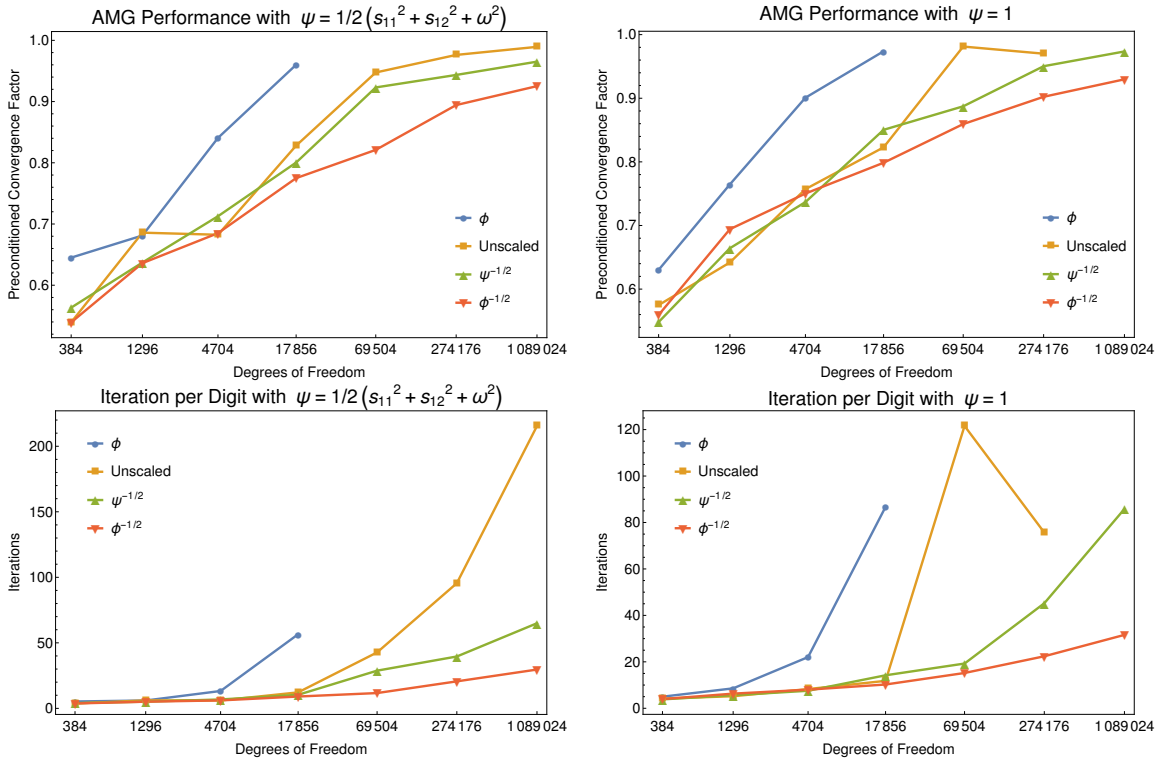

Figure 8.8: The CG preconditioned with AMG convergence factor (top) for $\psi = 1/2\left(s_{11}^2 + s_{12}^2 + \omega^2\right)$ (left) and $\psi = 1$ (right) with various scalings of the curl equations. The bottom graphs indicate how many iterations are required to reduce the functional by 0.1 at the given convergence factor. Each one of these points was found by taking the linear system from the final newton step and solving it with a zero right hand side and random initial guess. The points that were not plotted, were removed because they did not converge within 1000 iterations. For the case $\psi = 1$, the scaling $\psi^{-1/2}$ still uses the $1/2\left(s_{11}^2 + s_{12}^2 + \omega^2\right)$ definition only for the scaling.

Of the tests listed in Figures 8.7, Solving the basic fluidity formulation produces the more accurate solutions as seen in Figure 8.9. Notice that all of the test experience reduced convergence as the mesh gets refined. This is because the reference solution is from a data set provided in [30]. It is possible that the solution from that paper is only accurate to 1×10^{-4}, or it is possible that the first-order systems are converging to a close but slightly different solution.

The solution from the test where $\psi = 1/2\left({s_{11}}^2 + {s_{12}}^2 + \omega^2\right)$ with unscaled curl equations, was used to produce the graphs in Figures 8.2-8.5 because it produced accurate and interesting solutions.

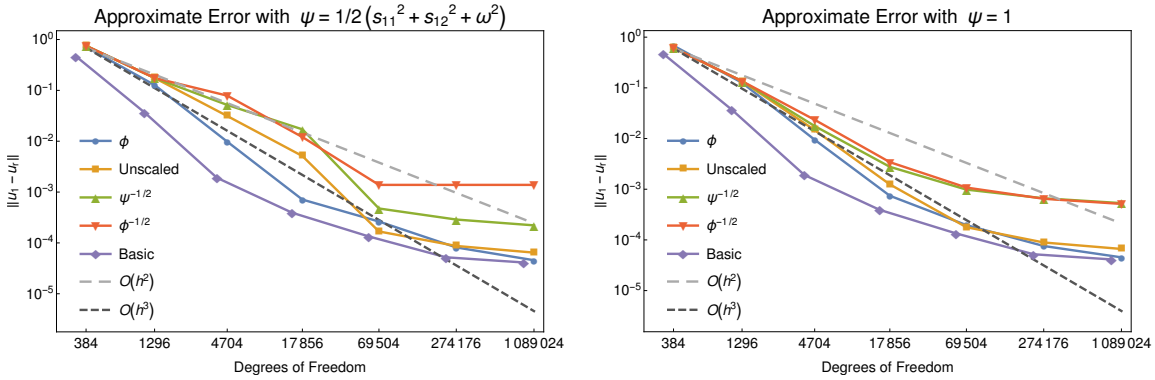

Figure 8.9: The L^2 convergence of the horizontal surface velocity, u_1, for $\psi = 1/2\left({s_{11}}^2 + {s_{12}}^2 + \omega^2\right)$ (left) and $\psi = 1$ (right) with various scalings of the curl equations. The solution provided in [30] is used as the reference, u_r. For the case $\psi = 1$, the scaling $\psi^{-1/2}$ still uses the $1/2\left({s_{11}}^2 + {s_{12}}^2 + \omega^2\right)$ definition only for the scaling. The "basic" case is solving the system in (5.4.2)-(5.4.6).

One such direction forward in recovering good AMG convergence factors while still maintaining optimal finite-element convergence would be to remove the curl equations all together and leverage an auxiliary space multigrid solvers that target $H(\text{div})$-elliptic systems, such as ADS [44]. Without the curl equations the augmented fluidity formulation can no longer be H^1-elliptic. Instead, the system becomes closer to an $H(\text{div})$-type elliptic system in s_{11}, and s_{12}, opening up the possibility of using an AMS/ADS solver applied as a block preconditioner to these variables.

Chapter 9

ISMIP: Benchmark D

This chapter discusses a test problem that involves basal sliding, which can cause large viscosities and is a good test case for a fluidity-based formulation.

9.1 Problem Setup

The next test problem also comes from the ISMIP series of benchmarks, specifically benchmark D. The domain used in benchmark D, like the rectangular problem from Chapter 7, is an infinitely long rectangular ice sheet flowing down an infinitely long hill. The resulting domain is a rectangle with periodic boundary conditions. The interesting feature of this problem is the bed experiences variable basal sliding, which is enforced by using the Rayleigh friction boundary conditions:

$$\underline{u} \cdot \underline{n} = 0, \qquad \underline{n} \cdot \underline{\underline{\sigma}} \cdot \underline{t} = \beta^2 \underline{u} \cdot \underline{t}, \tag{9.1.1}$$

where n and t are the boundary normal and tangent, and β^2 is the friction coefficient in Pa a m^{-1} [30]. In the case of benchmark D [39],

$$\beta^2 = 1000 + 1000 \sin(wx).$$

This is depicted as the red function in Figure 9.1, where the peak indicates where $\beta^2 = 2000$ Pa a m^{-1} and the trough is where $\beta^2 = 0$ Pa a m^{-1}. It is also important to note that glacier slope is $\theta = 0.1°$, but the computational domain is rotated to create a perfect rectangle. Table 9.1 list the various parameters in this benchmark.

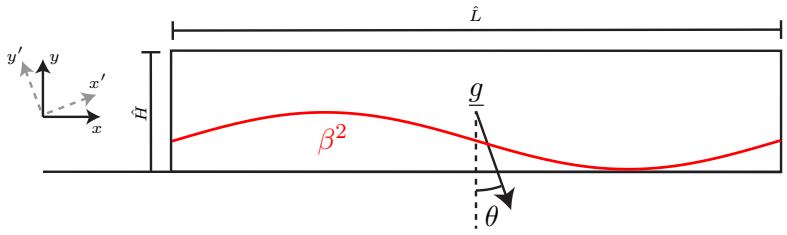

Figure 9.1: The domain for benchmark D. The red function is a depiction of the size of β^2.

Table 9.1: Parameters used in the benchmark D

Parameter	Value	Units
A	10^{-16}	$\text{Pa}^{-3}\ \text{a}^{-1}$
$\lvert g\rvert$	9.81	m/s^2
ρ	910	kg/m^3
$\hat{H}$	1	km
$\hat{L}$	10	km
θ	0.1°	
w	$2\pi/L$	
n	3	
Seconds per year	31,556,926	s/a

The first boundary condition in (9.1.1) is the no-penetration condition enforcing that ice not go through the boundary. The second condition is the expression for basal sliding. If β^2 is infinite, then $\underline{u} \cdot \underline{t} = 0$ and (9.1.1) reduces to simple no-slip boundary conditions as in an ice sheet with a frozen bed. On the other hand, when β^2 is very small, the ice is allowed to slip freely down the bed, which is a place where high viscosities are bound to show up. In this case, fluidity-based formulations are a better approach, which will be demonstrated in Section 9.2. Table 9.2 summarizes the boundary conditions for this problem.

In the Taylor-Hood Galerkin formulation from Section 5.1, (9.1.1) prevents the term, $\int_\Gamma n \cdot \underline{\underline{\sigma}} \cdot \underline{v}\, ds = 0$, from completely vanishing. Instead

$$\int_\Gamma n \cdot \underline{\underline{\sigma}} \cdot \underline{v}\, ds = \int_{\Gamma_s} n \cdot \underline{\underline{\sigma}} \cdot \underline{v}\, ds = -\int_{\Gamma_s} \beta^2 \underline{u} \cdot \underline{v}\, ds = 0$$

In the FOSLS formulations, (9.1.1) is enforces via explicitly adding them as boundary functionals.

Table 9.2: Boundary conditions for benchmark D

Bottom			Top	Sides
$\underline{u} \cdot \underline{n}$	$=$	0	$\hat{\underline{\underline{\sigma}}} \cdot \underline{n} = 0$	Periodic
$\underline{n} \cdot \hat{\underline{\underline{\sigma}}} \cdot \underline{t}$	$=$	$\beta^2 \underline{u} \cdot \underline{t}$		

9.2 Numerical Solution Results

This section discusses the solution to benchmark D using the augmented fluidity formulation with $\psi = 1/2\left({s_{11}}^2 + {s_{12}}^2 + \omega^2\right)$ and $\varphi = 1$. Just like with benchmark B in Chapter 8, this problem is solved with the NI-Newton-FOSLS method by solving equations (5.4.2)-(5.4.6) on the first two grids with just the basic fluidity formulation to ensure the solution is in the basin of attraction for Newton. This is because the curl equations in the augmented formulation can derail Newton if not properly treated. After that, the approximation on each grid is obtained using the augmented fluidity formulation. This method is implemented in the FEniCS and Dolfin finite-element packages for python [31]. The resulting solution is then compared with a compilation of

results from other Stokes and higher order methods models obtained from **The Cryosphere** at `http://www.the-cryosphere.net/2/95/2008/`. This comparison is found in Figure 9.2.

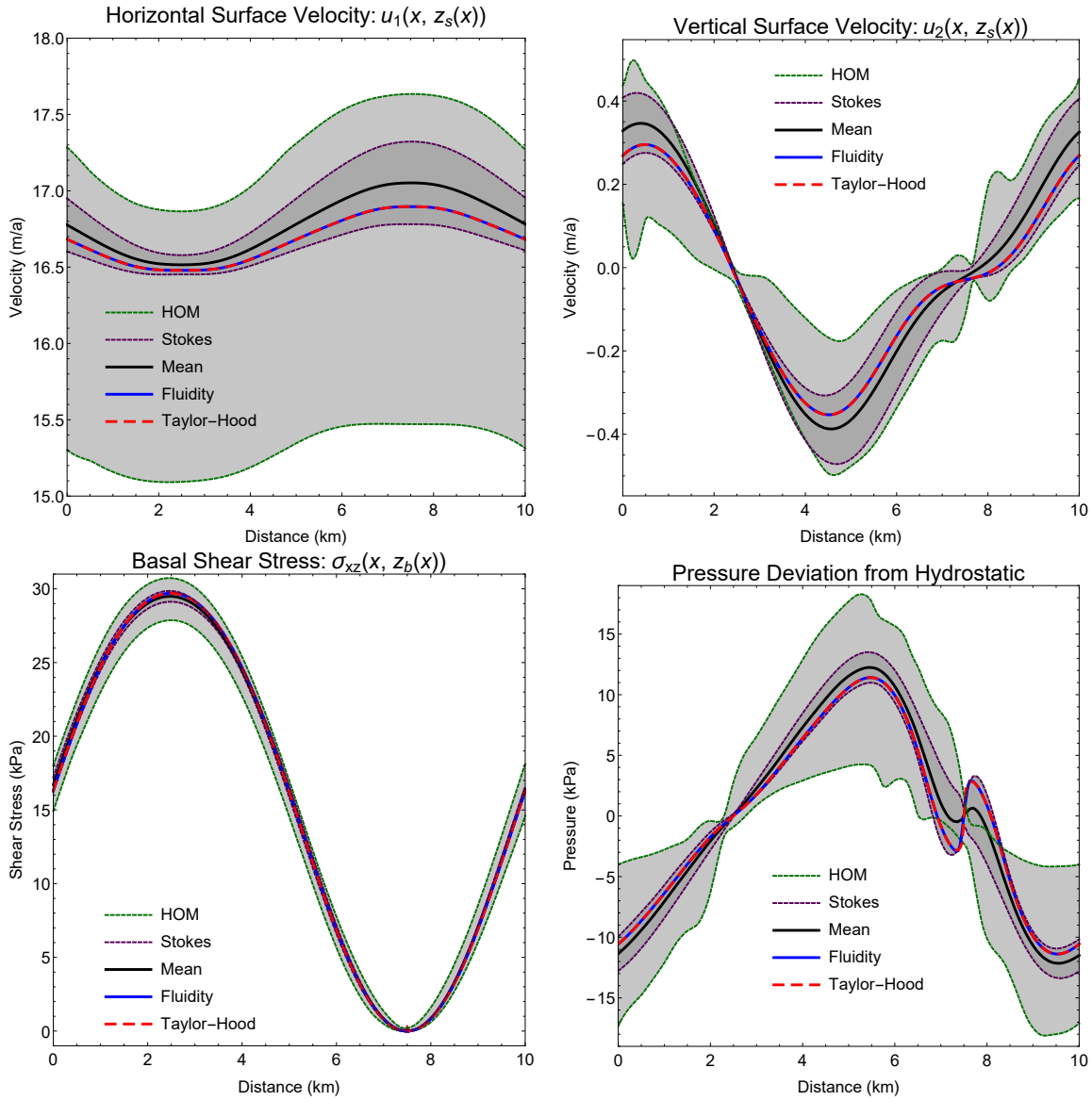

Figure 9.2: Various graphs of the augmented fluidity solution to benchmark D compared with other Stokes and higher order models. The light gray and gray bands represent one standard deviation of the higher order methods and full-Stokes models, respectively, with the average of the Stokes models represented as the black line. The solid blue line is the solution calculated using the augmented fluidity model. The dashed red line is a solution obtained by using a viscosity based Galerkin method with Taylor-Hood elements similar to [30].

One of the main points of interest from Figure 9.2 is that the augmented fluidity formulation

matches almost identically with the Galerkin method. Considering the wide spread of solutions, especially with regards to the horizontal surface velocity, the fact that the fluidity and Galerkin methods agree is good evidence that fluidity method is solving the problem accurately.

Another interesting feature shows up in the pressure deviation plot. Notice that the oscillating feature in the right side of that plot is not present in the higher-order models. This is probably due to the fact that these higher-order models reduce the complexity of the full-Stokes system by neglecting various strain rates. Apparently, these neglected strain rates are important in capturing the full behavior of the ice.

Next, $\log(\phi)$ on the surface is computed for both the augmented fluidity and Galerkin methods. This can be seen in Figure 9.3. Note that multiplying this plot by -1 results in a plot of $\log(\mu)$ to measure viscosity. Notice that the augmented fluidity method produces significantly smaller fluidities, which correspond to larger viscosities. The left peak is about 18 orders of magnitude smaller, and the right peak is about 17 order of magnitude smaller. What is more interesting is that the left peak of the Galerkin method appears to be capped at just under $\times 10^{-8}$. This spot corresponds to where β^2 is largest, which closely simulates a place where the bed is frozen.

As discussed in Section 8.2, s_{11} and s_{12} must be examined on the surface to get the full story as to why the fluidity-based formulation produces smaller fluidities. Recall that, in the fluidity-based formulation, s_{11} and s_{12} are primary dependent variables and are approximated in a discrete subspace of H^1. However, the only primary dependent variables of the Galerkin method are u_1, u_2, and p. This means, to calculate s_{11} or s_{12}, which is required to calculate fluidity, numerical derivatives of u_1, u_2 are taken. This will affect the accuracy of s_{11} or s_{12}. The FOSLS formulation will not have this problem.

Another useful feature of using a FOSLS formulation in which s_{11} and s_{12} are primary dependent variables is that they can be used directly in boundary conditions. For this problem, the no-stress boundary condition is $\hat{\underline{\underline{\sigma}}} \cdot \underline{n} = 0$. In the Galerkin method, this boundary condition is implicitly enforced [30]. However, when the domain is rotated so the top is horizontal as in Figure 9.1, this condition becomes $s_{11} + p = 0$ and $s_{12} = 0$. This means the FOSLS formulation

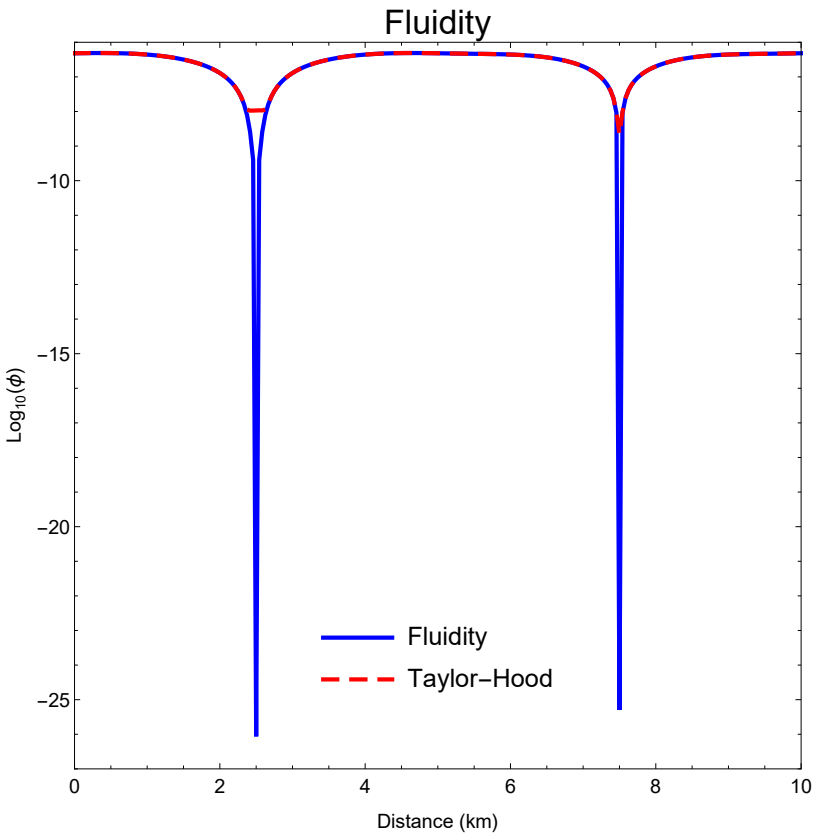

Figure 9.3: Fluidity at the surface as calculated using the augmented fluidity formulation (blue line) and a Galerkin method using Taylor-Hood elements (dashed red line).

can explicitly enforce $s_{12} = 0$ by building it into the finite element space.

Figure 9.4 show the values for s_{11} and s_{12} at the surface for both the fluidity-based and Galerkin methods. Now it is easier to see why the left peak of fluidity is stunted for the Galerkin method. Although both s_{11} and s_{12} cross zero for the Galerkin method, they are never both zero at the same location since $s_{12} = 0$ cannot be explicitly enforced. However, for the fluidity-based formulation $s_{11} = s_{12} = 0$ at two point in the domain since $s_{12} = 0$ is strictly enforced.

The last set of figures that examine the solution to this benchmark problem are the contour plots in Figure 9.5, which help to show where ϕ, ψ are small. Comparing with the benchmark B results in Figure 8.5, ϕ and ψ are generally a couple orders of magnitude smaller in benchmark D. This is most likely due to the fact that the ice is moving at an almost constant speed down the hill, which can be seen in the streamlines plot also in Figure 9.5. Like before, ϕ has two minima on the

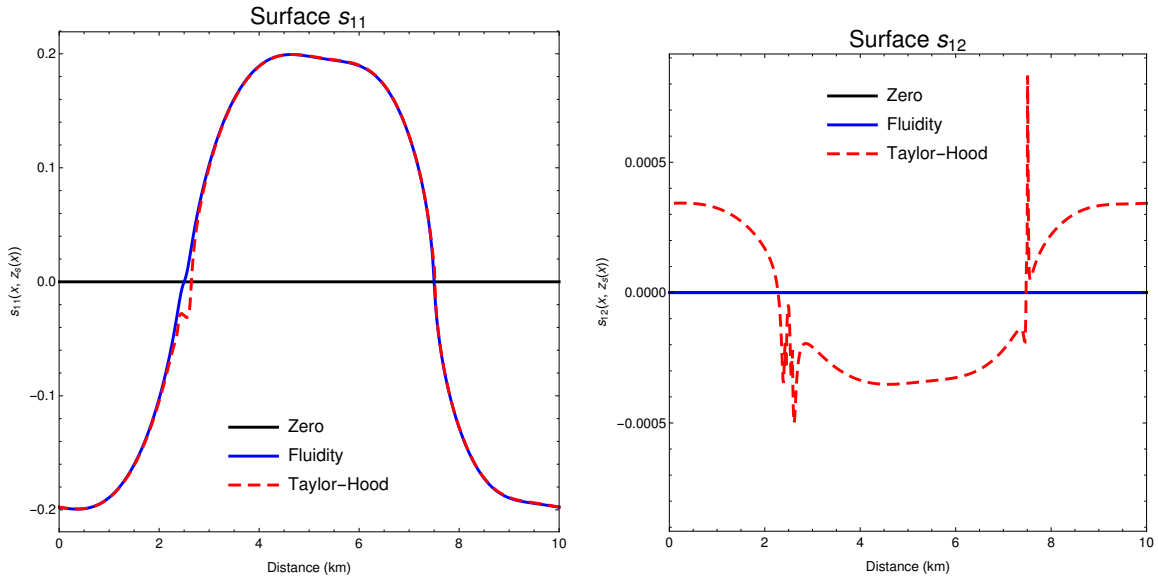

Figure 9.4: The two components of the deviatoric stress, s_{11} and s_{12}, evaluated at the surface as calculated using the augmented fluidity formulation (blue line) and a Galerkin method using Taylor-Hood elements (dashed red line).

surface, which now correspond to the maximum and minimum of β^2. Although it is hard to see in the streamline plot, the velocity is very slightly rotating around these points.

Another interesting feature of these contour plots is that both ϕ and ψ become very small near the bed where $\beta^2 = 0$. When $\beta^2 = 0$, the basal sliding boundary condition becomes $\underline{n} \cdot \underline{\underline{\sigma}} \cdot \underline{t} = 0$, which is equivalent to $s_{12} = 0$ since $n = [0, -1]$ and $t = [1, 0]$. Additionally, in the locations were β^2 is small, the glacier is almost experiencing pure translation. This can be seen in the streamlines plot. Pure translation will result in small stresses small as well as ω because these are all dependent on the rates of change of velocity. This type of situation is one reason why the fluidity-based formulations were developed.

9.3 Comparing Fluidity Formulations

This section compares the performance of both the basic and augmented fluidity formulations. In order to answer the questions posed at the end of Section 5.4, the next task is to examine how well the two FOSLS formulations perform given the various parameters for ψ and the scaling of

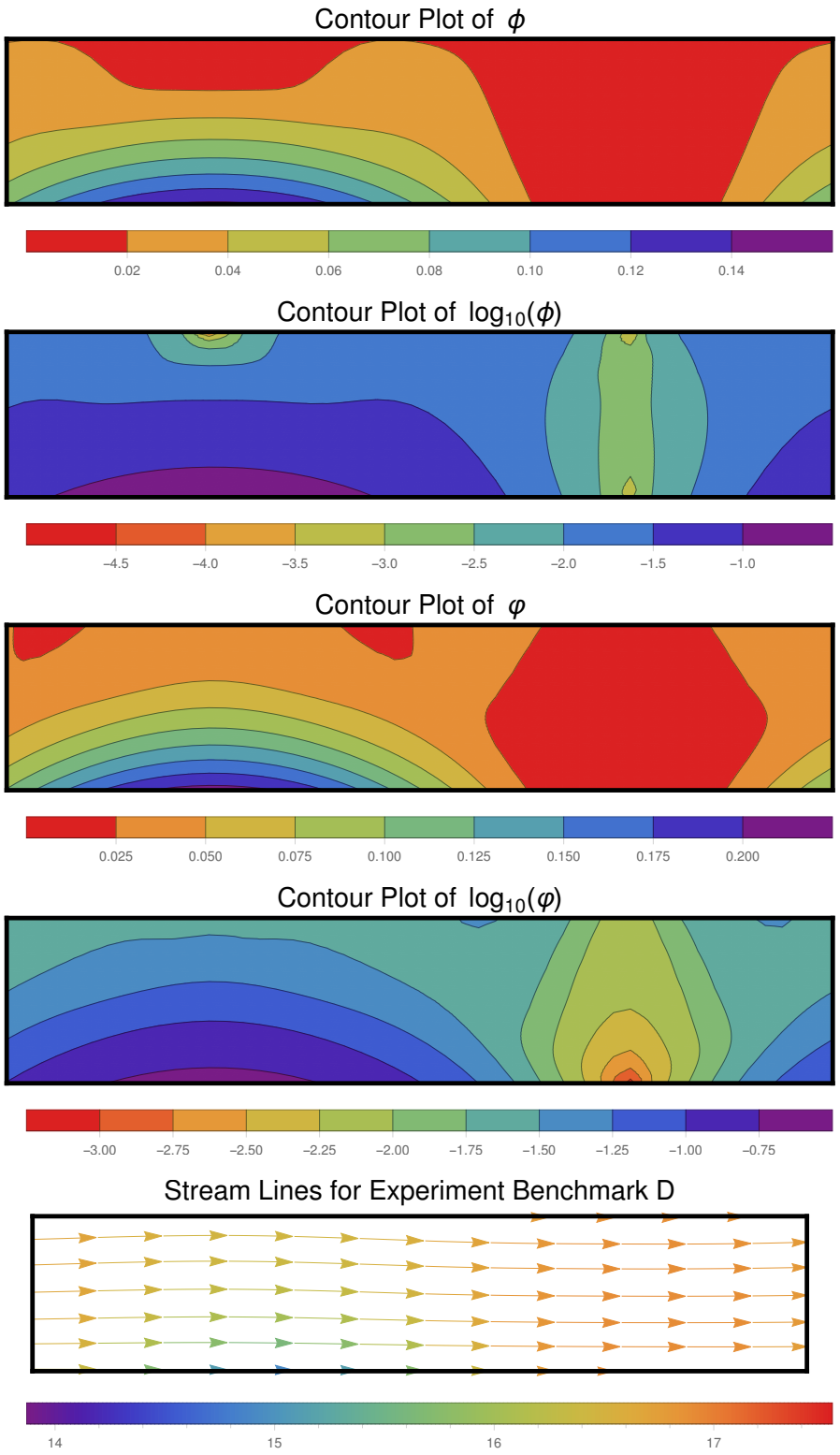

Figure 9.5: Contour plots of ϕ, $\log(\phi)$, ψ, $\log(\psi)$. The final plot show the streamlines for benchmark D.

the curl equation. Each of the following figures is organized in the following way. The figures are split into two plots based on the definition of ψ, where the left plot corresponds to using $\psi = 1/2\left(s_{11}{}^2 + s_{12}{}^2 + \omega^2\right)$ in Equations (5.4.15) and (5.4.16) and the right corresponds to $\psi = 1$. Each of these curves displays the effectiveness of a different scaling on the curl equations. Four different possible scalings are used, which, in order from strongest to weakest, are $\phi^{-1/2}$, $\psi^{-1/2}$, 1, and ϕ. Finally, there is one line that corresponds to solving the basic fluidity formulation in (5.4.2)-(5.4.6), which is independent of ψ and curl scaling.

The first set of plots examines the functional convergence, which is calculated by evaluating $||\mathcal{L}(\mathcal{U}) - f||$ on each gird level, where $\mathcal{L}$ represents the formulation applied to the unknowns, $\mathcal{U}$. Because quadratics are used for the finite-element space, the functional should reduce at a rate of $O(h^2)$. These results can be seen in Figure 9.6.

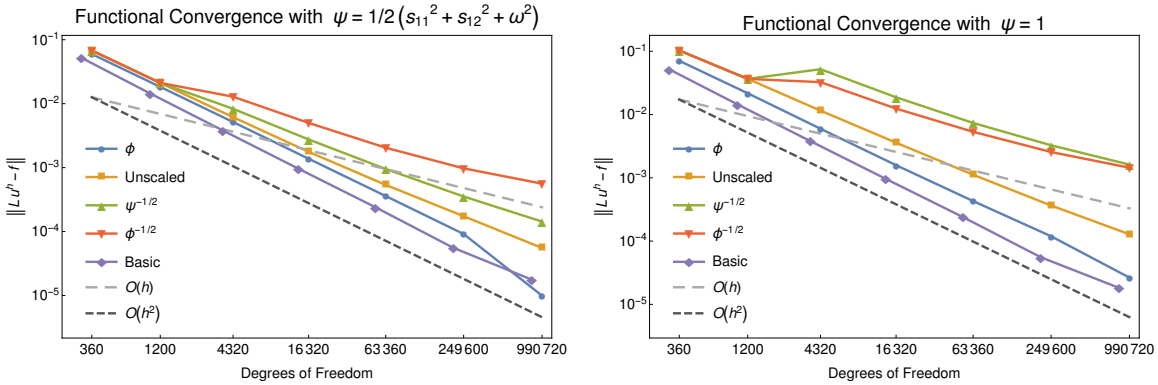

Figure 9.6: The functional norm convergence for $\psi = 1/2\left(s_{11}{}^2 + s_{12}{}^2 + \omega^2\right)$ (left) and $\psi = 1$ (right) with various scalings of the curl equations. For the case $\psi = 1$, the scaling $\psi^{-1/2}$ still uses the $1/2\left(s_{11}{}^2 + s_{12}{}^2 + \omega^2\right)$ definition for the scaling. The basic case refers to solving the system in (5.4.2)-(5.4.6).

It should be noted that Figure 9.6 should not be used to compare the relative size of the least-squares functional, since the functional for each test depend on the scaling. If, for instance, $\phi^{-1/2}$ is greater than one on a majority of the domain, the functional associated with that scaling will be necessarily larger than the unscaled test. Figure 9.6 should just be used to compare the relative convergence rates.

Notice that deemphasizing the locations where ϕ is small by scaling the curl equation by ϕ

lead to improved finite-element convergence. Additionally, the basic fluidity formulation, which is similar to scaling the curl equations by 0, performs similar to the ϕ scaling, both of which achieve $O(h^2)$ convergence. However, as the scaling on the curl equation increases, the finite-element convergence suffers. The idea behind scaling the curl equation is to improve AMG performance, which is discussed in the next set of plots.

The next set of plots, Figure 9.7, examines the performance of Conjugate Gradient (CG) preconditions with AMG on the various tests. Each one of these data points are found by taking the linear system from the final newton step on a grid level and solving it with a zero right hand side and random initial guess. The missing points are removed because they did not converge to a relative residual of 10×10^{-10} within 1000 iterations.

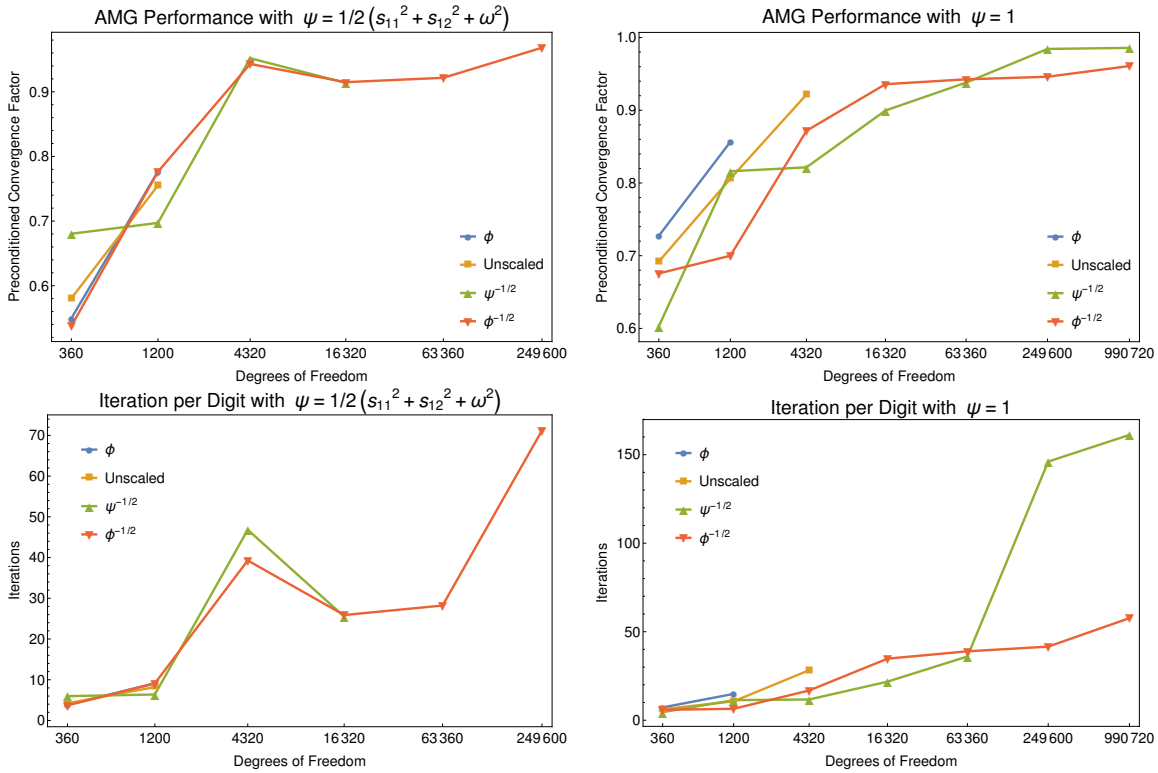

Figure 9.7: The CG preconditioned with AMG convergence factor (top) for $\psi = 1/2\left(s_{11}^2 + s_{12}^2 + \omega^2\right)$ (left) and $\psi = 1$ (right) with various scalings of the curl equations. The bottom graphs indicate how many iterations are required to reduce the functional by 0.1 at the given convergence factor. For the case $\psi = 1$, the scaling $\psi^{-1/2}$ still uses the $1/2\left(s_{11}^2 + s_{12}^2 + \omega^2\right)$ definition. Levels where AMG did not converge to a relative residual of 10×10^{-10} within 1000 iterations are removed.

When the curl equations are strongly scaled (i.e by $\psi^{-1/2}$ or $\phi^{-1/2}$), the AMG performance increased as seen in Figure 9.7. AMG performance is optimized by scaling the curl equations by $\phi^{-1/2}$. The performance is further increased by defining $\psi = 1$ leading to both of the strong scalings having bounded AMG convergence factors. Clearly, there is a trade off between AMG performance and finite-element convergence.

The final set of plots examines the accuracy of the solution by calculating $||u_1^f - u_1^r||$ on the surface of the ice sheet, where u_1^f is from the appropriate fluidity formulation and u_1^r is the reference solution from [30]. Most of the scaling test achieved a level of accuracy that is least as good as the solution from [30]. This can be seen in Figure 9.8. When the curl equations has a stronger scaling, the convergence rate of the L^2 approximation decreases.

The solutions for the unscaled system with $\psi = 1/2\left({s_{11}}^2 + {s_{12}}^2 + \omega^2\right)$ was used to generate the graphs in Figures 9.2-9.5 because it produced accurate and interesting solutions.

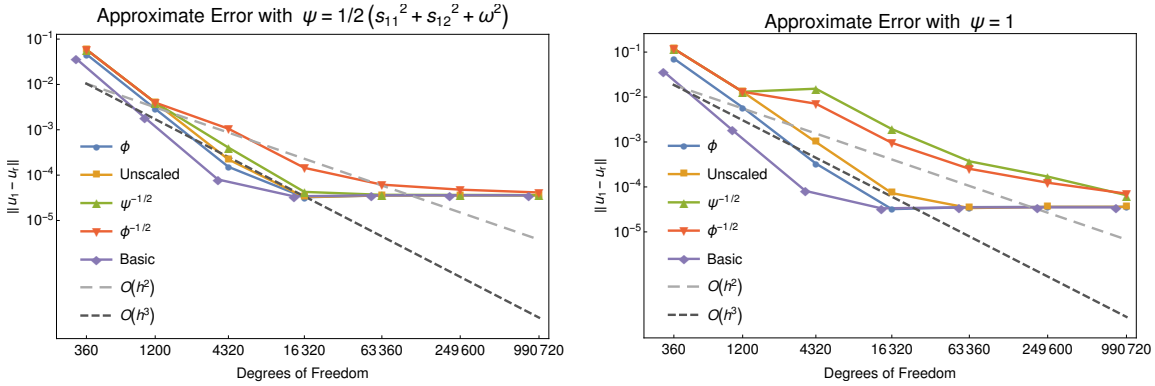

Figure 9.8: The L^2 convergence of the horizontal surface velocity, u_1, for $\psi = 1/2\left({s_{11}}^2 + {s_{12}}^2 + \omega^2\right)$ (left) and $\psi = 1$ (right) with various scalings of the curl equations. The solution provided in [30] is used as the reference, u_r. For the case $\psi = 1$, the scaling $\psi^{-1/2}$ still uses the $1/2\left({s_{11}}^2 + {s_{12}}^2 + \omega^2\right)$ definition only for the scaling. The basic case refers to solving the system in (5.4.2)-(5.4.6).

Based on the performance of both formulations on benchmarks B and D, as seen in Figures 8.7-8.9 as well as Figures 9.6-9.8, it can be concluded that the augmented fluidity formulation is not optimized for these problems. It is possible that there is a scaling on the curl equations thats optimizes the trade off between finite-element and AMG performance. However, a possibly better avenue of research is to find a efficient iterative solver for the basic fluidity formulation. This is

the topic of future work. The following test problems will only be solved using the basic fluidity formulation.

Chapter 10

ISMIP: Benchmark E

The chapter discusses another benchmark problem. This time the domain for the problem is taken from an real-world glacier. Additionally, this benchmark is slit into two experiments: one with pure no-slip basal boundary conditions and one with a small patch with basal sliding.

10.1 Problem Setup

The next ISMIP benchmark problem considered by this paper is benchmark E. In benchmark E, a central flow-line from the Haut Glacier d'Arolla in the European Alps is used as the domain and is depicted in Figure 10.1. The data used to generate this domain is archived on `http://homepages.ulb.ac.be/~fpattyn/ismip/`. Benchmark E consists of two experiments that have different boundary conditions on the bed of the ice sheet.

For this benchmark, the domain is generated by using quartic spline that exactly interpolates the data points. Also, the domain is first scaled from meters to kilometers and then the x coordinate is scaled by an additional 5 to make it so that $x \in [0, 1]$. A new derivative, $\frac{1}{5}\frac{\partial}{\partial x}$, is used to compensate for the second scaling. A full list of parameters is found in Table 10.1.

The boundary conditions for this problem are a bit special since there are two test cases. In both cases, the surface boundary conditions is the usual no-stress condition. However, the basal boundary conditions are different for each experiment. The first experiment has a no-slip basal boundary condition. The second experiment has a slippery patch where β^2 from Equation 9.1.1 equal zero when $2200 \leq x \leq 2500$ m. The summary of the boundary conditions for both experiments

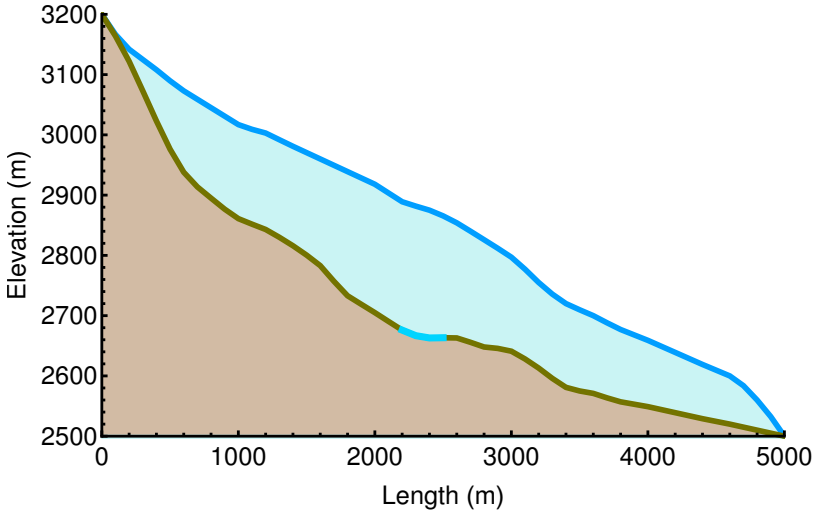

Figure 10.1: A cross section domain of the Haut Glacier d'Arolla used in benchmark E. The blue patch on the bed indicates where the basal sliding condition is applied in the second experiment.

Table 10.1: Parameters used in the benchmark E

Parameter	Value	Units
A	10^{-16}	$\mathrm{Pa}^{-3}\ \mathrm{a}^{-1}$
$\lvert g\rvert$	9.81	$\mathrm{m/s}^2$
ρ	910	$\mathrm{kg/m}^3$
w	$2\pi/L$	
n	3	
Seconds per year	31,556,926	s/a

is found in Table 10.2.

Table 10.2: Boundary conditions for benchmark E

	Bed			Surface		
Experiment 1	$\underline{u}$	$=$	$0 \quad x \in [0, 5000]$	$\hat{\underline{\underline{\sigma}}} \cdot \underline{n}$	$=$	0
Experiment 2	$\underline{u} \cdot \underline{n}$	$=$	0	$\hat{\underline{\underline{\sigma}}} \cdot \underline{n}$	$=$	0
	$\underline{n} \cdot \hat{\underline{\underline{\sigma}}} \cdot \underline{t}$	$=$	$0 \quad x \in [2200, 2500]$			
	$\underline{u}$	$=$	$0 \quad$ Otherwise			

10.2 Numerical Solution Results

Sections 8.2 and 9.2 showed that the basic fluidity formulation, represented by equations (5.4.2)-(5.4.6), is more reliable in terms of finite element convergence and convergence to an approximate solution. For this reason, it is the formulation used to solve the experiments in benchmark E. The resulting solution is compared with the database of other models and the Taylor-Hood model from from Section 5.1. From Figures 10.2 and 10.3, it is clear to see that the basic fluidity solution agrees well with the other compiled solutions for both experiments.

The largest discrepancy between the database and the basic fluidity formulation solution occurred in the basal shear stress and pressure deviation plots for experiment 2 seen in Figure 10.3. Recall that Experiment two involves a sharp transition from a no-slip boundary condition to a no-stress boundary condition. This sudden change cause a singularity in the derivative of the solutions resulting in poorer convergence. The effects of this singularity are seen throughout the entirety of experiment 2.

Once again, Figure 10.4 shows that a fluidity-based formulation recovers larger viscosity (smaller fluidities) than the Taylor-Hood method. Additionally, the fluidity formulation recovers several peaks that are not resolved by the Taylor-Hood method. This is particularly true around 1 km, between 2 km and 3 km, and 4.5 km. Unfortunately, without an exact solution, it is impossible to know which fluidity profile is more physically correct.

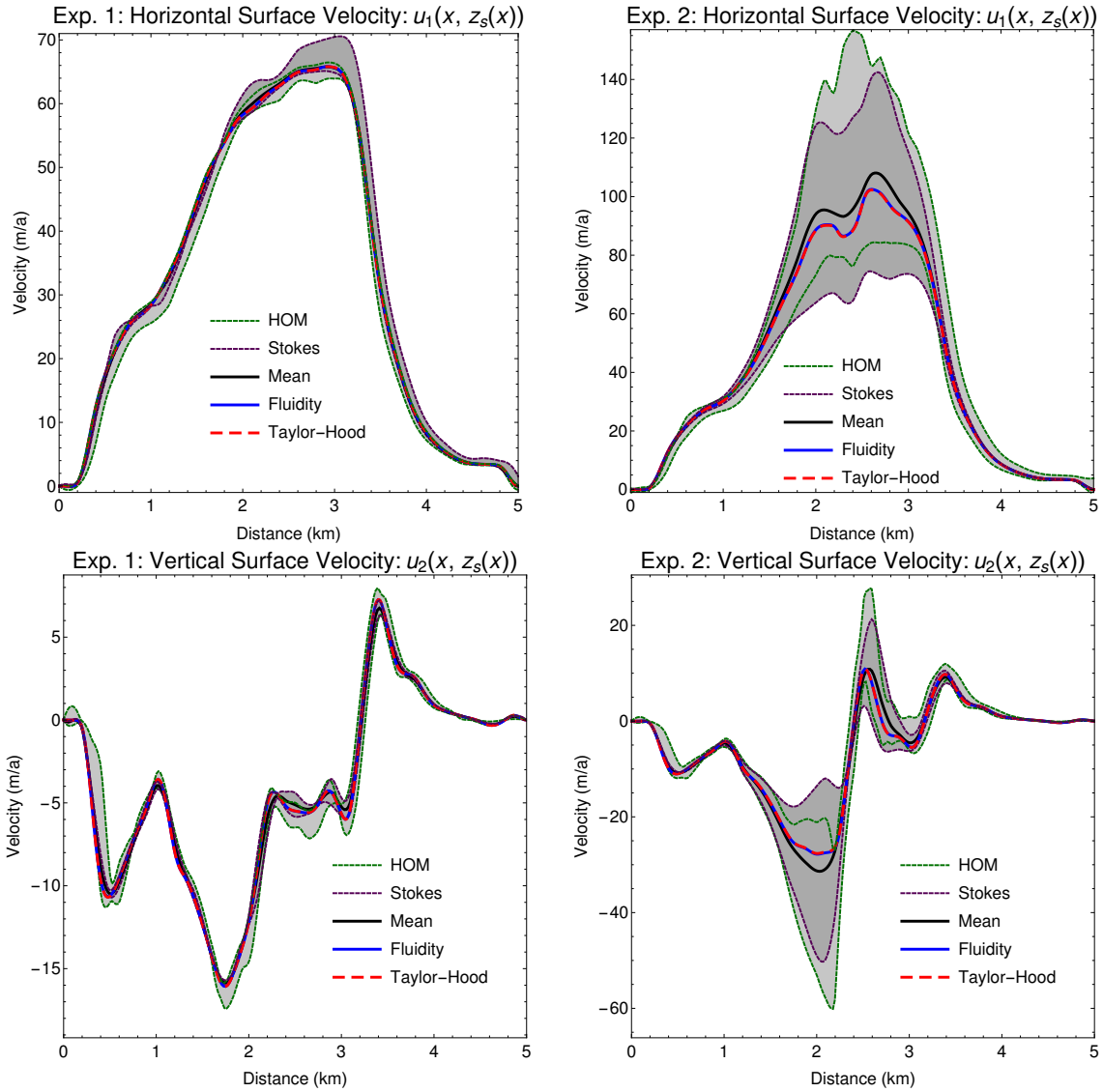

Figure 10.2: Surface velocity plots from the basic fluidity solution to benchmark E compared with other Stokes and higher order models. The light gray and gray bands represent one standard deviation of the higher order methods and full-Stokes models, respectively, with the average of the Stokes models represented as the gray line. The solid blue line is the solution calculated using the basic fluidity model. The dashed red line is a solution obtained by using a viscosity based Galerkin method with Taylor-Hood elements as described in [30]. Experiment 1 is on the left and experiment 2 is on the right.

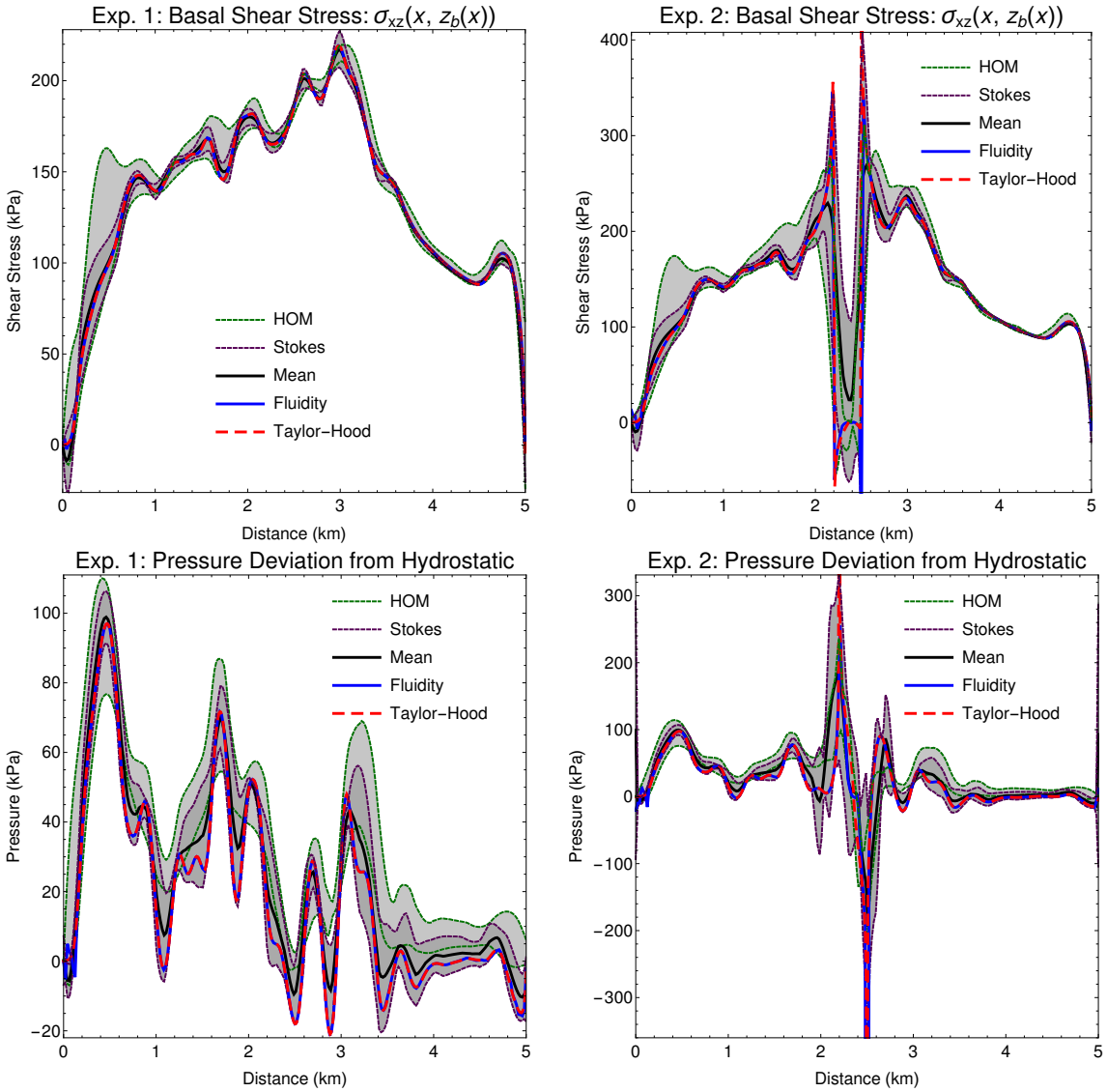

Figure 10.3: Basal sheer stress and pressure deviation from the basic fluidity solution to benchmark E compared with other Stokes and higher order models. The light gray and gray bands represent one standard deviation of the higher order methods and full-Stokes models, respectively, with the average of the Stokes models represented as the gray line. The solid blue line is the solution calculated using the fluidity model. The dashed red line is a solution obtained by using a viscosity based Galerkin method with Taylor-Hood elements as described in [30]. Experiment 1 is on the left and experiment 2 is on the right.

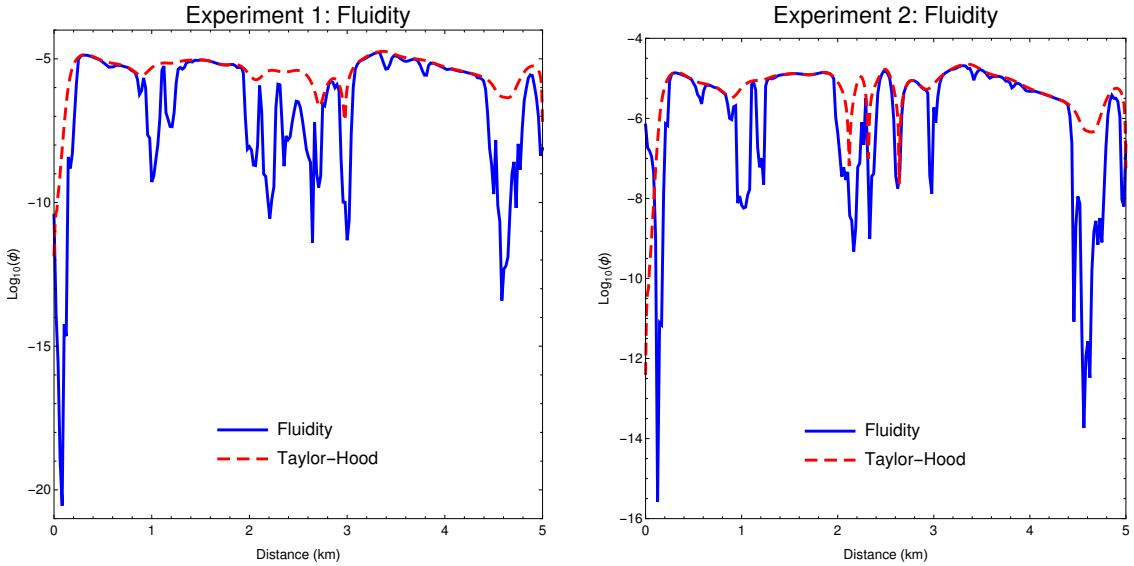

Figure 10.4: Fluidity at the surface as calculated by the fluidity formulation (blue line) and a Galerkin method using Taylor-Hood elements (dashed line). Experiment 1 is on the left and experiment 2 is on the right.

As in Sections 8.2 and 9.2, the surface stresses are examined to glean more information about the smaller fluidities. Figure 10.5 shows s_{11} and s_{12} evaluated at the surface of the domain for both experiments approximated using either the basic fluidity formulation or the Galerkin method. Unlike benchmark D, $s_{12} = 0$ is not explicitly enforced in the basic fluidity formulation since the surface is not a horizontal line. This means the fluidity peaks do not result from simply when s_{11} changes signs. Now both s_{11} and s_{12} need to be near zero at the same locations. From Figure 10.5 it is easy to see that this occurs more frequently with the basic fluidity method than the Galerkin method. Once again, this is due to the fact that s_{11} and s_{12} are primary dependent variables and are, therefore, approximated more accurately. This is just another benefit of a FOSLS formulation.

The next set of plots, found in Figure 10.6, describe the velocities through the entire glacier. The main point of interest from these graphs is in the horizontal velocity plot for experiment 2. Near the basal sliding boundary conditions, the ice rapidly accelerates to an almost uniform speed. This results in a "pile up" of ice just after the basal sliding boundary and an "absence" of ice just before this section. This is supported by the large negative vertical velocities of the ice filling in the void just before the basal sliding boundary. Additionally, the positive vertical velocities just after the sliding boundary indicate that the faster ice is traveling up and over the slower ice. This entire story can be seen in the stream line plots.

The experiment 1 velocity are pretty tame, when compared with experiment 2. The ice simply travels from top to bottom while following the shape of the basal boundary, more or less. Without the existence of any accumulation of snow fall on the upper half, this glacier would eventually just mostly drain out the right side.

Since only the basic fluidity system was solved, ψ could not be calculated for this experiment. The contour plots of ϕ and $\log(\phi)$ can be found in Figure 10.7. One interesting aspect of these plots was that the fluidity in experiment 1, is relatively large, when compared with the other benchmarks, near the bed at about the 3 km mark. This means that the stress in the region are larger, which would cause the ice to warm up. Since, this place is relatively flat/concave up, it is possible that liquid water would collect in this region from the warmer ice. This explain why placing the slippery

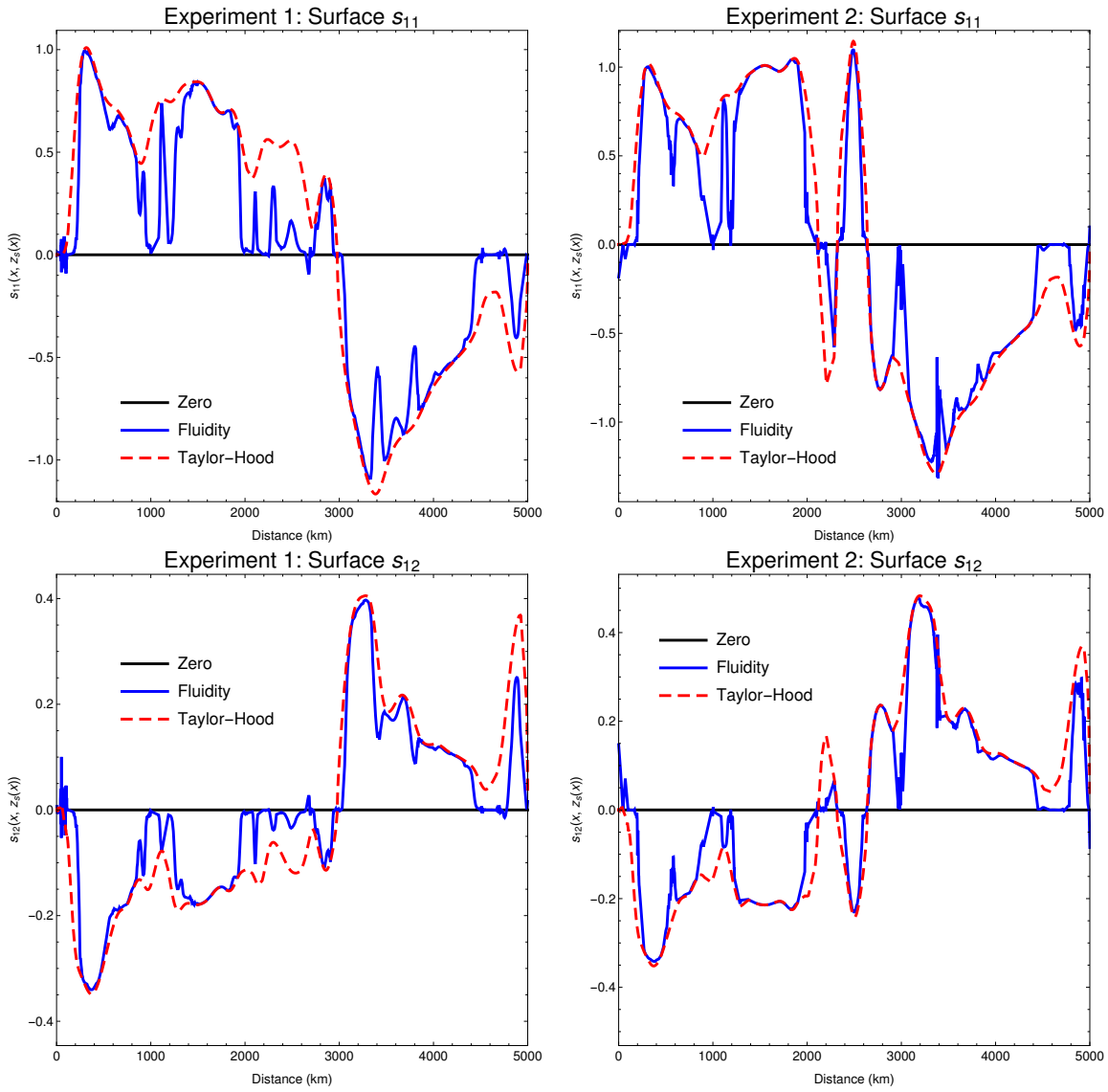

Figure 10.5: The two components of the deviatoric stress, s_{11} and s_{12}, evaluated at the surface as calculated using the augmented fluidity formulation (blue line) and a Galerkin method using Taylor-Hood elements (dashed red line). Experiment 1 is on the left and experiment 2 is on the right.

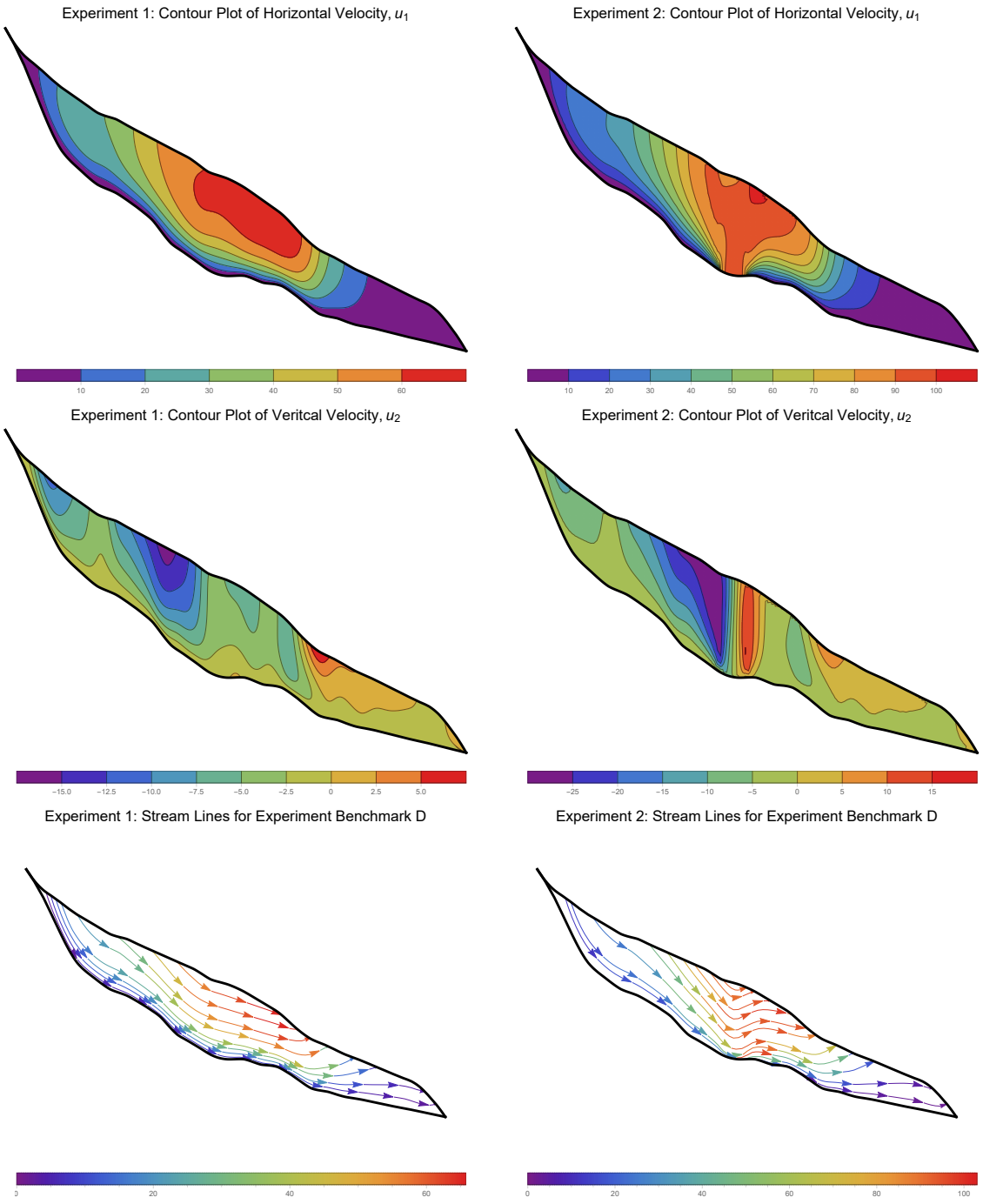

Figure 10.6: Contour plots of u_1, u_2, for both experiment 1 (left) and 2 (right). The final plot show the streamlines for experiment benchmark E

patch between 2.2-2.5 km makes sense.

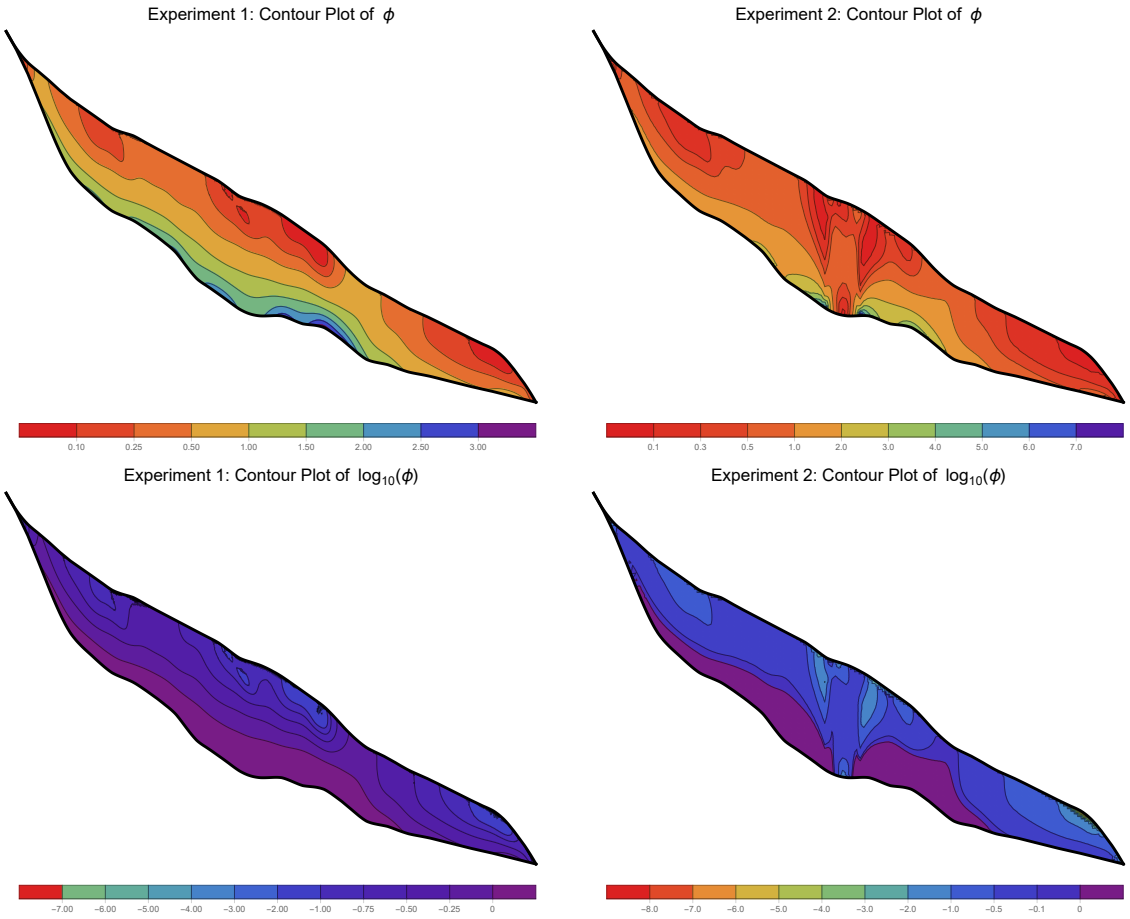

Figure 10.7: Contour plots of ϕ, $\log(\phi)$, for both experiment 1 (left) and 2 (right).

10.3 Performance Comparison

This benchmark is solved with two different types of refinement. The first is a simple global uniform refinement, and the second is local adaptive refinement using a threshold strategy [2], in which the element containing the largest error are refined first, until 50% of the total error is contained in the refined region. The local error is estimated by the FOSLS functional. The last level of refinement for the threshold method is a global uniform refinement. This is done to save time while still resulting in solutions that have approximately the same number of degrees of freedom.

The finite element converges of these two refinement methods is found in Figure 10.8. In the

case of experiment 1, the uniform refinement has a convergence rate of less than $O(h)$ with the final rate being about $O(h^{\frac{1}{2}})$. Refining with the threshold method increases this to about $O(h^{1.3})$.

Experiment 2 has more interesting behavior. Uniform refinement results in an abysmal rate, $\sim O(h^{0.25})$, for the finite-element convergence. This is due to the singularity caused by the instant switch between no-slip and no-stress boundary conditions on the bed. There are a few ways to deal with this type of singularity. The most obvious solution is to make the switch between the two boundary conditions smoother. This can be achieved by rewriting the basal sliding boundary condition as follows:

$$\underline{n} \cdot \underline{\underline{\sigma}} = \beta^2 \underline{u} \Rightarrow \alpha^2 \underline{n} \cdot \underline{\underline{\sigma}} = \underline{u},$$

where $\alpha^2 = \beta^{-2}$. Then smoothly transitioning α from 0 for a no-slip boundary to very large for the sliding boundary.

If the problem needs to be solved with the sharp transition between boundary conditions, there are a few ways to deal with this. One way would be to unweighted the functional around the singularities at 2.2 km and 2.5 km. This would result in increased finite element convergence, but reduced accuracy near those points. Another method would be to build the singularity into the finite element space, but this is outside the scope of this thesis. However, neither of these solutions are employed in this paper. Instead, the threshold refinement method is used to create a graded mesh around the singularity.

From Figure 10.8, it is easy to see that the threshold method for experiment 2 produced optimal finite element convergence of $O(h^2)$. However, immediately returning to a uniform refinement step in the last iteration reduces the convergence rate down to $O(h^{0.5})$. It is clear that a graded mesh must constantly be used to resolve the singularities introduced by the abrupt change between no-slip and basal sliding boundary conditions. This is another reason why a smoother transition between boundary conditions is the preferred way to avoid the singularities.

The next set of graphs in Figure 10.9 shows the convergence to the approximate solution found by solving the Taylor-Hood method with approximately one million degrees of freedom. These

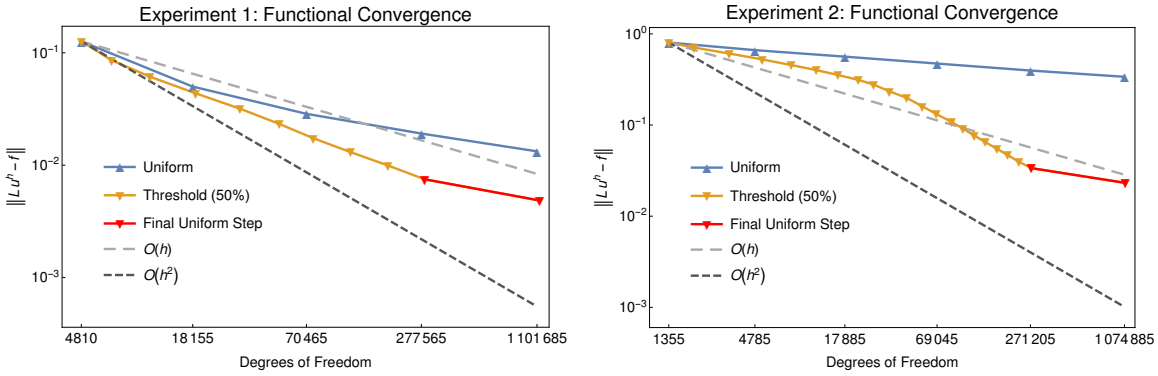

Figure 10.8: The functional norm convergence for experiment 1 (left) and and experiment 2 (right) with either uniform or threshold based mesh refinement. All tests use the basic fluidity formulation, (5.4.2)-(5.4.6), with quadratic elements.

convergence rates represent the minimum convergence rate between the basic fluidity formulation and the Taylor-Hood method to the true solution. Let u^* be the true solution and u^f, u^m be the approximate solutions from the fluidity and mixed methods that are converging to u^*. If $u^m \to u^*$ faster than $u^f \to u^*$, then u^m converges to u^* first and the convergence rate as $u^f \to u^m$ will be no larger than $u^f \to u^*$.

It is clear that the threshold refinement helps increase the rate of convergence resulting in almost an order of magnitude difference in the approximate error between the threshold and uniform solutions for experiment 1 and almost two orders of magnitude for experiment two. In the L^2 convergence plot, Figure 10.9, for experiment 2, the approximate error starts to increase. This is probably due to the fact that this comparison is between two approximate solutions and not a true solution.

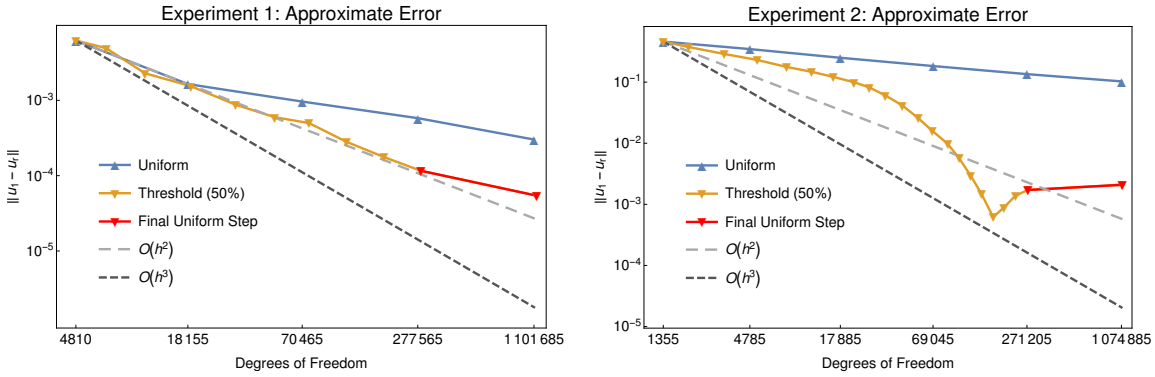

Figure 10.9: The L^2 convergence of the horizontal surface velocity, u_1, for experiment 1 (left) and experiment 2 (right) with either uniform or threshold mesh refinement. These error were found by comparing with the Taylor-Hood method. All test solved the basic fluidity formulation, (5.4.2)-(5.4.6), with quadratic elements.

Finally, Figure 10.10 shows a progression of adaptively refined meshes for experiments 1 and 2. In experiment 1, most of the refinement occurs near the border. Less refinement occurs where ϕ is smaller. This is probably due to the fact that the refinement is based on where the functional is large. Since a smaller ϕ results in a smaller functional, the threshold method might artificially ignore these locations.

In experiment 2, most of the refinement occurs near the two singularities. This is completely

expected since this will be where the largest errors occur. However, after enough levels of refinement, refinement starts to occur near the surface around the same places as seen in experiment 1.

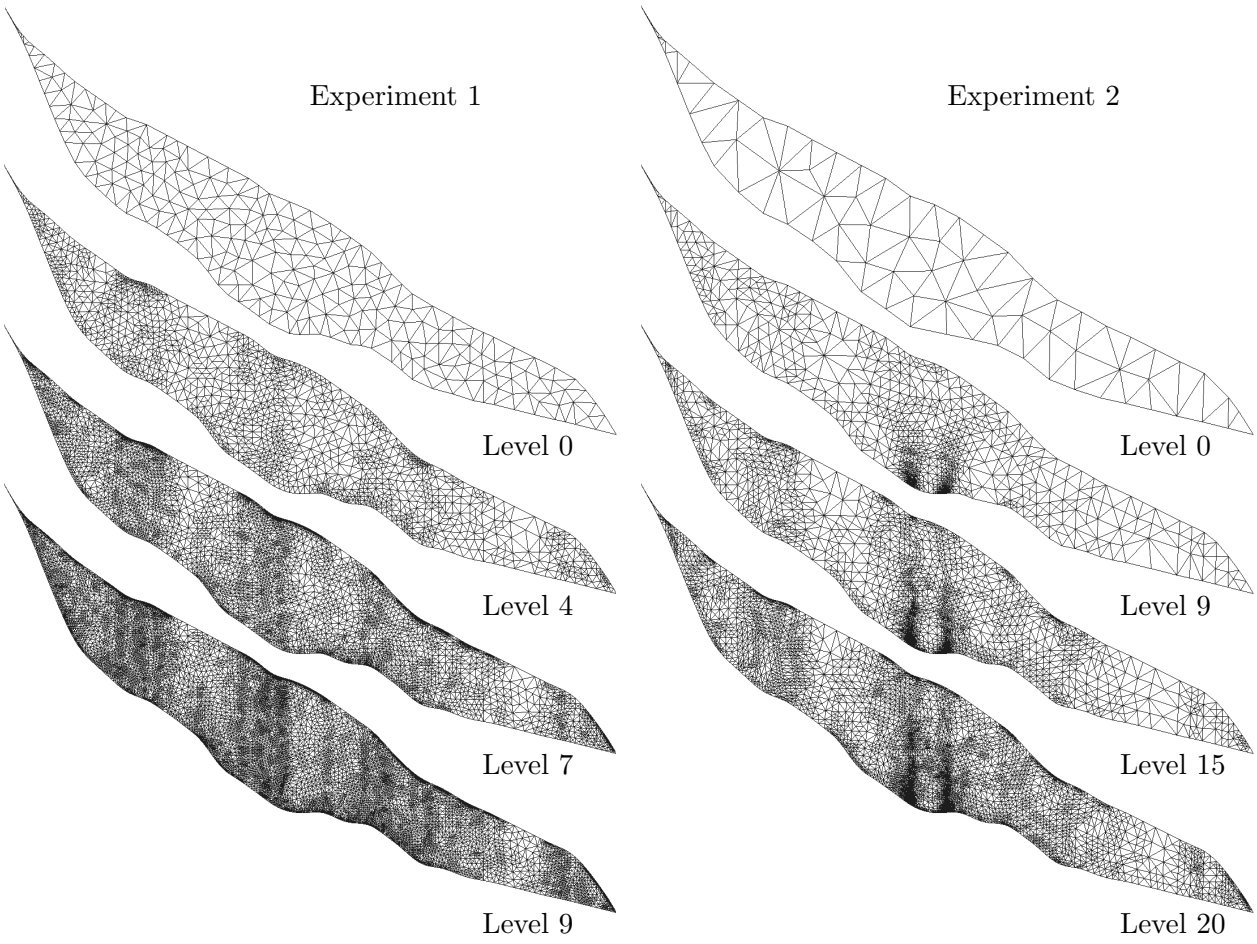

Figure 10.10: A few meshes from experiment 1 (left) and experiment 2 (right). The experiment 1 meshes are from levels 0, 4, 7, 9 with 4,810, 31,895, 119,240, and 288,380 degrees of freedom, respectively. The experiment 2 meshes are from levels 0, 9, 15, 20 with 1,355, 34,290, 119,055, 274,195 degrees of freedom, respectively.

Chapter 11

Time Dependant Domain

The chapter discusses the final test problem. This problem involve a mostly rectangular domain with a Gaussian bump on the bed. The free surface is allowed to evolve over time until the system reaches steady state.

11.1 Problem Setup

The last test problem is a variation on ISMIP benchmark F. Benchmark F is a rectangular glacier where the bed is perturbed by a Gaussian bump. Additionally, the free surface of the ice sheet is allowed to evolve over time. There are two main differences between benchmark F and the test problem presented here. First, the test problem in this paper is adapted for 2-D methods. Second, viscosity is nonlinear with $n = 3$ in Glen's flow law, (2.2.7) as opposed to the linear viscosity in benchmark F. The domain is defined by

$$z_s = -\tan(\theta)x$$

for the surface and

$$z_b = z_s - H + a_0 e^{\frac{-x^2}{{\sigma_0}^2}}$$

for the bed. The domain for this problem is found in Figure 11.1. Notice the bump a the bottom near the middle of the domain.

The other parameters in this test problem are chosen to match the spirit of benchmark F. For instance, benchmark F is designed so that the surface velocity of the rectangular glacier without

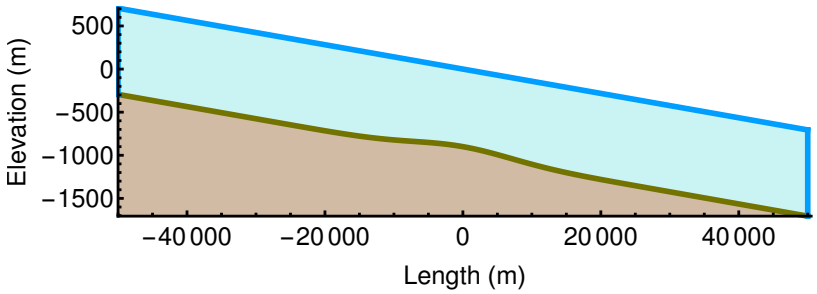

Figure 11.1: The domain for the time dependent test problem.

the Gaussian bump would be 100 m a^{-1}. The modified problem uses a flow law parameter, A, and average bed slope, θ such this surface velocity constraint is met. The full list of parameters is found in Table 11.1.

Table 11.1: Parameters used in the time dependent test problem

Parameter	Value	Units
A	10^{-16}	$Pa^{-3}\ a^{-1}$
$\|g\|$	9.81	m/s^2
ρ	910	kg/m^3
$\hat{H}$	1	km
$\hat{L}$	100	km
a_0	100	m
σ_0	10000	m
θ	0.809°	
n	3	
Seconds per year	31,556,926	s/a

The boundary conditions for this problem are very simple. On the surface a no-stress condition is used. The bed has a no-slip condition. Finally, the left and right sides are periodic. These are the same boundary conditions for the rectangular test problem in Section 7.1 summarized in Table 7.2.

The free surface is evolved using the kinematic relationship for ice sheets in 2-D,

$$\frac{\partial z_s}{\partial t} + u_1 \frac{\partial z_s}{\partial x} - u_2 = b, \tag{11.1.1}$$

where b is the surface mass balance [22]. For this test problem, the surface mass balance is zero.

11.2 Numerical Solution Results

As with benchmark E, this test problem is solved with a NI-Newton-FOSLS approach using the basic fluidity formulation. Forward Euler is used to update the surface with a time step of 0.5 years. At each time step, the maximum change in the surface between the previous and current time step is recorded. This value is simply referred to as surface change and is used as a stopping criteria for the simulation. Since the surface mass balance is zero, the free surface should slowly reach a steady state solution and the surface change should always decrease. The simulation runs for 250 years or until the surface change start to grow, indicating an instability in the time stepping method. Figure 11.2 shows the value of the surface change over time for both the basic fluidity formulation and the Taylor-Hood method. Notice that both methods decrease at the same rate for almost 100 years. After that, the Taylor-Hood method becomes unstable.

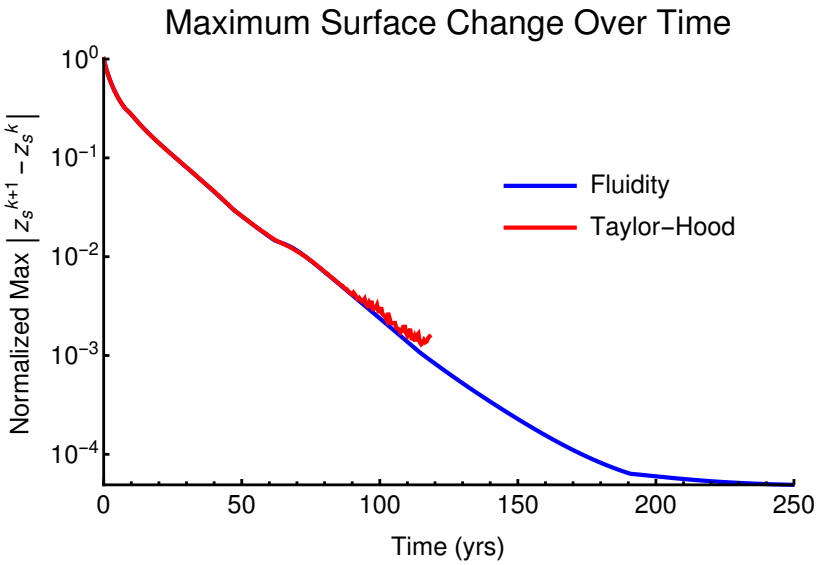

Figure 11.2: A plot of how the free surface changes over time. Let z_s^k be the free surface at time iteration k.

The surface elevation, horizontal velocity, and vertical velocity are found in Figure 11.3. Each plot shows its respective quantity of interest at various time snapshots. This way it is easier to see how the solution evolved over time as it approaches steady state. The surface elevation plot is rotated to remove the rather large linear component due to the slope of the ice sheet.

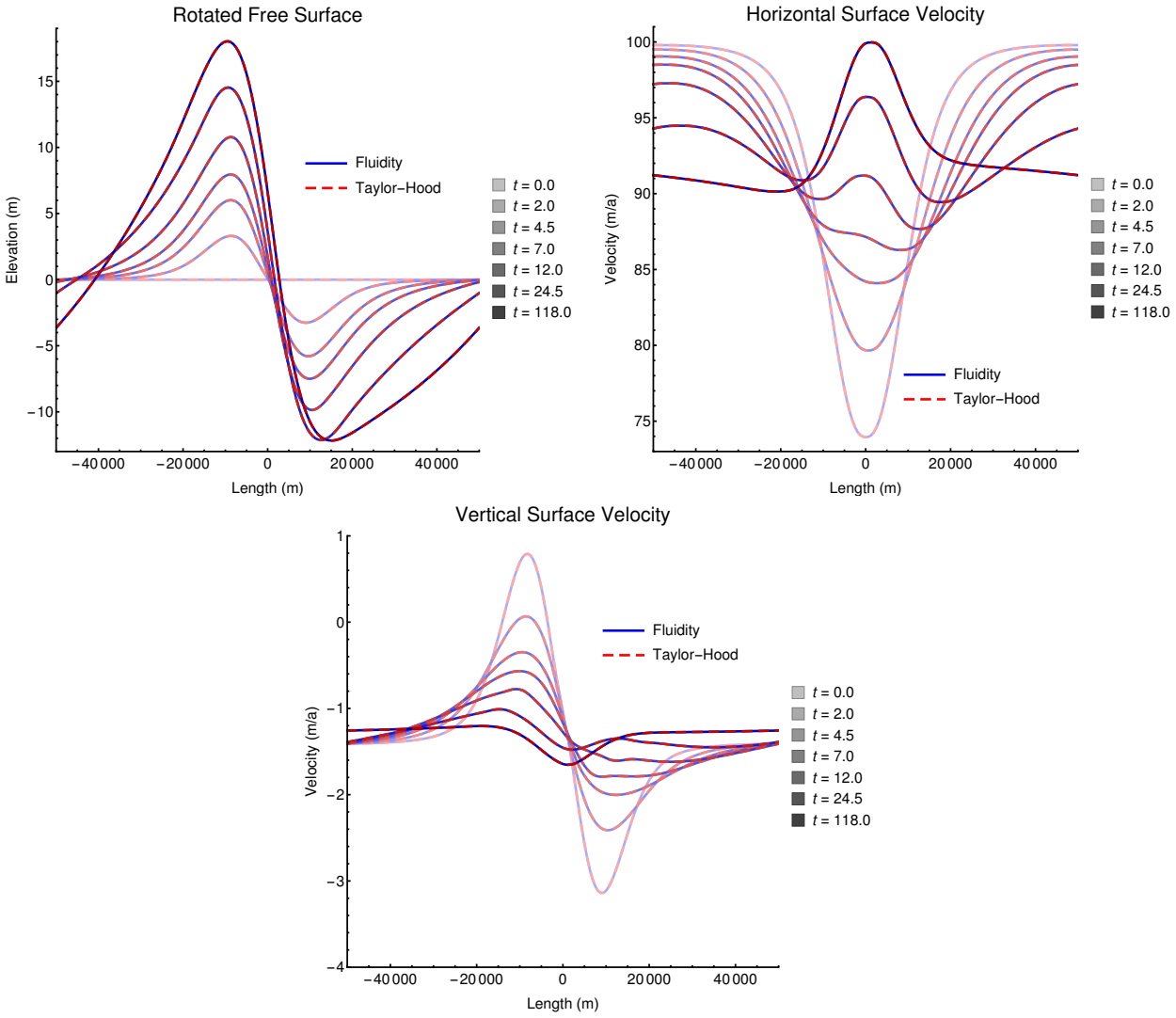

Figure 11.3: Plots of surface elevation, horizontal velocity, and vertical velocity. The blue line is the solution from the basic fluidity formulation and the dashed red line is from the Taylor-Hood method. The opacity of the lines, corresponding legend on the right, refers to what year the solution is from, where the darker gray corresponds to a more opaque line.

Most of the interesting dynamics happen in the surface fluidity plots found in Figure 11.4. Initially there are only two peaks in the fluidity. One of them is directly above the Gaussian bump, and the other occurs at the periodic boundary. To simplify referring to these peaks, name them the g-peak and p-peak, respectively as seen in subplot (a). Over time, the g-peak splits into a triplet, three peaks, and the left peak travels upstream and the right peak travels downstream, which is represented in subplot (b). The p-peak briefly travels downstream, and then travels upstream to eventually coalesce with the right peak from the triplet and finally diminishes, depicted in subplot (c). Finally, the system reaches steady state in subplot (d).

For the most part, the fluidity formulation captures smaller fluidities around the peaks. The Taylor-Hood method does not resolve the fluidity well when the coalescence mentioned above occurs. It should be noted that the grid remained constant throughout time. This lead to an interesting observation. As the peaks moved, they eventually cross a grid point. When the peak and the grid point are perfectly aligned, the fluidity is minimized, but the fluidity formation always has smaller values than the Taylor-Hood method. Since, both the fluidity and Taylor-Hood methods use the same number of surface grid points, it can be concluded that the discrepancy between the two methods is not due to the influence of the grid.

Figure 11.5 contains contour plots for the horizontal and vertical velocities as well as streamlines for the beginning of the simulation, $t = 0$ years, and the end of the simulation, $t = 250$ year. Notice the shape of the stream lines before and after the simulation. Near the surface, the stream lines exit and reenter the domain. The coincides with the fact that the vertical velocities are positive to the left and negative to the right of the bump. This is what leads to the build up of ice before the bump and the thinning of the ice just after the bump at the end of the simulation. After the simulation is complete, the streamlines are parallel to the surface, which is why this is the steady-state solution.

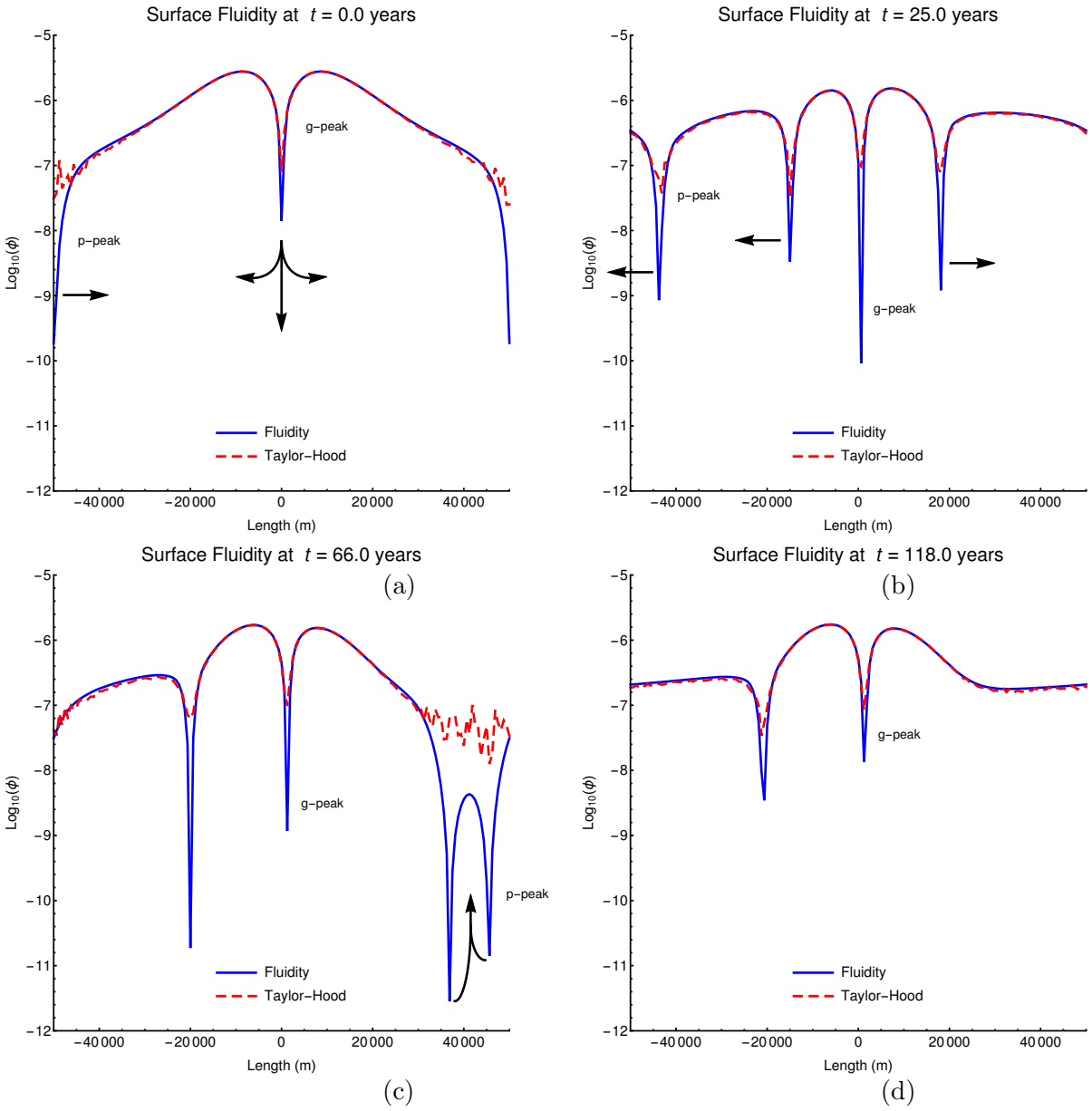

Figure 11.4: A series of plots that shows the fluidity at the surface at different times in the simulation. The blue line is the solution from the basic fluidity formulation and the dashed red line is from the Taylor-Hood method. The black arrows indicate how the direction the peak will travel.

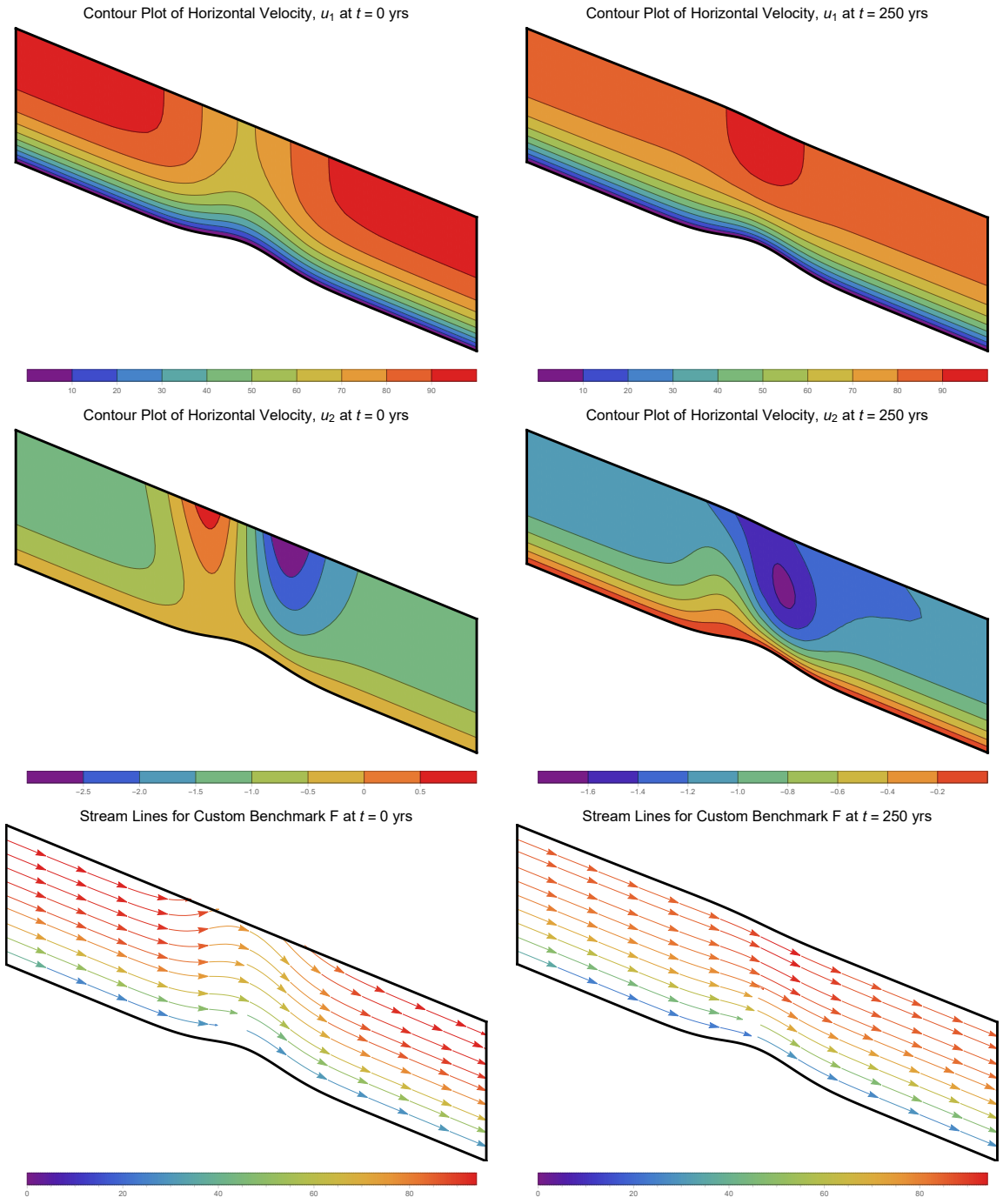

Figure 11.5: Contour plots of u_1, u_2, at year 0 (left) and at year 250 (right). The final plot show the streamlines.

The last set of plots, found in Figure 11.6, presents the contour plots for ϕ and $\log(\phi)$ before and after the simulation. Regardless of the simulated year, the majority of the ice sheet experiences nearly the same fluidity resulting in a rather smooth fluidity profile throughout the whole domain. The only places where the fluidity goes to zero is near the surface as discussed in Figure 11.4.

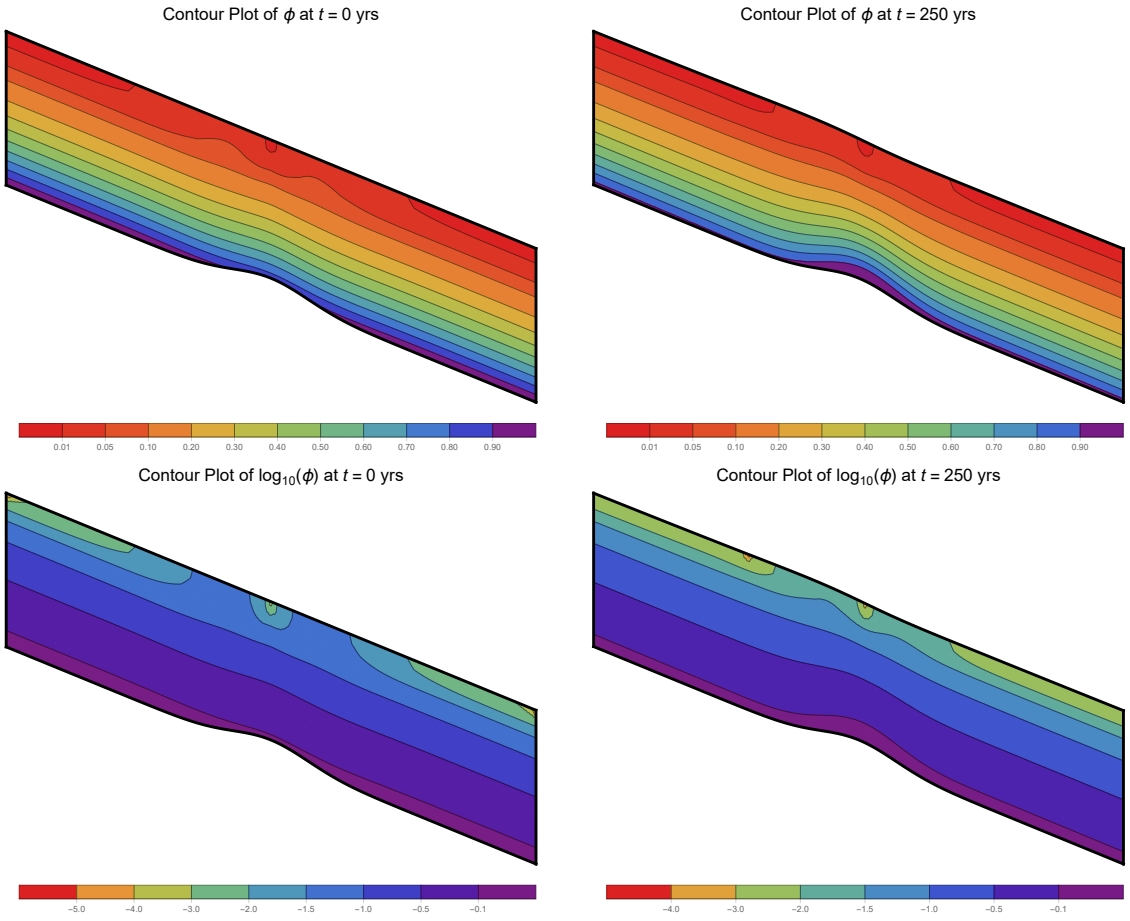

Figure 11.6: Contour plots of ϕ, $\log(\phi)$, at year 0 (left) and at year 250 (right).

Chapter 12

Discussion

The point of this dissertation was to develop a new full-Stokes formulation that attempts to over come the problems of infinite viscosity introduced by Glens Law. These infinite viscosities occurred in ice sheets where the ice sheet experienced very little stresses or deformation. Essentially, this was where the ice sheet was moving as a solid chunk. The development of this formulation started by returning the full-Stokes system back to a first-order system by creating a new set of variables from the velocity gradient. This led to the velocity-gradient viscosity formulation. Another first-order system was generated by setting the deviatoric stress as a new set of variables. This new method involved absorbing the viscosity into the new variables thereby viscosity, μ, was removed from the system and replaced by the fluidity, ϕ. Thus the basic and augmented fluidity formulation were created. One benifit of this fluidity-based formulation was that viscosity could become as large as necessary. However, a downside was that this leads to $\phi \to 0$, which affects coercivity as discussed in Section 6.3.

Once these formulations were developed, they were used to solve a variety of test problems. The first test problem was a simple infinity long, rectangular glacier flowing down an infinity long hill. This test problem showed that both the viscosity and fluidity formulations exhibited optimal finite element convergence. However, the augmented fluidity formulation was more accurate. Moreover, the fluidity formulation involved linear systems that were much more amenable to solution by AMG. As seen in Figure 7.6, nested iteration allowed for most of the nonlinear iterations to be performed on the coarse grid. The overall computational cost of the algorithm using the augmented

fluidity formulation was significantly less than with the viscosity formulation. With the addition of the adaptive refinement via ACE, even better accuracy per computational cost was achieved.

The next step was to move on to a more complicated test problem. The ISMIP-HOM [39] contained a series of benchmarks that feature several experiments to test ice-sheet models and also supplied a database of solutions from other methods for comparison. The first experiment, benchmark B, involved another infinitely long glacier with a spatially varying basal topography. The interesting aspect of this test solution was that the fluidity tended towards zero at several point along the surface of the glacier. When compared with a formulation developed in [30], the fluidity formulation produced fluidity/viscosity that were significantly smaller/larger than the Galerkin Taylor-Hood method. One factor for why this happened had to do with the fact that the FOSLS formulation approximated the stresses, s_{11} and s_{12} in a discrete subspace of H^1. Whereas, the Taylor-Hood method had to take numerical derivatives of the velocities to produce these stresses, which resulted in additional errors.

It was shown that the fluidity based method achieved optimal finite element convergence when the curl equations are omitted, as in the basic fluidity system, or when scaled by ϕ. However, increasing the scaling on the curl equations by using a scaling of either $\psi^{-1/2}$ or $\phi^{-1/2}$ resulted in reduced finite element convergence but improved AMG performance. This trend continued on in benchmark D.

Benchmark D was another ISMIP experiment that was solved using both fluidity formulations. Benchmark D involves an glacier that had a basal sliding boundary condition. Basal sliding occurred when a water systems developed between a glacier or ice sheet and the bed. With large basal sliding, the velocity variation across the bed became more uniform, which resulted in very large viscosities. This type of a problem was the reason a fluidity-based formulation was developed. As expected, the solutions found using the augmented fluidity formulation better resolved the fluidity/viscosity than the Galerkin method as seen between Figure 9.3. Additionally, this test showed that, although augmenting the fluidity formulation with a curl-based equation yields better AMG performance, the basic fluidity formulation consistently had optimal finite-element convergence.

This resulted in the basic fluidity formulation being the method used for solving the remaining two test problems.

The next benchmark, E, used real glacier geometry from the Haut Glacier d'Arolla in the European Alps. There were two variations on this benchmark. Experiment 1 involved a pure no-slip, basal boundary condition and experiment 2 had a small slippery patch. The solutions to both experiments were accurately resolve using the basic fluidity formulation and once again, yielded smaller fluidities the viscosity-based Taylor-Hood method. Additionally, the fluidity formulation also recovered several fluidity peaks that were absent in the Taylor-Hood method. The boundary conditions in experiment 2 result in singularities, which was resolved using a threshold adaptive mesh refinement method. Using the FOSLS functional as an error estimator resulted in optimal finite element convergence.

The last test problem was a 2-D adaptation of benchmark F with nonlinear viscosity and a time dependent free surface. Keeping with the trend, the fluidity formulation produced smaller fluidities than a viscosity-based method. This is especially true when two fluidity peaks coalesced. The fluidity formulation also remained stable longer than the Taylor-Hood method when using the notoriously unstable forward Euler method.

The future of this research is to continue to show the efficacy of the fluidity formulations at dealing with infinite viscosities. One possible application of this formulation is a ice shelf or grounding-line determination problem. Ice shelfs have an interesting set of basal boundary conditions. Most times, the boundary conditions start with a frozen bed, $\underline{u} = 0$, transition to basal sliding, $\underline{n} \cdot \underline{\underline{\sigma}} = \beta^2 \underline{u}$, and end with a floating free surface, $\underline{n} \cdot \underline{\underline{\sigma}} = 0$. The grounding line is the transition point between the grounded section and the floating free surface. It is expect that the floating part of the ice shelf experiences mostly translational velocities, which means large viscosities. Combining that with the basal sliding section, and this problem is the perfect application of a fluidity-based formulation.

Another future avenue of research involves optimizing the solver. The intent of the augmented fluidity formulation was to make a system that is amenable to AMG. However, the reality is AMG

requires some sense of a curl-type equation. In the case of a fluidity formulation, this curl equation involve a factor of ϕ, which can go to zero hurting the coercivity. An $H(\mathrm{div})$–type system based on a full-stress formulation can be solve using AMS or ADS [26, 27]. This would avoid the difficulties with the curl equation.

Bibliography

[1] hypre: A library of high performance preconditioners. `http://www.llnl.gov/CASC/hypre/`.

[2] J. Adler, T. Manteuffel, S. McCormick, J. Nolting, J. Ruge, and L. Tang. Efficiency based adaptive local refinement for first-order system least-squares formulations. SIAM J. Sci. Comp., 33:1–24, 2011.

[3] J. H. Adler, T. A. Manteuffel, S. F. McCormick, and J. W. Ruge. First-order system least squares for incompressible resistive magnetohydrodynamics. SIAM J. Sci. Comput., 32(1):229–248, 2010.

[4] S. Agmon, A. Douglis, and L. Nirenberg. Estimates near the boundary for solutions of elliptic partial differential equations satisfying general boundary conditions ii. Comm. Pure Appl. Math., 17:35–92, 1964.

[5] J. M. Allen, C. Leibs, T. Manteuffel, and H. Rajaram. A fluidity-based first-order system least-squares method for ice sheets. SIAM Journal on Scientific Computing, 39(2):B352–B374, 2017.

[6] W. H. Armstrong, R. S. Anderson, J. M. Allen, and H. RAJARAM. Modeling the worldview-derived seasonal velocity evolution of kennicott glacier, alaska. Journal of Glaciology, 62(234):763–777, 2016.

[7] M. Berndt, T. A. Manteuffel, and S. F. McCormick. Local error estimates and adaptive refinement for first-order system least squares (FOSLS). Electronic Transactions on Numerical Analysis, 6:35–43, 1997.

[8] E. Berthier, H. Vadon, D. Baratoux, Y. Arnaud, C. Vincent, K.L. Feigl, F. Rmy, and B. Legrsy. Surface motion of mountain glaciers derived from satellite optical imagery. Remote Sensing of Environment, 95(1):14–28, 2005.

[9] P. Bochev and Gunzburger. Least Squares Finite Element Methods. Springer, 2009.

[10] S. C. Brenner and L. R. Scott. The Mathematical Theory of Finite Element Methods, volume 15. Springer New York, New York, NY, 2008.

[11] W. Briggs, V. Henson, and S. McCormick. A Multigrid Tutorial: Second Edition. Society for Industrial and Applied Mathematics, Philadelphia, PA, USA, 2000.

[12] Z. Cai, R. Lazarov, T. A. Manteuffel, and S. F. McCormick. First-order system least squares for second-order partial differential equations: Part I. SIAM Journal on Numerical Analysis, 31(6):1785–1799, 1994.

[13] Z. Cai, T. Manteuffel, and S. McCormick. First-order system least squares for second-order partial differential equations: Part II. SIAM Journal on Numerical Analysis, 34(2):425–454, 1997.

[14] Z. Cai, T. A. Manteuffel, and McCormick S. First-order system least squares for stokes equations with application to linear elasticity. SIAM J. Numer. Anal., 34:1727–1741, 1997.

[15] Q Chen, M Gunzburger, and M Perego. Well-posedness results for a nonlinear stokes problem arising in glaciology. SIAM Journal on Mathematical Analysis, 45(5):2710–2733, 2013.

[16] A. Codd, T. A. Manteuffel, and S. F. McCormick. Multilevel first-order system least squares for nonlinear partial differential equations, with application to elliptic grid generation. SIAM J. Numer. Anal., 41:2197–2209, 2003.

[17] A. L. Codd, T. A. Manteuffel, and S. F. McCormick. Multilevel first-order system least squares for nonlinear elliptic partial differential equations. SIAM Journal on Numerical Analysis, 41(6):2197–2209, 2004.

[18] A. L. Codd, T. A. Manteuffel, S. F. McCormick, and J. W. Ruge. Multilevel first-order system least squares for elliptic grid generation. SIAM J. Numer. Anal., 41(6):2210–2232, June 2003.

[19] H. De Sterck, T. Manteuffel, S. McCormick, J. Nolting, J. Ruge, and L. Tang. Efficiency-based h-and hp-refinement strategies for finite element methods. Numerical Linear Algebra with Applications, 15(2-3):89–114, 2008.

[20] H. Elman, D. Silvester, and A. Wathen. Finite Elements and Fast Iterative Solvers with Applications in Incompressible Fluid Dynamics. Oxford University Press, 2014.

[21] R. Greve. A continuum–mechanical formulation for shallow polythermal ice sheets. Philosophical Transactions of the Royal Society A, 355(1726):921–974, 1997.

[22] R Greve and H Blatter. Dynamics of Ice Sheets and Glaciers. Advances in Geophysical and Environmental Mechanics and Mathematics. Springer-Verlag, 2009.

[23] M. D. Gunzburger. Finite Element Methods for Viscous Incompressible Flows: A Guide to Theory, Practice, and Algorithms. Academic Press, Boston, Mass., 1989.

[24] J. J. Heys, E. Lee, T. A. Manteuffel, S. F. McCormick, and J. W. Ruge. Enhanced mass conservation in least-squares methods for navier-stokes equations. SIAM J. Sci. Comput., 31(3):2303–2321, 2009.

[25] J. J. Heys, T. A. Manteuffel, and S. F. McCormick. On mass-conserving least-squares methods. SIAM J. Sci. Comput., 28(5):1675–1693, 2006.

[26] R. Hiptmair and J. Xu. Nodal auxiliary space preconditioning in $H(\nabla\times)$ and $H(\nabla\cdot)$ spaces. SIAM Journal on Numerical Analysis, 45(6):2483–2509, 2007.

[27] T. V. Kolev and P. S. Vassilevski. Parallel auxiliary space AMG for $H(\nabla\times)$ problems. Journal of Computational Mathematics, 27(5):604–623, 2009.

[28] C. A. Leibs. First-Order Systems Least-Squares Finite Element Methods and Nested Iteration for Electromagnetic Two-Fluid Kinetic-Based Plasma Models. PhD thesis, 2014.

[29] W. Leng, L. Ju, M. Gunzburger, and S. Price. Manufactured solutions and the verification of three-dimensional stokes ice-sheet models. The Cryosphere, (1):19–29, 2013.

[30] W. Leng, L. Ju, M. Gunzburger, S. Price, and T. Ringler. A parallel high-order accurate finite element nonlinear stokes ice sheet model and benchmark experiments. Journal of Geophysical Research: Earth Surface, 117(F1), 2012.

[31] A Logg, K.-A. Mardal, and G. N. et al. Wells. Automated Solution of Differential Equations by the Finite Element Method. Springer, 2012.

[32] T. A. Manteuffel and K. Ressel. A least-squares finite element solution of the neutron transport equation in diffusive regimes. SIAM J. Numer. Anal., 85:806–835, 1998.

[33] S. McCormick. Multilevel first-order system least squares (FOSLS) for helmholtz equations. Procs. Conf. Maxwell Equations, page 1993, 1994.

[34] Steffen Münzenmaier. First-order system least squares for generalized-newtonian coupled stokes-darcy flow. Numerical Methods for Partial Differential Equations, pages 1150–1173, 2014.

[35] J. Nolting. Efficiency-based Local Adaptive Refinement for FOSLS Finite Elements. PhD thesis, University of Colorado at Boulder, 2008.

[36] J. F. Nye. The flow of a glacier in a channel of rectangular, elliptic or parabolic cross-section. Journal of Glaciology, 5(41):661–690, 1965.

[37] R. K. Pachauri and A. Reisinger, editors. Climate Change 2007: Synthesis Report. IPCC, Geneva, Switzerland, 2007.

[38] F. Pattyn. A new three-dimensional higher-order thermomechanical ice sheet model: Basic sensitivity, ice stream development, and ice flow across subglacial lakes. Journal of Geophysical Research: Solid Earth, 108(B8), 2003.

[39] F. Pattyn, L. Perichon, A. Aschwanden, B. Breuer, B. de Smedt, O. Gagliardini, G. H. Gudmundsson, R. Hindmarsh, A. Hubbard, and J. V. Johnson. Benchmark experiments for higher-order and full stokes ice sheet models (ISMIP-HOM). The Cryosphere Discussions, (1):111–151, 2008.

[40] M Perego, M Gunzburger, and J Burkardt. Parallel finite-element implementation for higher-order ice-sheet models. Journal of Glaciology, 58(207):76, 2012.

[41] E. Rignot and P. Kanagaratnam. Changes in the velocity structure of the Greenland ice sheet. Science, 311(5763):986–990, 2006.

[42] H. Seddik, R. Greve, T. Zwinger, F. Gillet-Chaulet, and O. Gagliardini. Simulations of the Greenland ice sheet 100 years into the future with the full stokes model Elmer/Ice. Journal of Glaciology, 58(209):427–440, 2012.

[43] S. Solomon, D. Qin, M. Manning, Z. Chen, M. Marquis, K.B. Averyt, M. Tignor, and H.L. Miller, editors. Contribution of Working Group I to the Fourth Assessment Report of the Intergovernmental Panel on Climate Change. Cambridge University Press, Cambridge, United Kingdom and New York, NY, USA, 2007.

[44] V. K. Tzanio and S. V. Panayot. Parallel auxiliary space AMG solver for $H(\nabla\cdot)$ problems. SIAM Journal on Scientific Computing, 34(6):A3079–A3098, 2012.

[45] M. van den Broeke, J. Bamber, J. Ettema, E. Rignot, E. Schrama, W. J. van de Berg, E. van Meijgaard, I. Velicogna, and B. Wouters. Partitioning recent Greenland mass loss. Science, 326(5955):984–986, 2009.

[46] C. Westphal. First-Order System Least Squares (FOSLS) for Geometrically Nonlinear Elasticity in Nonsmooth Domains. PhD thesis, University of Colorado at Boulder, 2004.

[47] H. Zhang, L. Ju, M. Gunzburger, T. Ringler, and S. Price. Coupled models and parallel simulations for three dimensional full-stokes ice sheet modeling. Numer. Math. Theory Methods Appl., 4:359–381, 2011.